# Chapter 5

## *Control of YBCO-TFA Growth Parameters*

Chemical solution growth of epitaxial thin films has arisen as a new and very exciting opportunity for the development of advanced functional ceramic materials[5.1]. The preparation of superconducting CC, where a biaxial texture of the superconducting oxide needs to be reached on metallic substrates, can strongly benefit from this new methodology. This growth process appears to be very promising in view of the preparation of low cost conductors. Nowadays, one of the cheapest techniques to growth YBCO is the TFA-MOD process. Recently, various groups in the world have investigated this promising TFA-MOD to prepare high-$J_c$ YBCO films[1.26, 1.28, 1.30, 4.12, 4.17, 5.2]. It is, however, a complex issue to reach full control of all the microstructural factors which may influence the superconducting properties of these conductors. It appears to be very appealing to first investigate the influence of the processing parameters on the growth mechanisms and the microstructural development in single crystalline substrates. A detailed understanding of the microstructure and the ability to control the microstructure are key issues for successful device application. This challenge has been taken for the superconductivity group at ICMAB in the scope of the European project called *SOLSULET*.

We have showed in section 4.2.2, that in order to achieve high quality YBCO TFA films during the pyrolysis process the film homogeneity must be preserved; otherwise the final superconducting performances are degraded. Now in this chapter, we will focus on the relevance of the control of YBCO TFA growth parameters on the final microstructure and superconducting properties. The growth parameters studied are: reaction time, growth temperature, water vapour pressure and gas flow rate. Finally, due to the intrinsic nature of the sol-gel compounds, non-optimized growth conditions may

lead to very porous YBCO TFA-MOD films, hence we have investigated the influence of porosity on the superconducting properties of YBCO TFA-MOD films and its possible reduction by applying a sintering process.

## 5.1. Reaction Time for $BaF_2$ Decomposition

After optimization of the solution deposition and pyrolysis parameters (chapter 4), we have concentrated on the study of the control of the reaction time in order to optimize the growth process of YBCO TFA-MOD films. One of the key issues of TFA-MOD process is the $BaF_2$ decomposition at the growth step. At present there exist different opinions about the reaction of $BaF_2$ decomposition. Two proposed mechanisms have been reported: The first one, it is claimed by Smith *et al*[1.28], they propose that a mixture of nanocrystalline precursors exists, such as $BaF_2$, CuO and $Y_2Cu_2O_5$, as a result of the pyrolysis process. These nanocrystalline precursors react with the water vapour of the wet atmosphere to give $YBa_2Cu_3O_{6.5}$ tetragonal phase and generate HF gas as subproduct following the reaction:

| | |
|---|---|
| $2\,BaF_2 + 2\,CuO + 0.5\,Y_2Cu_2O_5 + 2H_2O \xrightarrow{O_2} YBa_2Cu_3O_{6.5} + 4HF\uparrow$ | (5.1) |

The advancement of this reaction is mainly controlled by temperature and water pressure, $P(H_2O)$, while oxygen pressure, $PO_2$, shifts the stability limits of the YBCO phase and hence also influences the reaction kinetics [1.28, 5.3, 5.4].

The second mechanism claimed by Araki *et al*[5.3] proposes that the reaction between nanocrystalline precursor and water vapour consists of two steps:

| | |
|---|---|
| $2BaF_2 + 2H_2O \rightarrow 2BaO + 4HF\uparrow$ | (5.2) |
| $2BaO + 2CuO + 0.5Y_2Cu_2O_5 + xO_2 \rightarrow YBa_2Cu_3O_{6.5}$ | (5.3) |

Later, Araki *et al* [1.26] proposed a light variation of this mechanism. Specifically, they found that after the pyrolysis process the precursor film consists of nanocrystalline CuO

surrounded by an amorphous matrix of the oxyfluorur Y-Ba-O-F, then CuO reacts very slowly with the amorphous matrix and $H_2O$ to give $YBa_2Cu_3O_{6.5}$ and HF.

| | |
|---|---|
| $CuO + Y - Ba - O - F + H_2O \xrightarrow{O_2} YBa_2Cu_3O_{6.5} + HF \uparrow$ | (5.4) |

In any of the models, the participation of water vapour is very important in the $BaF_2$ decomposition to obtain $YBa_2Cu_3O_{6.5}$, but it is necessary to know how much time we need to apply the wet atmosphere in order to obtain a completely reacted film and avoid that $H_2O$ attacks the $YBa_2Cu_3O_{6.5}$ tetragonal phase.

As we saw in chapter 4, micro-Raman spectroscopy is a versatile, sensitive and non destructive technique to detect impurities and secondary phases on YBCO TFA-MOD films. From equations (5.1) to (5.3), a completed reacted film is obtained when $BaF_2$ traces disappear. Moreover, the $BaF_2$ phase has a strong Raman efficiency and thus it is easier to detect by micro-Raman spectroscopy than by XRD. This fact, allowed us to monitor the extinction of the $BaF_2$ Raman signal in the Raman spectra, and thus determine the necessary reaction time of a precursor film in the growth process at T~790 $^oC$ and obtain a completely reacted sample.

To quantify the presence of $BaF_2$ phase on incompletely reacted YBCO TFA-MOD films, we need to find the Raman scattering efficiency ratio between these two phases. We prepared powder pellets of 1 gram containing $BaF_2$ and YBCO phases at different concentrations (from 10%wt to 50%wt $BaF_2$). The grain size of these two phases was ensured <1μm by a ball milling process. No changes in the powder structure or oxygen content were observed as it was determined by micro-Raman spectroscopy technique. The Raman spectras of mixed powder pellets are shown in figure 5.1a, they were collected in backscattering configuration by using a microscope objective of x10 magnification (laser spot ~ 10μm).

Then, we determined the Raman scattering efficiency ratio between the integrated intensity of the $BaF_2$ phonon mode at 241 $cm^{-1}$ and the integrated intensity of the YBCO phonon modes at 340 and 500 $cm^{-1}$ for the six powder pellets, *i.e.*:

$$\frac{I_{BaF_2}}{I_{YBCO}} = \frac{I_{241}^{BaF_2}}{I_{340}^{O(2,3)} + I_{500}^{O(4)}} \quad (5.5)$$

Figure 5.1b shows the experimental values of the integrated intensity ratio as a function of $BaF_2$ % nominal content in weight, a linear behaviour has been found with a slope of 0.2.

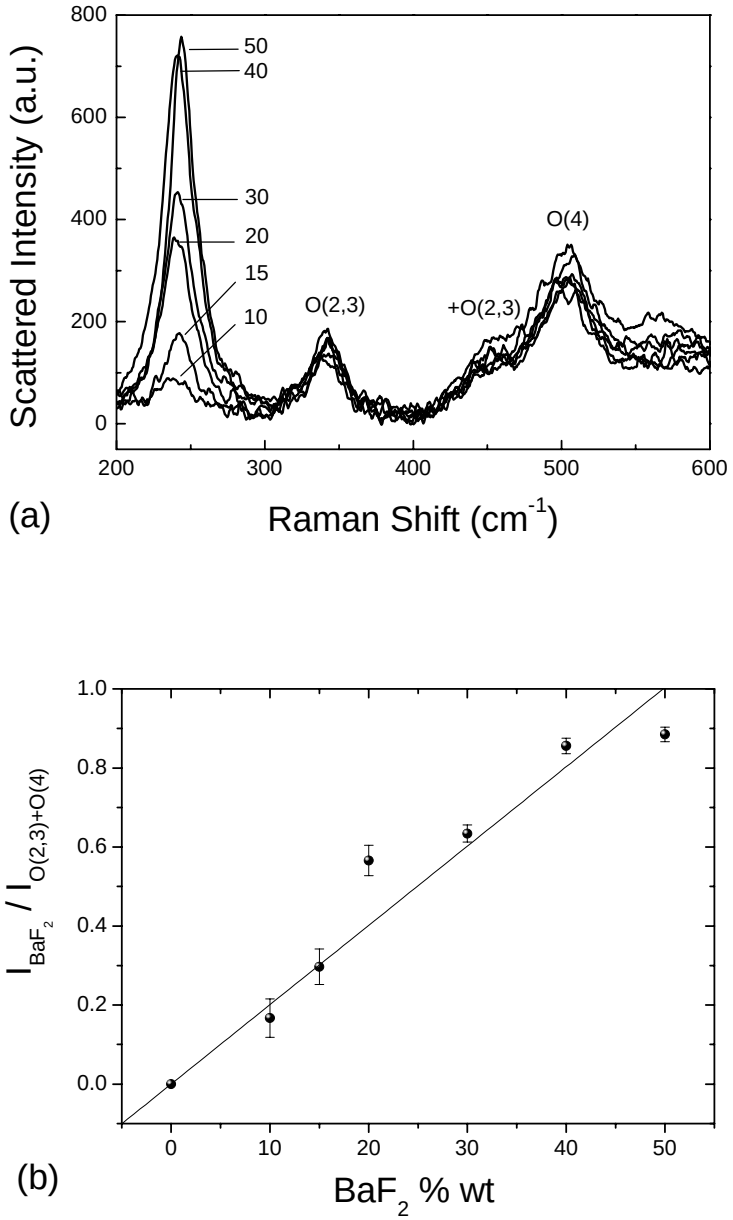


Figure 5.1. (a) Raman spectra of powder pellets of $BaF_2$ + YBCO between 10% wt of $BaF_2$ and 50% wt, notice the increase of the signal at 241 $cm^{-1}$ as the nominal content of $BaF_2$ increases. (b) Linear relationship between the integrated intensity ratio and $BaF_2$ % wt nominal content. The fit of the experimental values has a slope value ~ 0.2.

Therefore, we have been able to obtain a linear relationship between the ratio of the integrated intensities of $BaF_2$ and YBCO phonon modes and $BaF_2$ % wt nominal content in the powder pellets. Then, with this information we are able to quantify the $BaF_2$ phase present on the YBCO TFA-MOD samples and determine the proper reaction time required to complete the reaction. In this sense, we made four samples with optimized pyrolysis process and different reaction times. Characteristics of these samples are shown in tables 5.1 and 5.2, and micro-Raman analysis was performed to each sample.

**Table 5.1**

Conditions for YBCO films to study the reaction kinetics

| |
|---|
| Precursor solution prepared from Y, Ba and Cu acetates |
| Concentration = 1.5 M |
| LAO Substrate |
| Optimized pyrolysis process |
| $T_{growth}$ = 790 $^{o}$C |
| $P(H_2O)$ = 24 mbar |
| $P(O_2)$ = 0.2 mbar |
| Reaction time = variable + 30 min dry |
| Standard oxygenation |

**Table 5.2**

$BaF_2$ % content in weight in YBCO films at different reaction times

| **Sample** | **Time (min)** | $\mathbf{I}_{BaF_2} / \mathbf{I}_{O(2,3)+O(4)}$ | **$BaF_2$ % wt** |
|---|---|---|---|
| T10 | 10 | 0.16 | 8.15 |
| T30 | 30 | 0.11 | 5.6 |
| T90 | 90 | 0.09 | 4.25 |
| T150 | 150 | 0 | 0 |

Figure 5.2a shows the values of $BaF_2$ % wt for the four reaction times studied. Micro-Raman was able to detect small amounts of $BaF_2$ on YBCO films up to 4 % respect to the YBCO phase. In figure 5.2b we observe that at 30 minutes the $BaF_2$ phonon peak is clearly visible corresponding to an incompletely reacted TFA-MOD film, while at 150 minutes a fully reacted sample is obtained where only the YBCO phonon modes are observed. Additionally, we also note that our completely reacted film samples did not display additional bands (around 580 $cm^{-1}$) in the Raman spectra which have been associated to cation disorder in the YBCO structure[5.4,5.5], thus indicating that high quality films have been obtained. In particular this sample at 150 minutes corresponds to a biaxially textured and high-$J_c$ film, $\Delta\phi \sim 1^o$ with $J_c$(77K) ~3 MA/$cm^2$, respectively. Therefore, the micro-Raman analysis allowed us to restrict the reaction time (150 minutes in wet atmosphere) and thus, optimize the preparation process of YBCO TFA-MOD films for the growth rate imposed by the growth parameters of table 5.1. At present, members of the superconductivity group are working on increasing the growth rate focused on process industrialization, and in that case reaction times should also be further reduced.

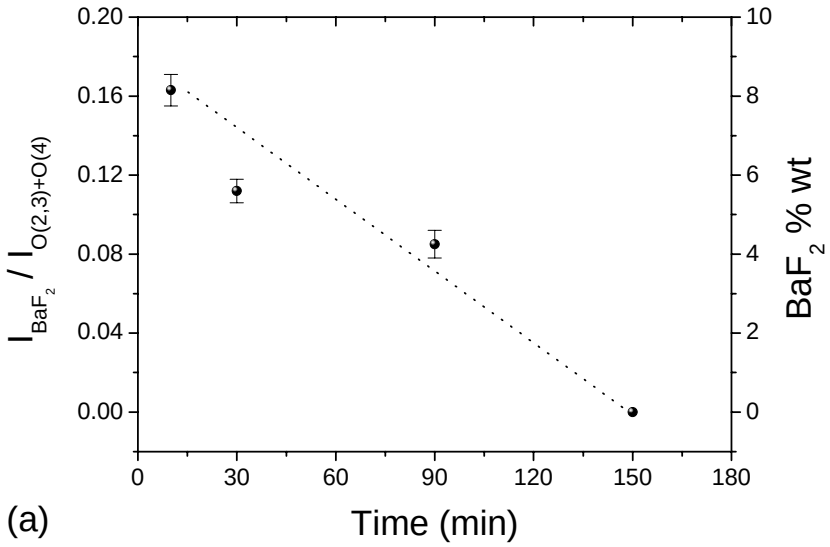


Figure 5.2 (a)

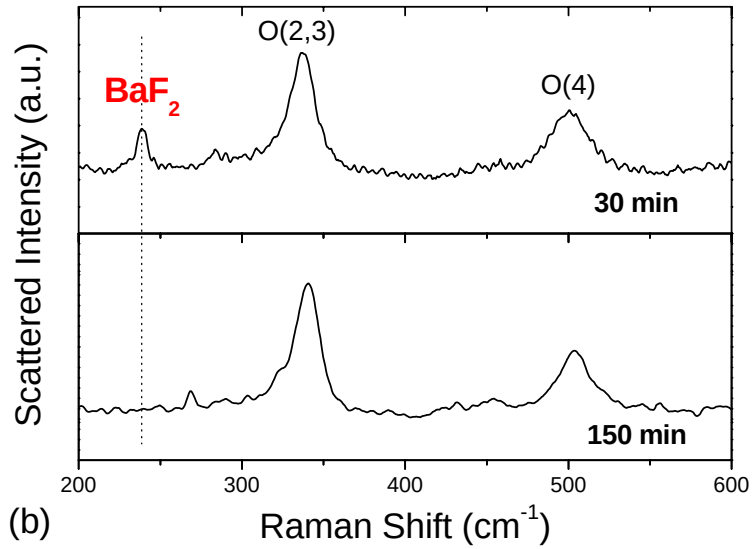


Figure 5.2. (a) $BaF_2$ % in weight values and integrated intensity ratio at different reaction times (b) an incompletely reacted film at 30 min where the $BaF_2$ phonon peak is clearly seen, while 150 min correspond to a fully reacted sample where only the YBCO phonons modes are observed.

## 5.2. Growth Temperature

After optimization of the reaction time, we have concentrated on the study of the influence of the growth temperature on the final microstructure and superconducting properties. The influence of growth temperature in the preparation of TFA films becomes apparent due to the strong temperature dependence of the reaction kinetics. A detailed understanding of the microstructure and the ability to control the microstructure are key issues for high-$J_c$ growth of TFA films.

We began a systematic study of the influence of the growth temperature on the final properties to optimize this experimental parameter. In order to be able to isolate the influence of this parameter we kept all the other processing parameters constant. Two experimental batches were grown where only the temperature variation of the growth annealing process was changed. These two batches have different preparation method of precursor solution, as we saw in section 4.1, *i.e.* from Y, Ba and Cu acetates and commercial YBCO powder, they also have different water pressures, 24 mbar and 7

mbar, respectively. These precursor solutions were deposited on LAO single crystal by spin coating technique and thicknesses in the range 250 to 400 nm were obtained depending on the solution precursor viscosity (250 nm for acetates and 400 nm for oxide powder). Tables 5.3 and 5.4 show the experimental parameters used to growth these films.

**Table 5.3**

Conditions for YBCO films prepared from acetates

| |
|---|
| Precursor solution prepared from Y, Ba and Cu acetates |
| Concentration = 1.5M |
| Optimized pyrolysis process |
| $T_{growth}$ = variable |
| Thickness = 0.25 μm |
| $P(H_2O)$ = 24 mbar |
| $P(O_2)$ = 0.2 mbar |
| Reaction time = 150 min wet + 30 min dry |
| Total gas flow rate= 0.024 m/s |
| Standard oxygenation |

**Table 5.4**

Conditions for YBCO films prepared from commercial powder

| |
|---|
| Precursor solution prepared from YBCO commercial powder |
| Concentration = 1.5M |
| Optimized pyrolysis process |
| $T_{growth}$ = variable |
| Thickness = 0.40 μm |
| $P(H_2O)$ = 7 mbar |
| $P(O_2)$ = 0.2 mbar |
| Reaction time = 150 min wet + 30 min dry |
| Total gas flow rate= 0.024 m/s |
| Standard oxygenation |

### 5.2.1. Study of Growth Temperature on samples prepares from Y, Ba and Cu acetates

We prepared five samples following the experimental parameters of table 5.3. The studied growth temperatures were 700°, 725°, 750°, 790° and 830 °C. XRD was used as a routine technique to characterize the crystalline structure and epitaxy of the YBCO films. Figure 5.3 shows the θ-2θ XRD patterns obtained for this batch.

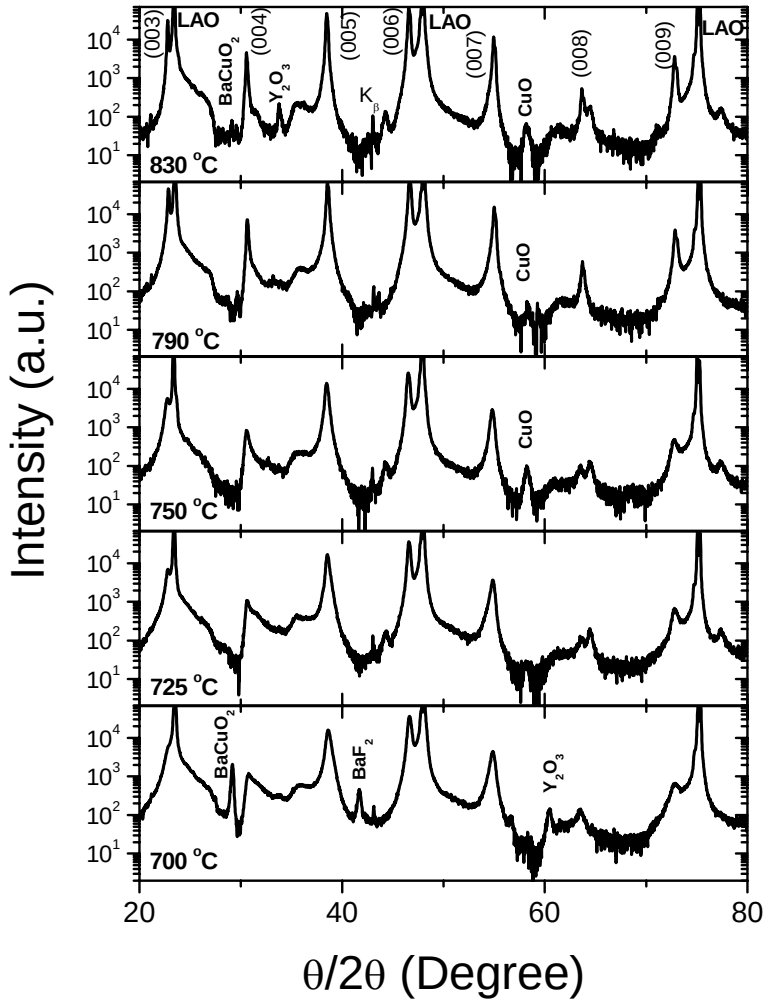


Figure 5.3. XRD patterns in logarithmic scale of YBCO samples prepared from acetates at different temperatures. At high temperature a better crystalline structure is observed.

In figure 5.3 we can observe clearly the (*00l*) YBCO profiles increasing on intensity as the growth temperature is increased. Strong (*00l*) peaks of YBCO indicate that the TFA

films have a large fraction of *c*-oriented grains with regard to the LAO substrate. We can also observe the (*h00*) reflections coming from LAO single crystal and associated reflections due to Cu $K_\alpha$ radiation. We have observed that the intensity values of (005) YBCO profiles was increasing; denoting enhancement of crystalline structure, as shown in figure 5.4. At 700 $^oC$ we have obtained YBCO epitaxial but some secondary phase and impurity amounts of $Y_2O_3$, $BaF_2$ and $BaCuO_2$ phases were present in the film. The peak intensity of the phases $Y_2O_3$ , $BaF_2$ and $BaCuO_2$ was less than ~1%, ~3 % and ~13 %, respectively, in comparison with the intensity of (*005*) YBCO profile. Clearly, the appearance of the $BaF_2$ and $BaCuO_2$ phases is related to low processing temperature. On the contrary, $Y_2O_3$, CuO and $BaCuO_2$ phases appearing at high temperature were less than 1% in comparison with the intensity of (*005*) YBCO profile.

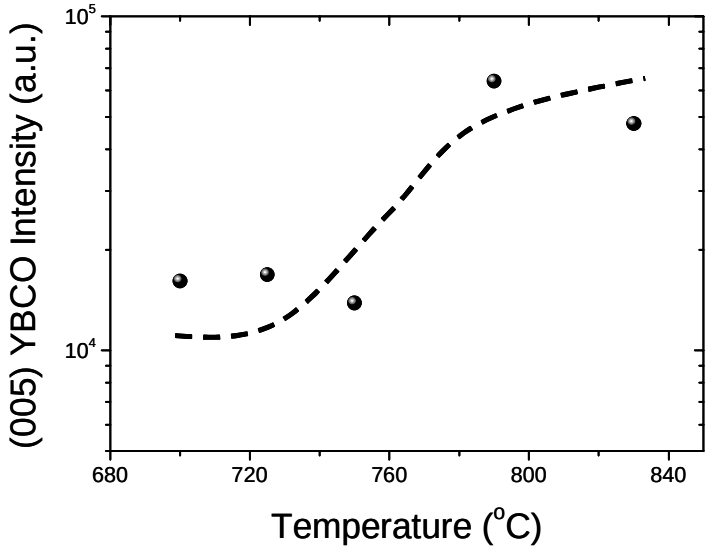


Figure 5.4. XRD intensity of (*005*) YBCO profile as a function of growth temperature.

The YBCO ceramic oxide is an anisotropic compound, thus it is very important to obtain *c*-axis oriented grains perpendicular to the substrate surface, because a misorientation produces a detrimental of superconducting performances. We also performed XRD ω-scans measurements. In figure 5.5 we show the Δω values of (*005*) YBCO profile as a function of growth temperature, no systematic dependence with the temperature can be appreciated in the FWHM values ($0.50 \leq \Delta\omega \leq 0.72$).

The presence of the $BaCuO_2$ phase found by XRD is correlated with micro-Raman measurements at the same temperature (700 $^oC$). In figure 5.6a the Raman spectra of this batch are shown. We observed only YBCO phonons in films grown at high temperatures.

Additionally, the evaluation of *c*-axis oriented grains, δ, was performed by micro-Raman spectroscopy using equation 3.8c, by averaging five different 10 μm laser spots, as we did in chapter 3 to obtain the uniaxial texture. The uniaxial texture values of these samples are shown in figure 5.6b, observing a maximum value ~ 0.92. The uniaxial texture depends on the processing temperature. Our results are comparable with the ones obtained by Iguchi *et al*[5.6] for a processing temperature of 800 $^oC$, δ ~ 0.90. The high uniaxial texture values obtained on YBCO TFA-MOD films, confirms that it is possible to grow highly *c*-axis oriented YBCO films by TFA-MOD process and thus the industrialization of the process to produce long length YBCO CC is viable.

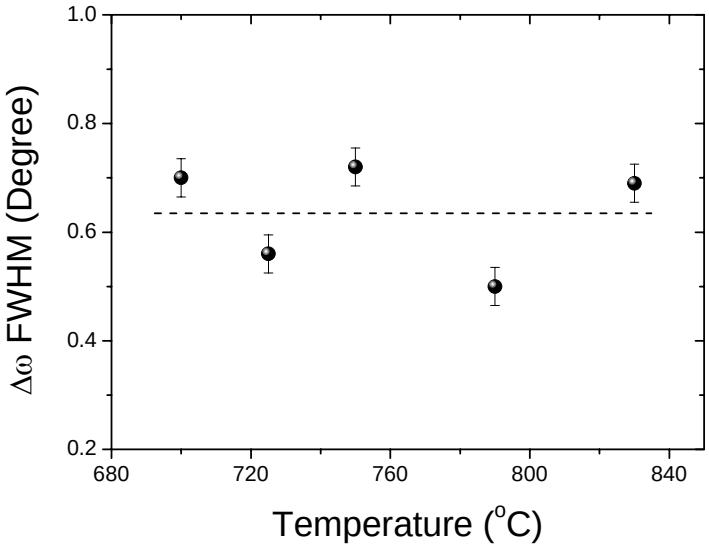


Figure 5.5. FWHM values of the XRD ω-scans measurements of the (*005*) YBCO profile as a function of the growth temperature.

On the other hand, surface microstructure of this batch was obtained by SEM micrographs, as illustrated in figure 5.7. The differences in residual porosity of these samples are easily seen. The growth temperature influenced the morphology of the samples. While the sample prepared at 700 $^oC$ is extremely porous, a progressive

decrease in pore size and concentration is evident when the temperature is increased, and at 790 $^{o}$C and 830 $^{o}$C the pores have nearly vanished. The presence of some *a*-axis oriented grains is denoted by needle-shape grains with typical size ~ 1 μm.

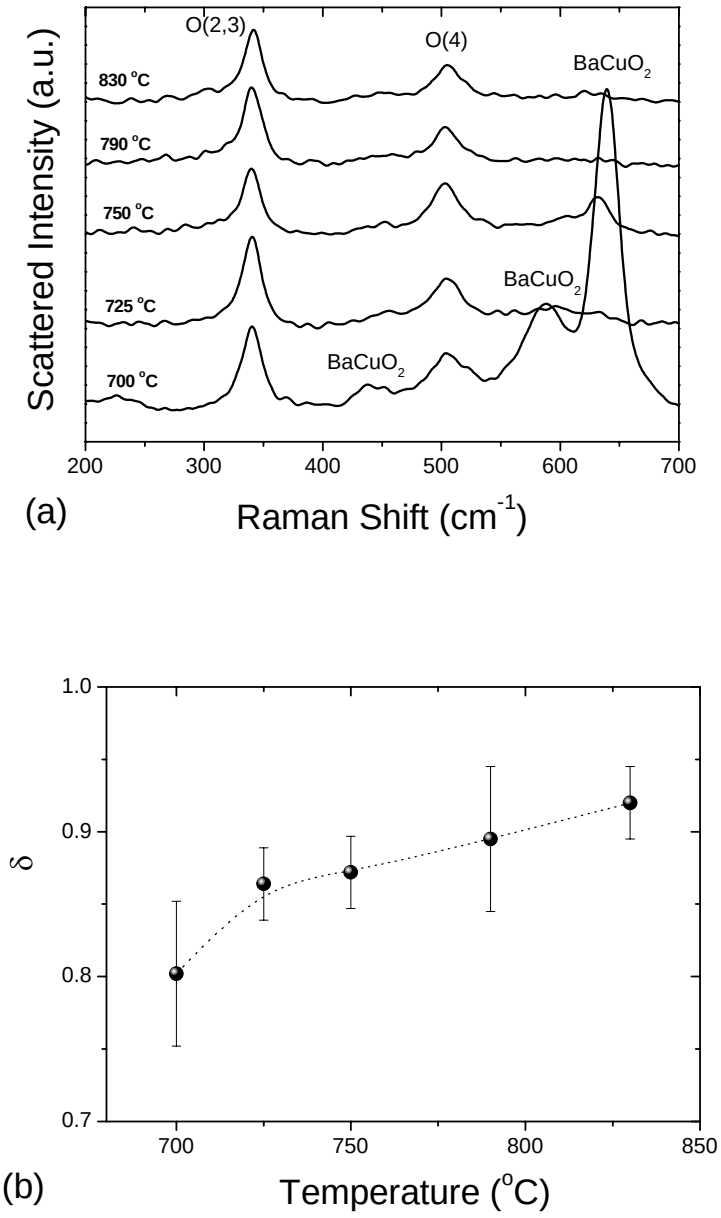


Figure 5.6. (a) Polarized micro-Raman spectra of YBCO samples prepared from acetates at different growth temperatures. (b) Uniaxial texture evolution with growth temperature.

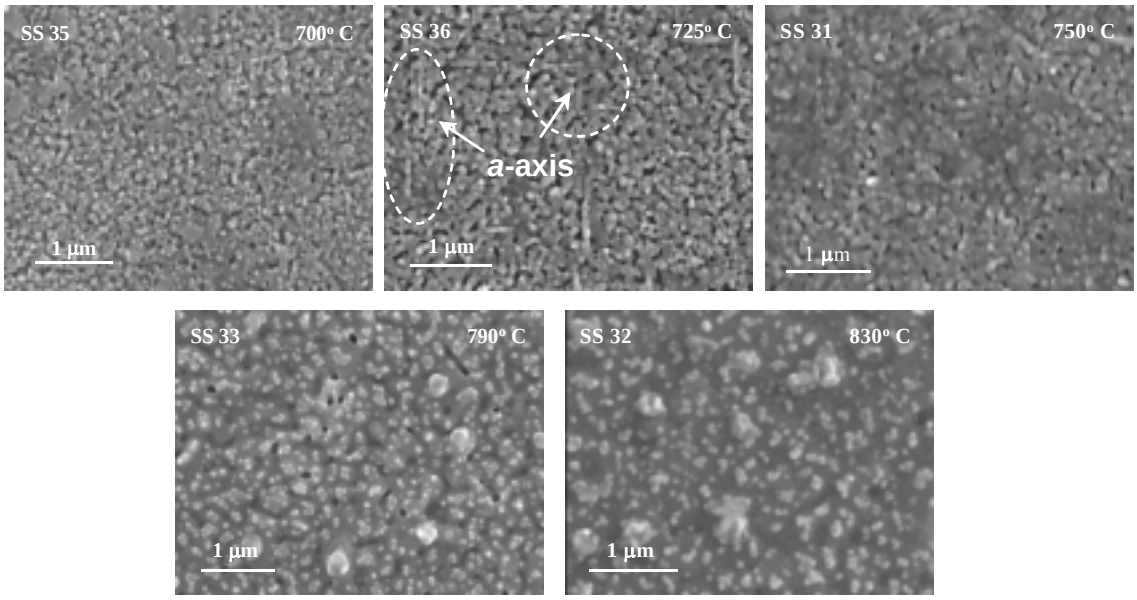


Figure 5.7. SEM micrographs of YBCO samples grown via acetates at different firing temperatures. Qualitative information about final porosity is seen. At low temperatures porous films with presence of *a*/*b*-oriented grains are obtained, in contrast at 830 $^{o}$C a dense film is grown.

We have found particularly that the porosity of the samples is strongly dependent on the growth temperature. Texture analysis performed by micro-Raman spectroscopy has evidenced an existing relationship between *a*-axis oriented grains, porosity and superconducting properties[5.7], as we will show more in detail later in section 5.5. Moreover, the influence of the growth temperature and the associated porosity modification can be clearly detected and quantified through measurements of the temperature dependence of the electrical resistivity in the normal state, because a pore is an *obstacle* for current transport. Thus, porosity affects seriously the high current-carrying capability of the TFA films, as it is confirmed below by resistivity measurements at 300K and $J_c$ transport measurements.

As shown in figures 5.8 and 5.9, $\rho_{300K}$ approaches to the YBCO single crystal value, 200 μΩ-cm [5.8], and $J_c$ value increases up to ~ 2.5 MA/cm$^2$ for samples grown at 790 $^{o}$C. These optimum values correlate with micro-Raman results on the uniaxial texture δ ~ 0.92, *in-plane* texture $\Delta\phi \sim 1.1^{o}$ degree, dense samples in SEM micrographs and high crystalline structure in XRD patterns, denoting high performing YBCO TFA-MOD film. On the contrary the presence of porosity, secondary phases or impurities results in poor

connectivity of YBCO grains[1.29,5.7] giving raise to high normal state resistivity and low $J_c$ values. This fact could also be related with the low $J_c$ value observed at 700 $^oC$.

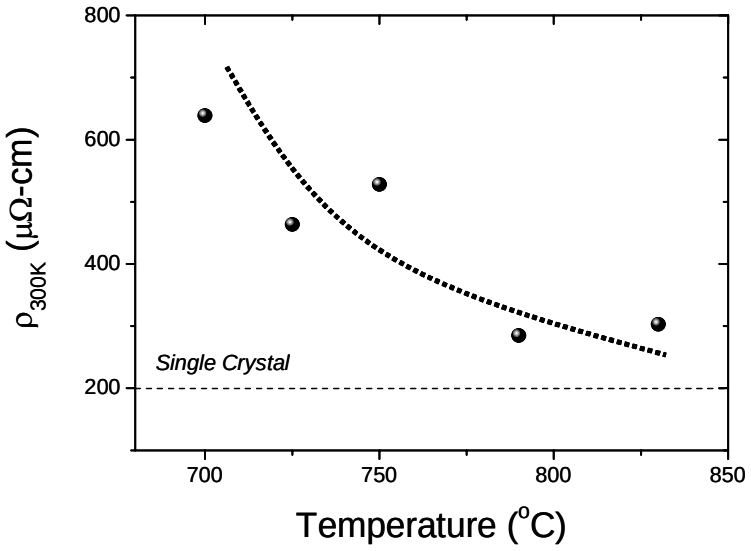


Figure 5.8. Resistivity values at 300K of YBCO samples grown via acetates at different firing temperatures.

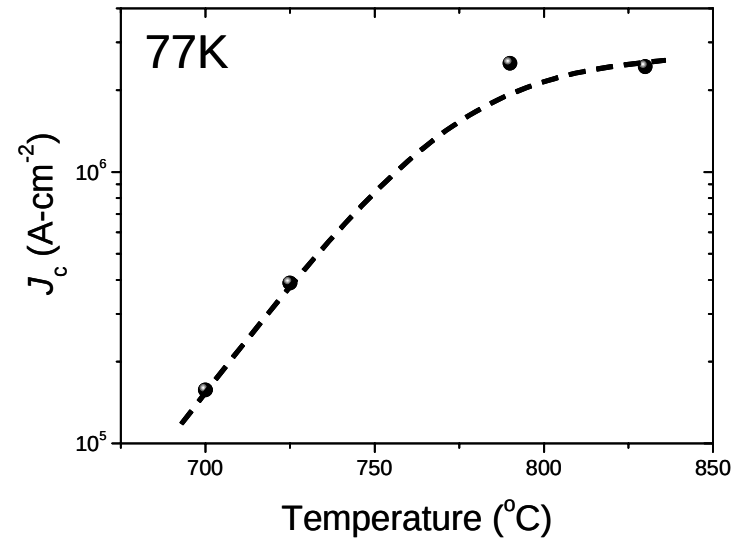


Figure 5.9. Critical current density at 77K of YBCO samples grown via acetates at different firing temperatures. Notice that the $J_c$ value at 790 $^oC$ and 830 $^oC$ is higher than ~2.5 MA/cm$^2$.

Moreover, the misfit between YBCO and LAO due to different cell parameters and thermal dilatation coefficients, makes possible that they expand in different ways at a given growth temperature, therefore it will be more favourable a particular orientation

(*h00*) or (*00l*) of the YBCO grains according to the growth temperature. Mukaida *et al*[5.9] studied the lowest temperature for *c*-axis preferred oriented thin film growth at different substrate materials by PLD, as show in figure 5.10.

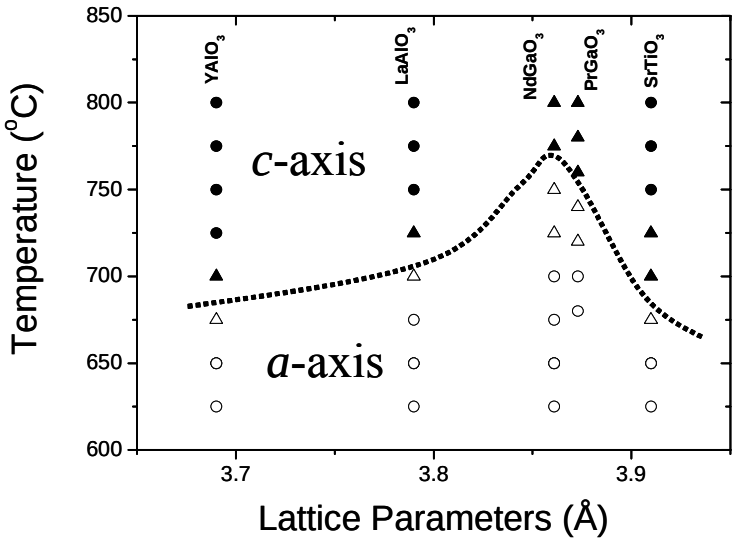


Figure 5.10. Substrate temperature dependencies of the main orientation axis of $YBa_2Cu_3O_7$, thin films grown on different substrate materials such as: (*001*) Nd:$YAlO_3$ (*a* = 3.69 Å), (*001*) $LaAlO_3$ (*a* = 3.79 Å), (*110*) $NdGaO_3$ (*a* = 3.86 Å), (*100*) $NdPrO_3$ (*a* = 3.87 Å) and (*100*) $SrTiO_3$ (*a* = 3.91 Å). Solid circles (●), solid triangles (▲), open triangles (△), and open circles (○) represent grown thin films that were fully c-, almost c-, almost a-, and fully a-axis preferred orientation, respectively.[adapted from reference 5.9].

Therefore, at the light of these results, the increase of the growth temperature during the annealing process has proved to have a tremendous influence on the final microstructure and superconducting properties of the samples. High temperature treatments evidence an improving of *c*-axis oriented grains on the YBCO films and superconducting performances.

### 5.2.2. Study of Growth Temperature on samples prepared from commercial YBCO powder

We prepared nine samples following the experimental conditions of table 5.4. The precursor films were converted at different growth temperatures 650°, 700°, 745°, 775°, 790°, 795°, 800°, 810° and 820 °C. Figure 5.11 shows the XRD patterns of this second

batch. We can clearly observe the (*00l*) YBCO peaks increasing in intensity as the growth temperature increases. Strong peaks of YBCO (*00l*) indicate that we have a large fraction of *c*-axis oriented with regard to the LAO surface at high temperatures. We also observe the (*h00*) LAO profiles and associated reflections due to Cu $K_\alpha$ radiation. At 650 $^oC$ we have obtained YBCO phase with no traces of secondary phases or impurities. But at 820 $^oC$ some secondary phases such as $Y_2O_3$ and CuO were present in the film. The peak intensity of the phases $Y_2O_3$ and CuO was less than ~1%, in comparison with the intensity of (*005*) YBCO profile. The appearance of these impurity phases will be discussed later in chapter 6. As in the case of the acetate films, the intensity of (*005*) YBCO intensity was increasing with increasing the growth temperature denoting an improvement of crystalline structure, as clearly shown in figure 5.12.

We also performed routinely XRD ω-scan measurements of YBCO (*005*) profile, the FWHM values are in the range of $0.64^o \leq \Delta\omega \leq 0.78^o$ (figure 5.13). As it was obtained in YBCO films grown from acetates there is not a clear dependence of Δω values with temperature though an increase of intensity of the XRD profiles is observed. Better crystalline structure films are obtained between 745 $^oC$ and 795 $^oC$, this fact reveals that there exists a range of annealing temperatures to grow TFA films with acceptable crystalline structure to obtain *c*-axis grains perpendicular to substrate surface. SEM micrographs of surface microstructure shown in figure 5.14, show the same trend as the batch prepared from acetates namely, the porosity decreases with the increasing of annealing temperature. Notice that at close to the highest temperatures used 810, 820 $^oC$ (for commercial powder) or 830 $^oC$ (for acetates) we are rather closed to the decomposition limit at $P(O_2)$ = 0.2 mbar (see figure 5.15) and therefore, slight modification of the temperature tendency could be expected, namely figure 5.17, 5.18 and 5.19. Later, in section 5.5 we will show the relationship among resistivity, uniaxial texture and critical currents.

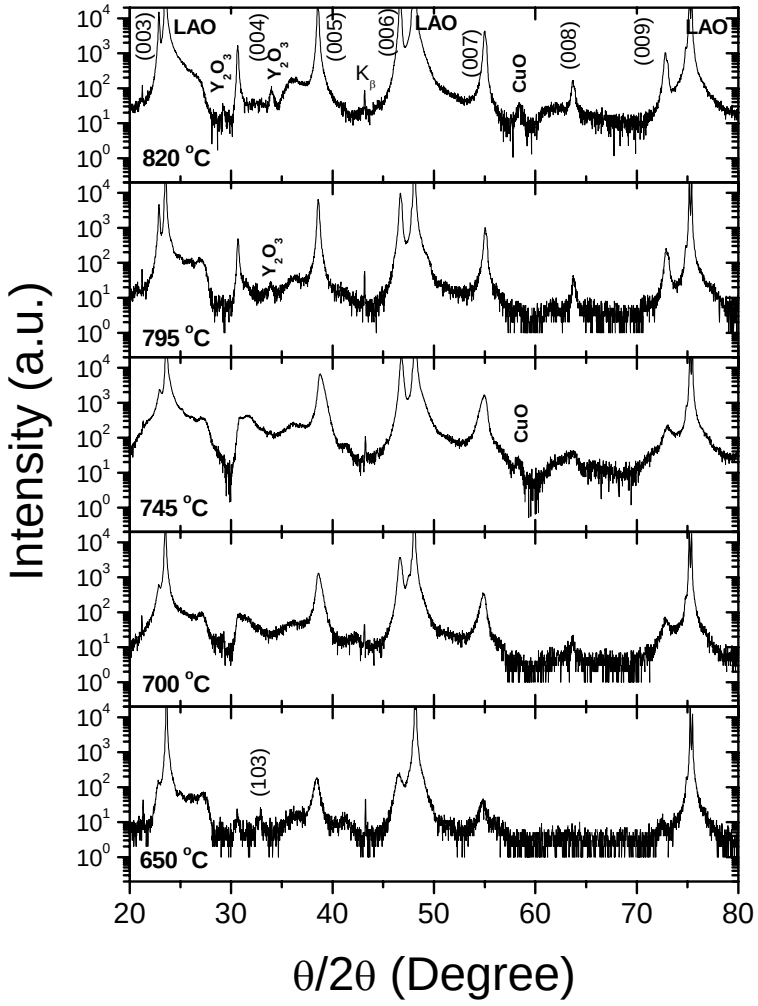


Figure 5.11. XRD patterns in logarithmic scale of films prepared via commercial YBCO powder. Notice the high crystalline structure of samples grown at high temperatures, the absence of $BaCuO_2$ traces and signals of CuO and $Y_2O_3$.

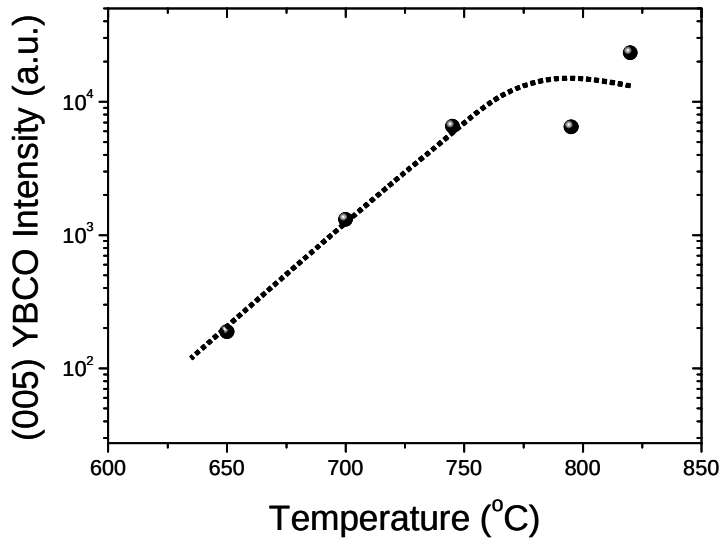


Figure 5.12. XRD intensity of (*005*) YBCO profile as a function of growth temperature. Notice the enhancement of crystalline structure at high temperatures.

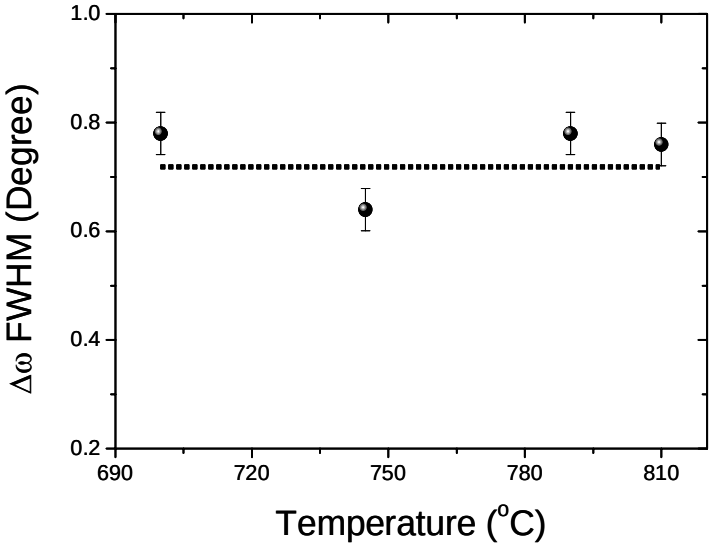


Figure 5.13. FWHM values of the XRD ω–scan measurements of the (*005*) YBCO profile as a function of the grow temperature, for samples prepared form commercial YBCO powder.

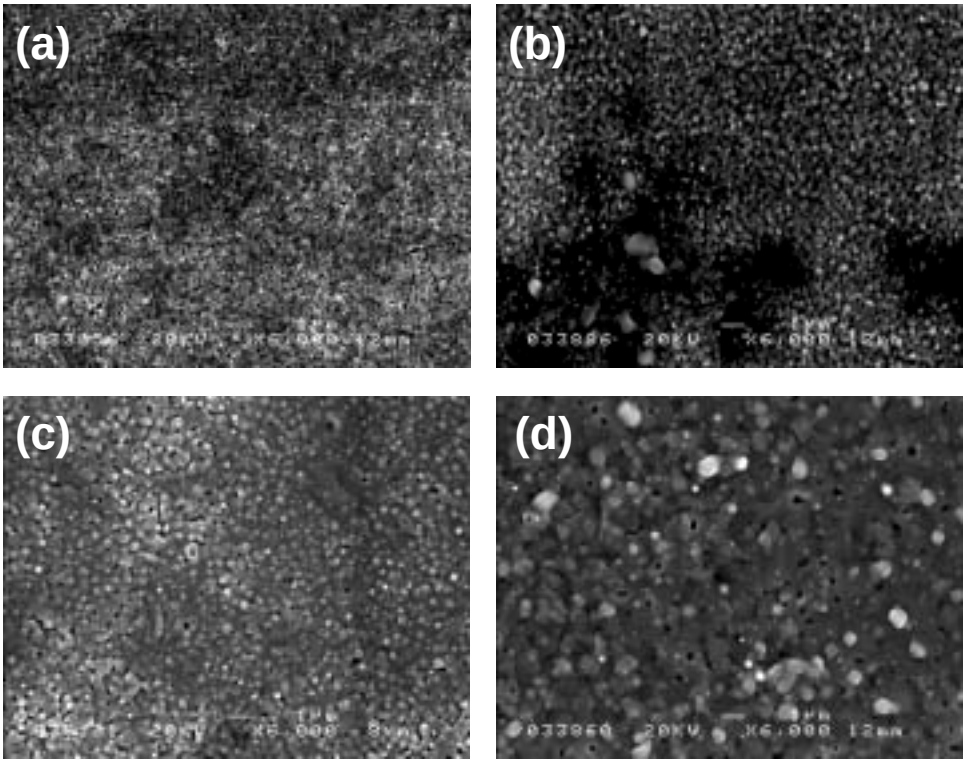


Figure 5.14. SEM micrographs of YBCO samples prepared via commercial powder at different firing temperature (a) 700, (b) 745, (c) 795 and (d) 810 $^{o}$C.

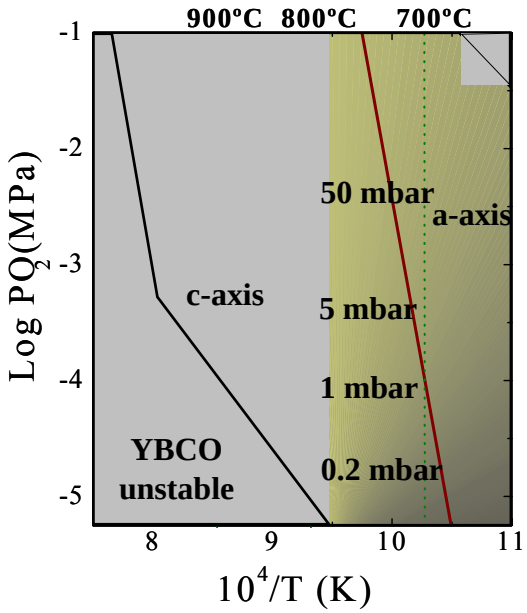


Figure 5.15. P($O_2$)-temperature phase diagram of YBCO adapted from reference [5.10]. Notice we are in the working zone of $PO_2$ ~ 0.2 mbar.

Micro-Raman measurements are shown in figure 5.16. They correlate the XRD results since we clearly observe YBCO Raman signal for all the growth temperature range studied. We have observed favourable *a*-axis orientation at growth temperatures below 700 $^{o}$C, as it is clearly observed in figure 5.16 by the higher intensity of the O(4) phonon mode with regard to the O(2,3) phonon mode. On the other hand, for temperatures above 700 $^{o}$C, the relative intensity of the O(4) phonon mode decreases with regard to the O(2,3) phonon intensity, denoting an increase of *c*-axis oriented grains concentration on the film.

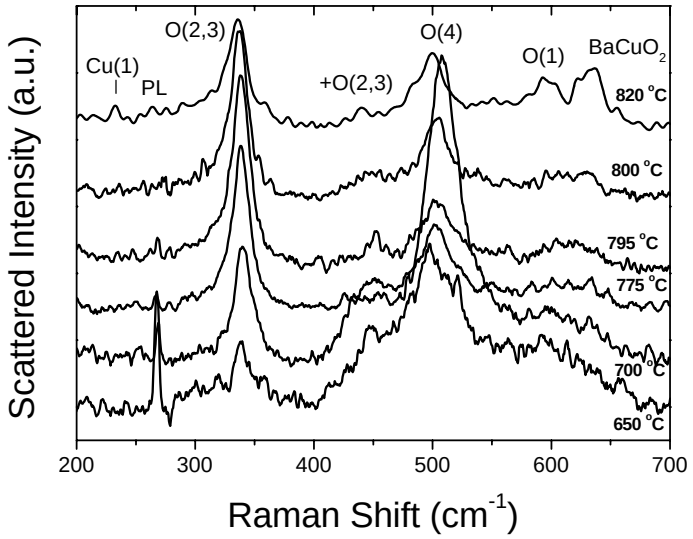


Figure 5.16. Polarized micro-Raman spectra of YBCO samples prepared from commercial YBCO powder.

The evaluation of uniaxial texture, δ, was performed by averaging five measurements performed at five different points on the samples using the ~10 μm laser spot. We noticed that a strong dependence of uniaxial texture with annealing temperature exists as clearly observed in figure 5.17. This trend is in agreement with the previously observed behaviour on samples grown from acetates (figure 5.6b). The evolution of uniaxial texture reveals that there is a range of annealing temperatures between 745 $^{o}$C ≤ $T_{growth}$ ≤ 800 $^{o}$C to growth *c*-axis oriented films. We have also observed that the uniaxial texture for the annealing temperature range between 745 $^{o}$C and 800 $^{o}$C has nearly the same value δ ~ 0.90. Below 745 $^{o}$C, strong *a*-axis growth with small δ values is attained. For annealing temperatures over 800 $^{o}$C Raman signals from CuO chain site disorder

and $BaCuO_2$ impurities appear, as is seen in figure 5.16. Also a decrease of the uniaxial texture value was observed, as displayed in figure 5.17.

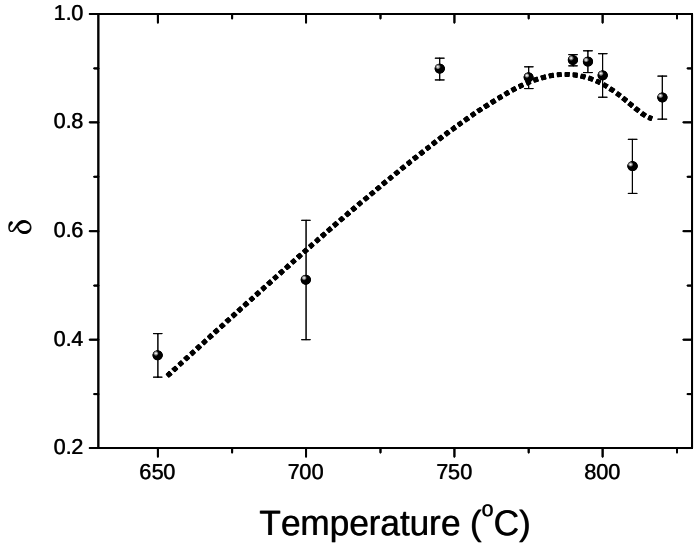


Figure 5.17. Uniaxial texture values determined from micro-Raman as a function of grow temperature for the YBCO samples prepared via commercial YBCO powder.

Transport measurements, $\rho_{300K}$ and $J_c$, are shown in figures 5.18 and 5.19 respectively. The $J_c$ values, at 77K, increase until ~ 2.35 MA/cm$^2$ correlated with $\rho_{300K}$ ~ 300 μΩ-cm values approaching to the YBCO single crystal value (200 μΩ-cm)[5.8]. These values obtained are correlated with XRD, micro-Raman and SEM results. As in the case of acetate based films, high crystalline structure, dense matrix and high uniaxial texture denote a biaxial textured and high $J_c$ superconducting films.

At the light of the results, the annealing temperature has the following influence on the YBCO TFA growth: nucleation of *a*-axis grains is favourable at low annealing temperature as shown in the diagram of figure 5.15; instead, high annealing temperatures promote *c*-axis oriented grains perpendicular to substrate surface. All these facts are in agreement with Mukaida *et al*[5.9] and Iguchi *et al*[5.6]. We conclude that, the optimized growth temperature is 795 °C - 800 °C. This working range is below the oxidation limit of metal tapes, therefore at the ICMAB group this YBCO TFA-MOD processing treatment has been transmitted to metallic substrates for future CC production.

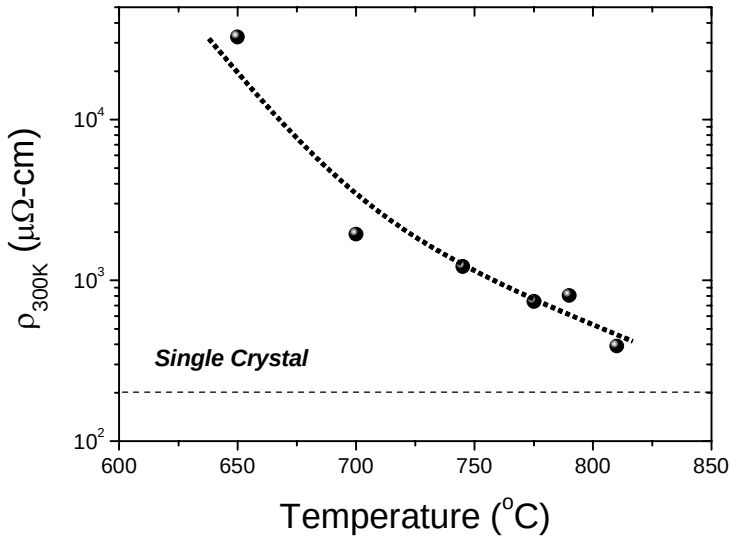


Figure 5.18. Resistivity values at 300K as a function of growth temperature of samples prepared from commercial YBCO powder.

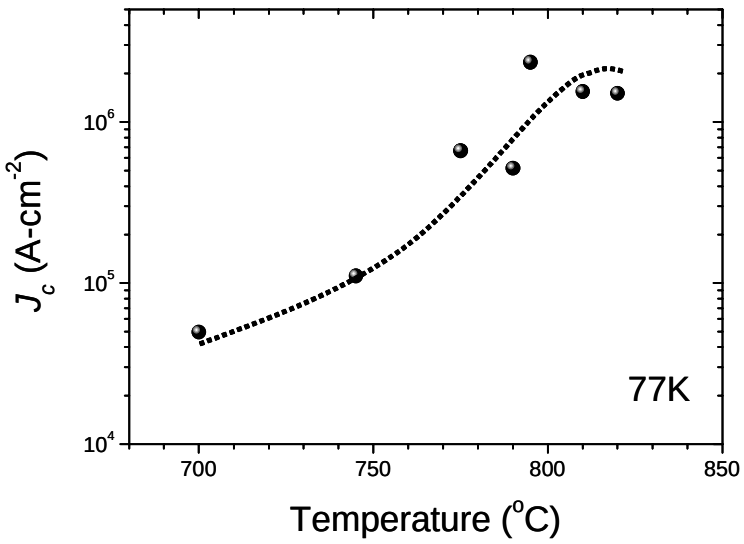


Figure 5.19. Critical current density at 77K of YBCO samples prepared form commercial powder. Notice a maximum $J_c \sim 2.35$ MA/cm$^2$ at 795 $^o$C.

From the two sets of experiments on acetates- and oxides-based, we have observed that for high growth temperature we have obtained $\delta$, $J_c$ and $\rho$ values very similar, but for low growth temperature the actual values of these parameters were very different. This fact may be due to the difference in the water vapour pressure, 24 mbar for acetates and 7 mbar for oxides (see tables 5.3 and 5.4), though also a difference in the thickness

between the two sets of samples (0.25 and 0.40 μm, respectively) existed. The $P(H_2O)$ growth parameter is certainly an important parameter to take into account because the $P(H_2O)$ is directly related to the local rate of conversion from $H_2O$ to HF as we saw in chapter 4 (equation 4.8). Therefore, in the following section we have performed a deep study of this growth parameter.

## 5.3. Water Vapour Pressure.

We studied the variation of the final microstructure and the superconducting properties with another principal parameter in the growth of YBCO TFA-MOD films, the water vapour pressure. The chemical reaction for YBCO phase formation requires water vapour at certain pressure in order to decompose the $BaF_2$ intermediate phase (see equation 5.1 or 5.2). There exists a direct dependence of the local rate of conversion from $H_2O$ to HF, *i.e.*, $R \propto \sqrt{P(H_2O)}$ (equation 4.8). We will expect that high pressure values produce distorted growth of the film and need to find an optimum work pressure range. Seven samples were prepared in the water vapour pressure values: 1.5, 6, 7, 11.5, 23, 24 and 26 mbar. In order to be able to isolate the influence of this parameter we kept all the other processing parameters constant considering the optimized growth temperature at 795 $^{o}$C. Experimental conditions of these samples are shown in table 5.5.

**Table 5.5**

Growth conditions of YBCO films with variable water pressure

| |
|---|
| Precursor solution prepared from YBCO commercial powder |
| Concentration = 1.5 M |
| Optimized pyrolysis process |
| $T_{growth}$ = 795 $^{o}$C |
| Thickness = 0.4 μm |
| $P(H_2O)$ = variable |
| $P(O_2)$ = 0.2 mbar |
| Reaction time = 150 min wet + 30 min dry |
| Standard oxygenation |

The XRD patterns of samples grown at different water vapour pressures are shown in figure 5.20. We obtained YBCO XRD signals for all range of water pressure studied. In particular, we have observed strong intensity of the YBCO profiles in the sample grown at 23 mbar. This is an indication of higher crystalline structure and high *c*-axis grains concentration of the TFA film. We also observed the (*h00*) reflections coming from LAO substrate and associated reflections due to Cu $K_\alpha$ radiation. The peak intensities of secondary phases, such as $Y_2Cu_2O_5$ (Y225) and CuO, were compared with its respective (*005*) YBCO intensity, thus they were minor than 1% to be present on the TFA films. However, it is important to note that the precursor phase $Y_2Cu_2O_5$ appears for low water pressures, *i.e.*, low growth rate.

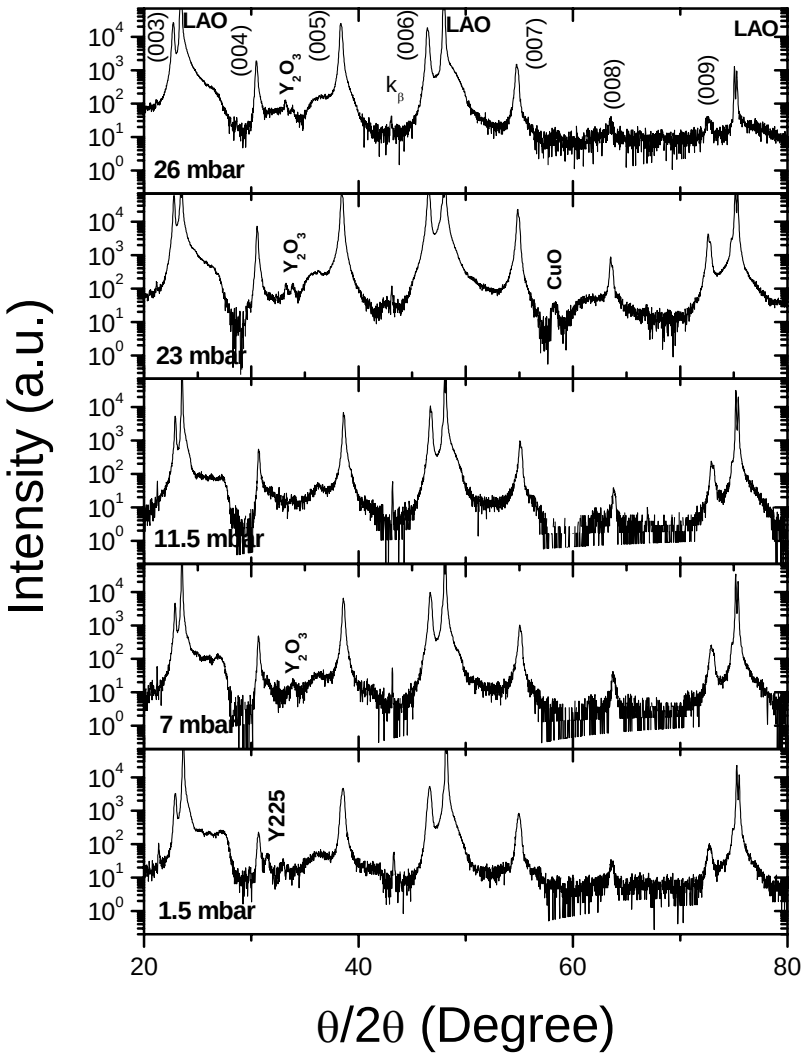


Figure 5.20. XRD patterns in logarithmic scale of films produced via commercial YBCO powder at different water vapour pressures.

XRD ω-scan measurements indicate FWHM values between $0.42^{o} \leq \Delta\omega \leq .\ 0.90^{o}$, as shown in figure 5.21. To determine the uniaxial texture, we also performed micro-Raman measurements which are shown in figure 5.22. The evaluation of uniaxial texture, δ, was also performed by averaging five different 10 μm laser spot. We have observed that at water pressures in the range of 5 to 15 mbar the uniaxial texture is constant $\delta \sim 0.9$, but at water pressure below 5 mbar or above 23 mbar there is a slight decrease of uniaxial texture $\delta \sim 0.8$. Additionally, we observed below 5 mbar and above 23 mbar appearance of defects in the Raman spectra (figure 5.23) such as Cu(1) and O(1) prohibited Raman phonons at 230 $cm^{-1}$ and 595 $cm^{-1}$ respectively, is observed as a result of the presence of broken Cu-O chains in the YBCO structure[5.11]. This kind of disorder is due to fragments of CuO chains, *i.e.* if an atom is located at the inversion center of the CuO metallic chain and is displaced along the chain direction, the change of the electric susceptibility of all bonds to one side is exactly compensated by the bonds of the opposite side. When a chain is infinitely long, this cancellation occurs for all atoms. However, for finite fragment, the displacement due to even modes involving atoms at the extremes of the chain is not compensated leading to a Raman signal.

In the SEM micrographs of the surface morphology shown in figure 5.24, we do not appreciate changes in surface microstructure with regard to different water vapour pressure. These surface microstructures with different water vapour pressures are in agreement with the studies on YBCO films grown by the $BaF_2$ process between $P(H_2O)$, total pressure and temperature carried out by Yoo *et al*[5.12].

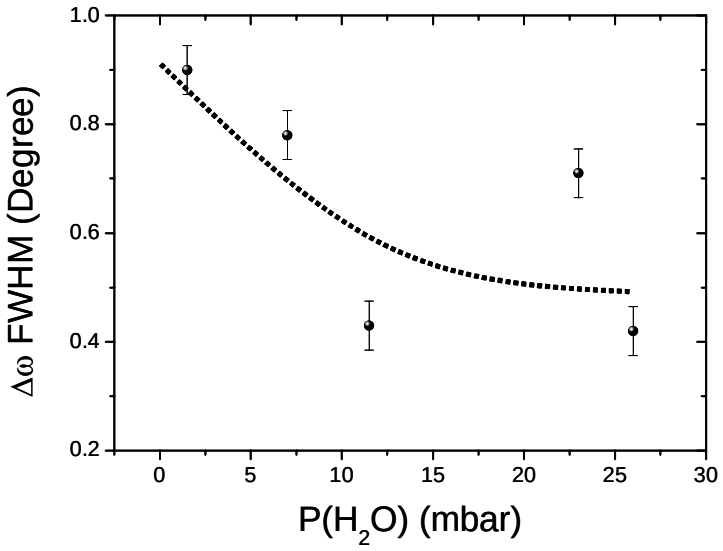


Figure 5.21. FWHM values of the XRD ω-scan measurements of (*005*) YBCO profile as a function of the water pressure.

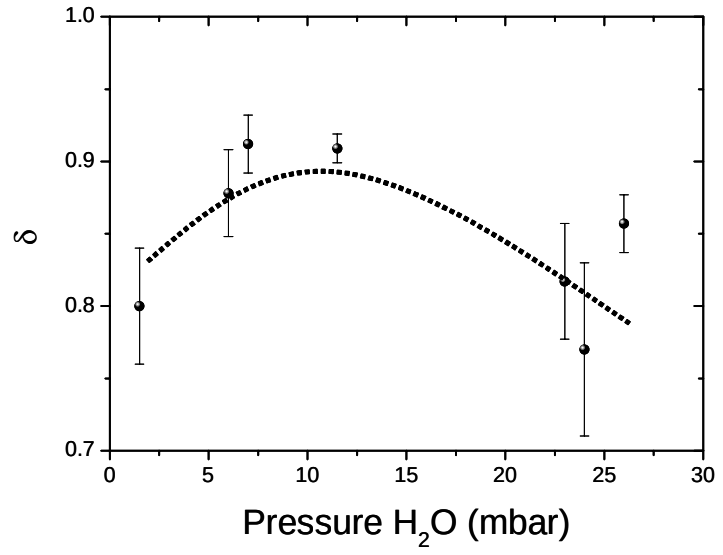


Figure 5.22. Uniaxial texture of YBCO samples grown at different water pressures.

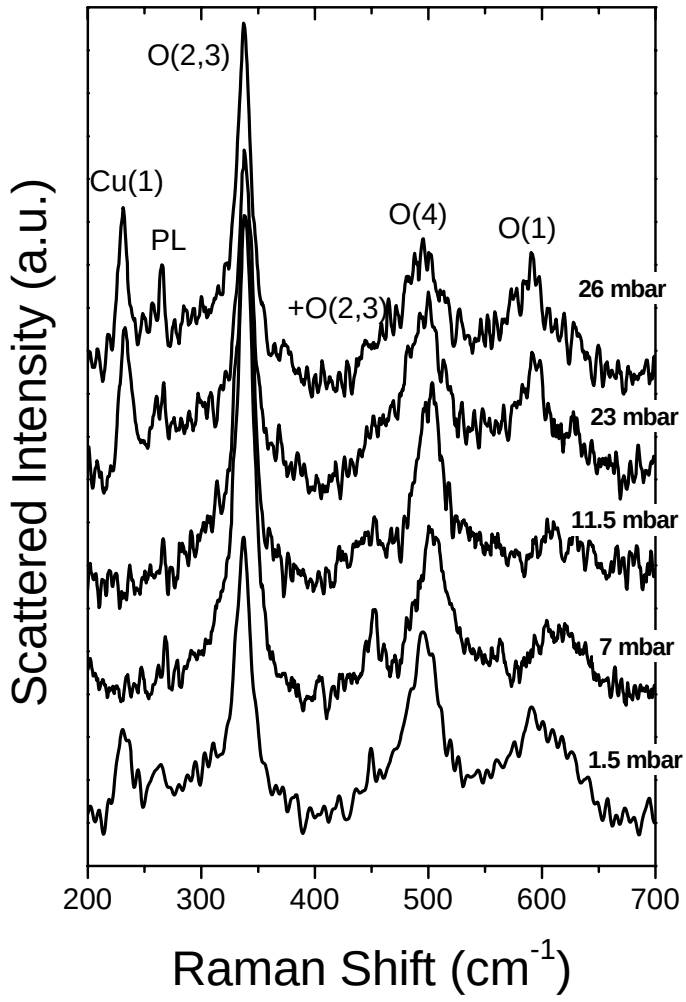


Figure 5.23. Micro-Raman spectra of YBCO samples grown at different water pressures. Notice the appearance of defects such as Cu(1) and O(1) at 230 $cm^{-1}$ and 595 $cm^{-1}$ respectively, denoting broken CuO chains.

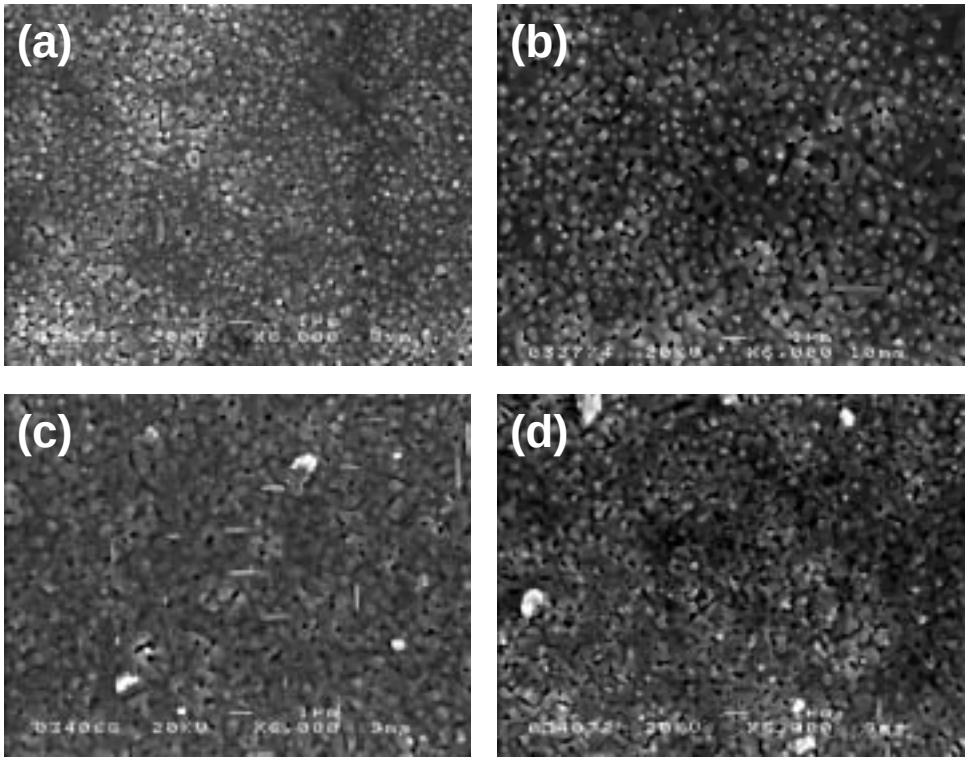


Figure 5.24. SEM micrographs of YBCO samples produced via commercial YBCO powder at different water vapour pressures (a) 7, (b) 11.5, (c) 23 and (d) 26 mbar. Notice that we can not observe important changes in porosity and surface morphology.

Then, we performed transport measurements of these films. Figures 5.25 and 5.26 show the resistivity, $\rho_{300K}$ and $J_c$ as a function of water vapour pressure. As we see, the $\rho_{300K}$ values approach to YBCO single crystal value (200 μΩ-cm) in the range of 5 – 12 mbar of water vapour pressures, micro-Raman measurements show that samples grown at that water vapour pressure are free from defects, as illustrated in figure 5.23, meanwhile at water vapour pressures above 23 mbar and below 5 mbar we observed an increase of the $\rho_{300K}$ values, confirming a more distorted growth. In addition, at water pressures below 5 mbar the $\rho_{300K}$ values were very high with respect to pressures above 23 mbar. Moreover, from critical current density measurements at 77K, $J_c$ is constant for water pressures between 5 -12 mbar but undergoes a drastic drop of three orders of magnitude for water pressure values higher than 23 mbar and one order of magnitude for values lower than 2.5 mbar. Yoo *et al*[5.12] and Iguchi *et al*[5.6], also observed a strong decrease on $J_c$ values at higher water pressures. As stated earlier in the Raman measurements, samples grown at higher and lower water pressure values show the appearances of Cu(1) and O(1) Raman modes related to structural defects in YBCO.

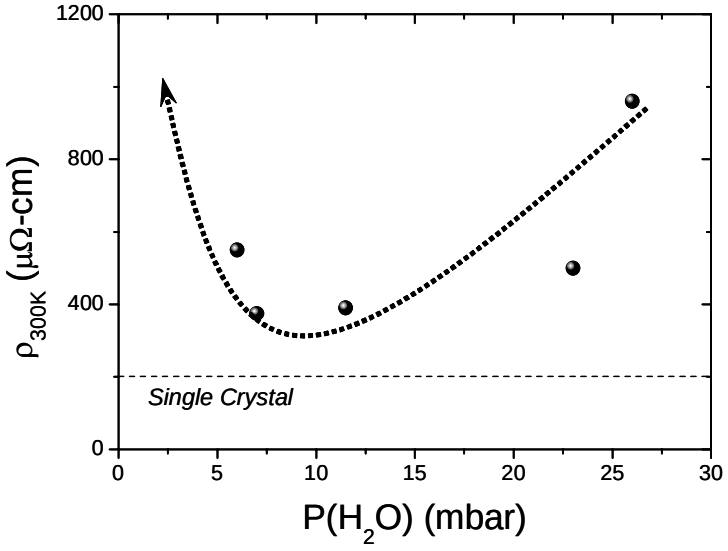


Figure 5.25. Resistivity measurements at 300K of YBCO samples prepared by commercial powder at different water pressure values.

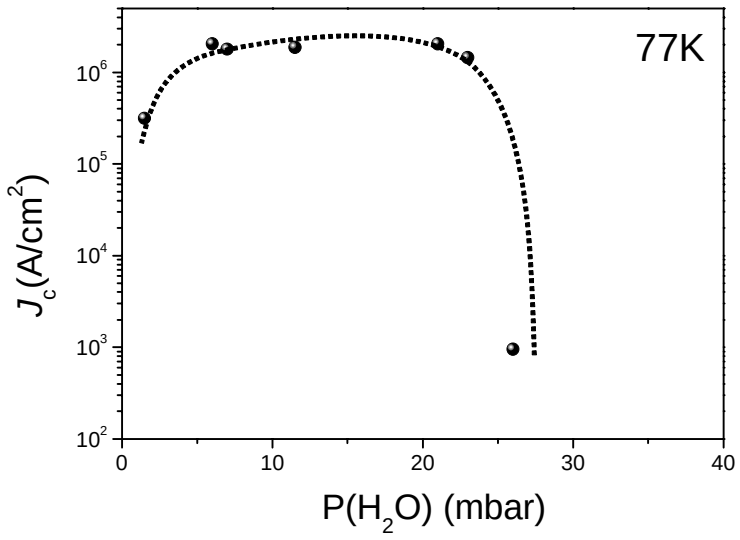


Figure 5.26. Critical current density of YBCO samples grown at different water pressures.

As we presented in chapter 4, low water vapour pressures involve low conversion rates (equation 4.8) and not enough HF release; this might not complete the reaction, or even entrap HF, precipitate of the precursor phases or generate disorder. On the contrary, for high water vapour pressure we have high conversion rates and thus, may obtain a distorted growth front producing a disordered growth. At the light of these results, we may conclude that the water vapour pressure values optimum for the preparation of highly *c*-axis oriented and high-$J_c$ YBCO films are in the range of 6 mbar ≤ $P(H_2O)$ ≤ 11 mbar.

Another parameter to take into account is the gas flow rate in the reaction zone, because it is related to the diffusion boundary layer (figure 4.6). Thus, the HF swept out from the reaction zone may be strongly related to the gas flow rate. In the next section we focus on the study of this growth parameter.

## 5.4. Gas Flow Rate

Another parameter studied in the preparation of YBCO TFA-MOD films was the gas flow rate in the furnace. As we saw in section 4.1, the relation between the gas flow vector of water pressure and the HF gas is very important, because with the increase or decrease in the gas flow rate, more or less moisture ($H_2O$) is carried into the reaction zone and the HF of the reaction is swept out of the reaction zone more or less efficiently. We prepared another batch containing eight samples grown at different gas flow rate values: 0.0024, 0.0072, 0.012, 0.018, 0.024, 0.030, 0.036 and 0.048 m/s. In order to be able to isolate the influence of this parameter on the YBCO final quality, we kept all the other processing parameters constant, considering the optimum parameters $T_{growth}$ ~ 795 $^oC$ and water vapour pressure ~ 7 mbar. Table 5.6 shows the main experimental conditions of this batch.

**Table 5.6**

Conditions for YBCO films grow with variable gas flow rates

| |
|---|
| Precursor solution prepared from commercial YBCO powder |
| Concentration = 1.5 M |
| LAO substrate |
| Optimized pyrolysis process |
| $T_{growth}$ = 795 $^{o}$C |
| Thickness = 0.4 μm |
| $P(H_2O)$ = 7 mbar |
| $P(O_2)$ = 0.2 mbar |
| Gas flow rate = variable |
| Reaction time = 150 min wet + 30 min dry |
| Standard oxygenation |

In figure 5.27 we show the XRD patterns of the present batch, where we can observe the high intensity of (*00l*) YBCO profiles denoting good crystallinity, and high *c*-axis oriented grain fraction. We also observe (*h00*) LAO substrate profiles and associated reflections due to Cu $K_\alpha$ radiation, denoted by $K_\beta$. The peak intensities of secondary phases at all gas flow rates and impurities found such as $Y_2O_3$, CuO and $BaCuO_2$ were compared with its respective (*005*) YBCO intensity, we determined that their intensities were minor than 1%. Figure 5.28 shows the FWHM values of the XRD ω-scan measurements of the (*005*) YBCO profile and are in the range $0.53^{o} \leq \Delta\omega \leq 1.27^{o}$. The profile is very broad when the gas flow rate is increased to 0.048 m/s.

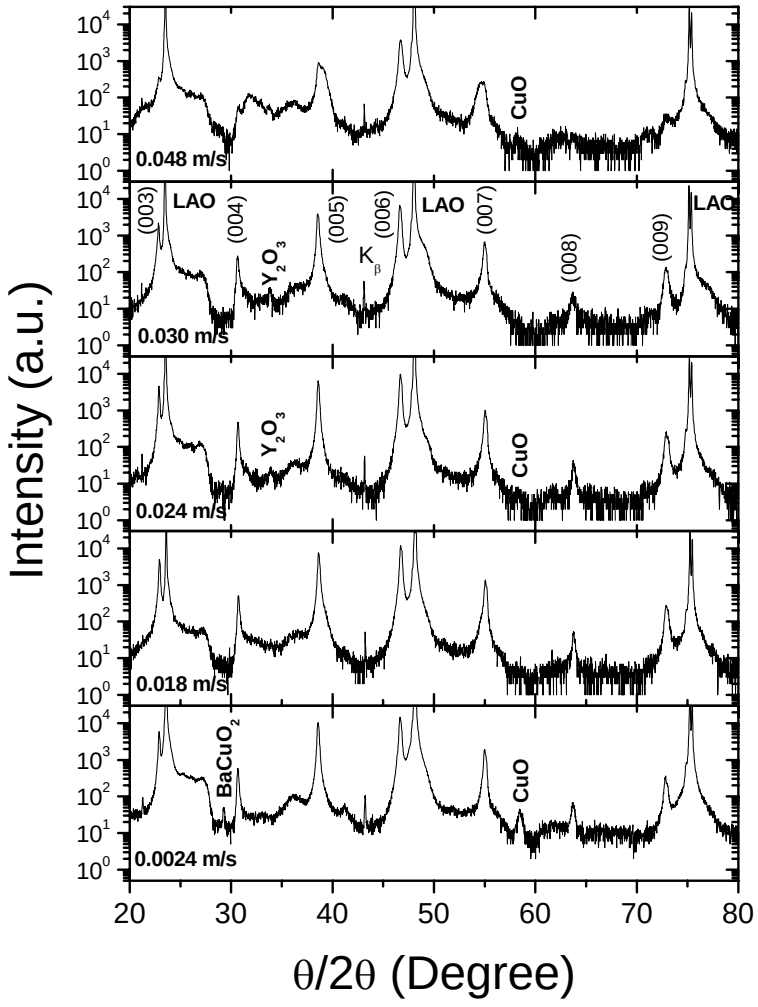


Figure 5.27. XRD patterns in logarithmic scale of YBCO films growth at different gas flow rates.

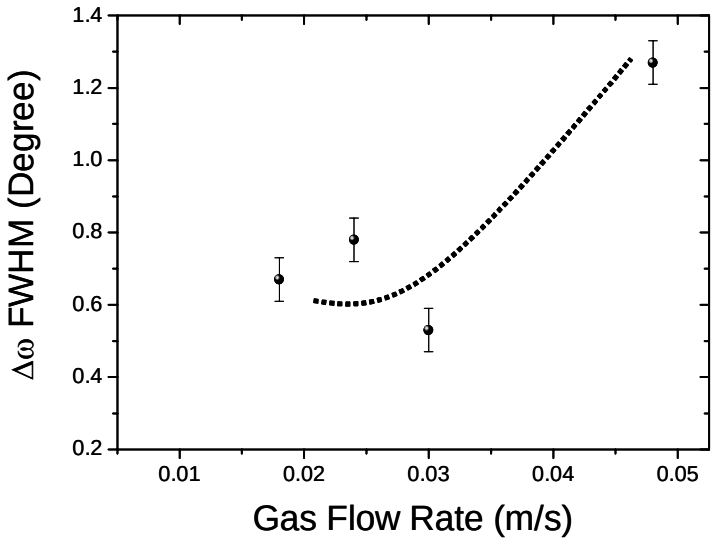


Figure 5.28. FWHM values of the XRD ω-scan measurements of the (*005*) YBCO profile for samples grown at different gas flow rates.

We performed micro-Raman measurements with the 10 μm laser spot, figure 5.29 shows the *polarized* Raman spectra of YBCO samples at different investigated gas flow rates. We only observe YBCO phonons modes in the films grown free of secondary phases or slight impurity traces at gas flow rates below 0.048 m/s. This would be in agreement with an increased amount of impurities and disorder observed in the Raman spectra and the poor crystalline structure observed in XRD and Δω value at high gas flow rate (0.048 m/s).

On the other hand, the uniaxial texture, determined by averaging five laser spots (10 μm), remains almost constant (δ ~ 0.90) for the investigated gas flow rate interval, as it is displayed in figure 5.30. This fact can be observed in the surface microstructure by SEM micrographs of the films (figure 5.31). A clear difference among gas flow rates can not be observed. These results evidence that any variation on the gas flow rate has not a direct influence on the uniaxial texture. However we have found influence of this parameter on the transport and superconducting performances. As it is clearly evidenced in $\rho_{300K}$ and $J_c$ measurements displayed in figures 5.32 and 5.33, respectively.

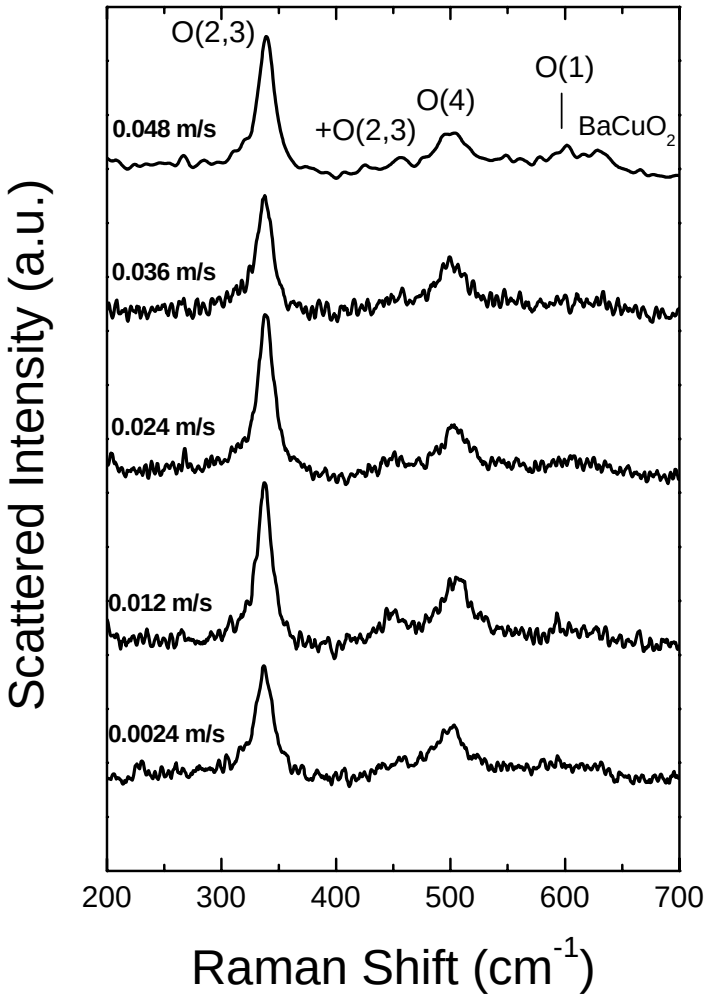


Figure 5.29. Polarized micro-Raman spectra of YBCO samples prepared from commercial YBCO powder at different gas flow rates.

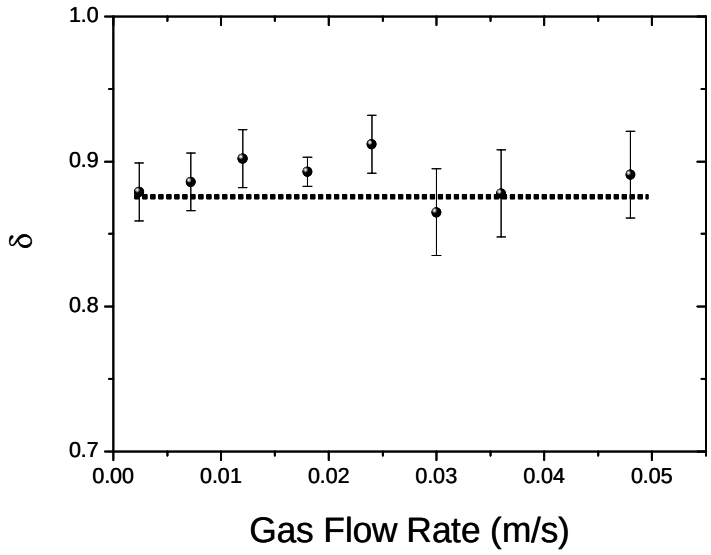


Figure 5.30. The uniaxial texture of YBCO samples growth at different gas flow rates. The δ values remains almost constant (δ ~ 0.90) for the investigated gas flow rate interval

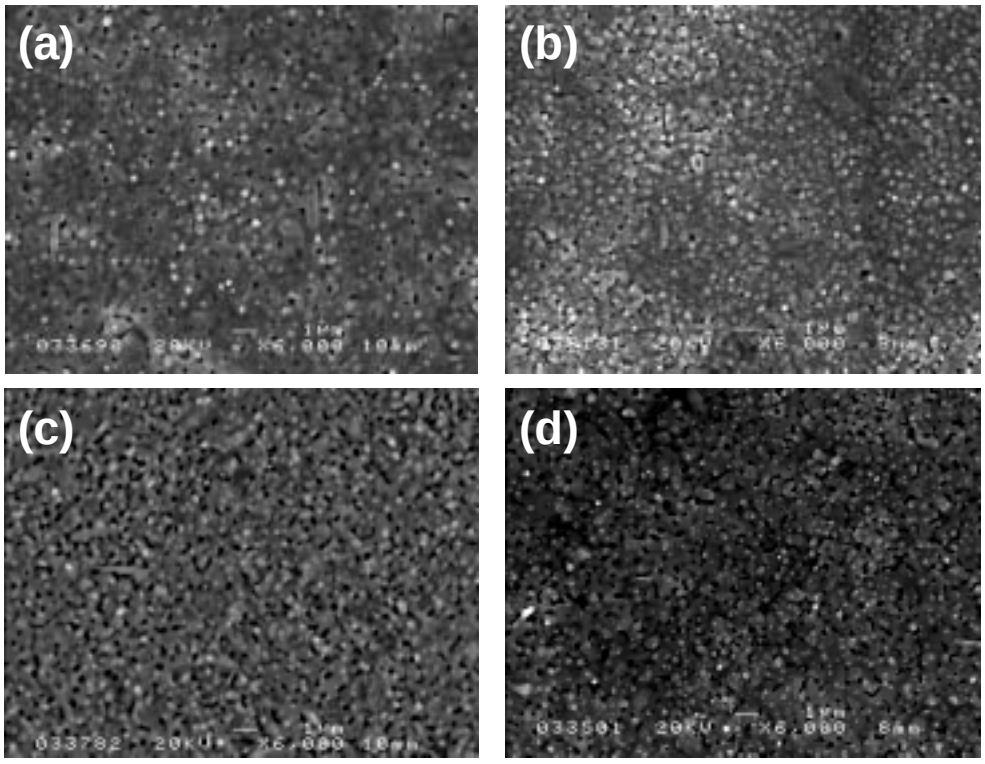


Figure 5.31. SEM micrographs of YBCO samples prepared from commercial YBCO powder at different gas flows rates (a) 0.0024, (b) 0.024 (c) 0.030 and (d) 0.048 m/s.

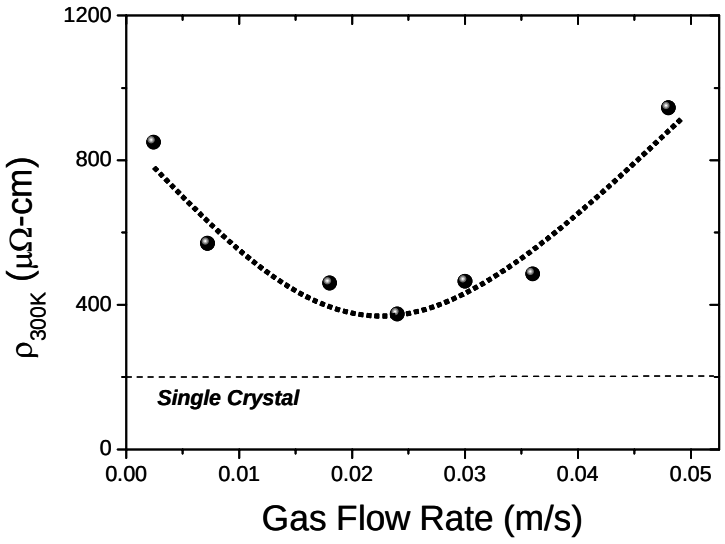


Figure 5.32. The $\rho_{300K}$ measurements of YBCO samples at different gas flow rates. Notice the minimum value at 0.024 m/s.

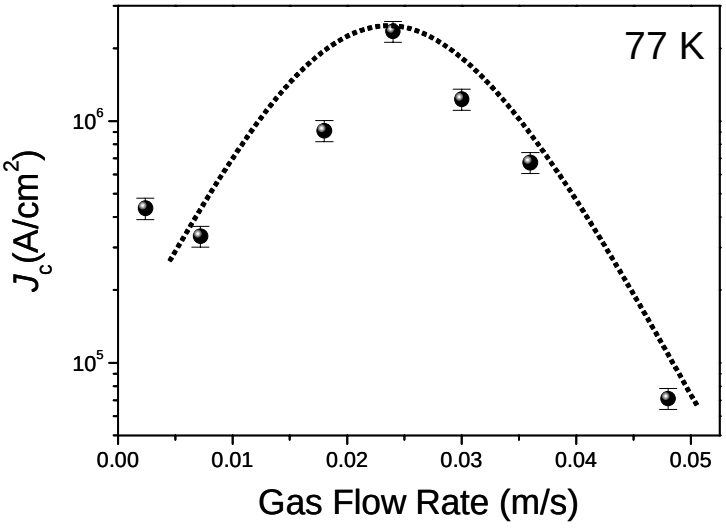


Figure 5.33. Critical current density measurements at different gas flow rates. Notice the maximum value at 0.024 m/s.

In the bibliography, Sathyamurthy *et al*[5.2,5.13] performed studies on TFA films grown onto STO and LAO single crystals at 800 $^{o}$C and P($O_2$) = 0.25 mbar. They observed that $J_c$ increases when the gas flow rate increases and obtained films with $J_c$ ~ 0.4 MA/cm$^2$, $\Delta\phi$ ~ 2.0 $^{o}$, $\Delta\omega$ ~ 0.80$^{o}$ and good crystallinity at its maximum gas flow rate.

From figures 5.32 and 5.33 we observe a clear correlation between the critical current density measurements at 77K and the normal state resistivity measurements. The $\rho_{300K}$ has a minimum value at 0.024 m/s and approaches the YBCO single crystal value (200 μΩ-cm) while the critical current density has a maximum value ~ 1.5 MA/cm$^2$ at the same gas flow rate. Particularly, the TFA film also displayed $\Delta\phi \sim 0.77^o$, $\Delta\omega \sim 0.78^o$ degree and $\delta \sim 0.90$ at 0.024 m/s. Thus, these values involve biaxial textured, *c*-axis oriented grains and high-$J_c$ YBCO TFA-MOD films.

Therefore, we propose that high and low gas flow rates may promote possibly the formation of impurities and/or structural disorder during YBCO growth. This could indicate that the diffusion boundary layer necessary for mass transfer of HF through a gas, in the Honjo model, (section 4.1) is affected by the gas flow rate and as we saw in equation (4.8) high flow rates involve high conversion rates ($R \propto \sqrt{V_g}$) producing a distorted growth. On the contrary, if the HF of the reaction is not swept out of the reaction zone efficiently at low gas flow rates, then, the YBCO growth front is blocked.

At the light of these results we concluded that there exists an optimum gas flow for a given geometry which is not correlated with *a*-axis oriented grains growth. However, this parameter is still in discussion in the scientific community, because the growth mechanisms are not known enough in order to apply a specific growth rate necessary to grow YBCO films and obtain the relation among the other growth parameters.

## 5.5. Porosity and sintering

Due to the intrinsic nature of the sol-gel compounds, there is a tendency to generate porous materials. We have observed that non-optimized growth conditions may lead to very porous YBCO TFA-MOD films, which can strongly degrade the superconducting properties. We have observed two possible sources of porosity in our TFA films studied. The first one related to low temperature treatments ($T_{growth} < 750\ ^oC$) while the second one is related to high temperature process ($T_{growth} > 750\ ^oC$). As we will show later, the formation of *a*-axis oriented grains and the formation of very porous films are strongly linked at low annealing temperatures, while on the other hand; pores may also remain

trapped within the *c*-axis grains when they grow at high annealing temperatures. In the first part of this section we have investigated the influence of porosity on the superconducting performances of YBCO TFA-MOD films in more detail. Micro-Raman has been used to determine the uniaxial texture and complementary results from SEM, resistivity and $J_c$ are presented.

In addition, we can then wonder if it is possible to reduce the porosity of YBCO TFA-MOD films after growing them. It is well known that porous polycrystalline solids can be further compacted through a sintering process which involves an atomic diffusion transport through the solid state. Thus, in the second part of this section we have investigated the influence of additional sintering treatments in two particular TFA films having strongly different *c*-axis fraction: (a) high concentration of *a*-axis grains $\delta = 0.30$ (b) high concentration of *c*-axis grains $\delta = 0.75$.

### 5.5.1. Porosity dependence with annealing temperature

We have observed in the TFA films studied in the 5.2.2 section that we only obtained high uniaxial texture values and dense YBCO films grown at high annealing temperatures ($T_{growth} > 750$ $^oC$), meanwhile we have also observed low uniaxial texture values and very porous YBCO films grown at low annealing temperatures ($T_{growth} < 750$ $^oC$), as showed in figure 5.17. To investigate the influence of porosity on the superconducting performances, first we performed a comparison between two particular samples with different porosity and uniaxial textures grown at different temperatures, 790 $^oC$ and 700 $^oC$, we kept the rest of processing parameters constant ($P(H_2O) = 7$ mbar, $P(O_2) = 0.2$ mbar, gas flow = 0.024 m/s).

Figure 5.34a represents a typical example of a well dense YBCO TFA-MOD film growth at 790 $^oC$ with $\delta \sim 0.9$. Here only some pores can be seen and a continuous and uniform matrix is observed. In contrast, the SEM micrograph of figure 5.34b illustrates the case of a high porous YBCO TFA-MOD growth at 700 $^oC$ with $\delta \sim 0.3$. As we can see, the differences between both pictures are evident. The two main features in figure 5.34b are the dominant presence of pores and a huge difference in the relative proportion of *a/b*-axis oriented grains and the *c*-axis ones although the average size

remains essentially unchanged (~1 μm). An interesting fact that we have observed from a careful examination of figure 5.34b is that pores seem to be always associated to the presence of *a/b*-axis oriented grains. The nucleation of *a*/*b* grains is still an open issue. There is some evidence that it could be related to high growth rates (*i.e.* for high water pressure) or to low growth temperatures[5.10,5.14] (see figure 5.10). We should keep in mind that the growth rate in the *ab* direction is much faster (~5 times) than along the *c*-direction. Thus when an *a/b*-axis grain nucleates it takes as much material as possible from the surrounding areas in order to increase its length perpendicular to the substrate. As a result there is a lack of material for the neighbouring *c*-axis grains to fill the gap between *a/b*-axis nucleation centers, and pores are thus formed (figure 5.35b). Therefore, in these YBCO TFA-MOD samples grown at low annealing temperatures ($T_{growth}$ < 745 $^{o}$C ), it seems that the main factor controlling the porosity is the relative concentration of *a/b*-axis oriented grains. This concentration can be quantified by micro-Raman spectroscopy measurements of the uniaxial texture, δ.

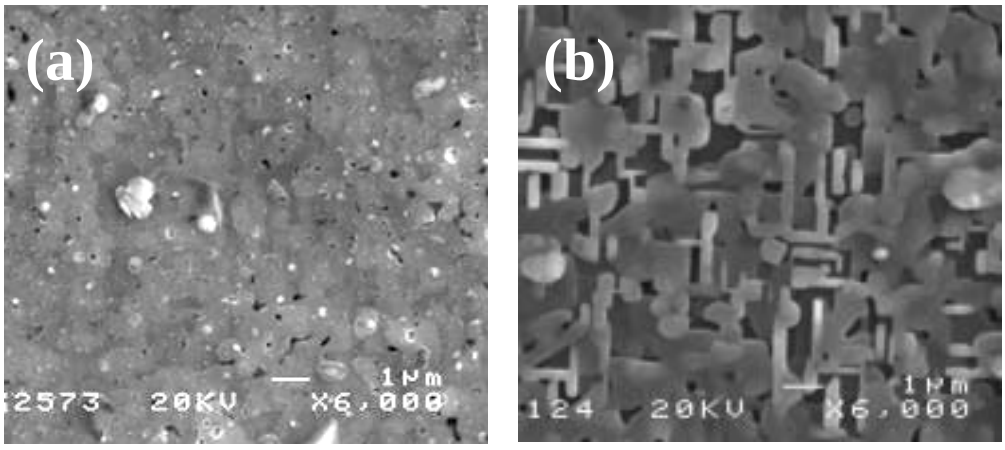


Figure 5.34. SEM micrographs of two different of YBCO TFA-MOD films: (a) well densified, low porosity film grown at 790 $^{o}$C (δ ~ 0.90); while (b) shows a high porosity film grown at 700 $^{o}$C with *a/b*-oriented grains (δ ~ 0.30); pores are mainly associated to these *a*-axis oriented grains.

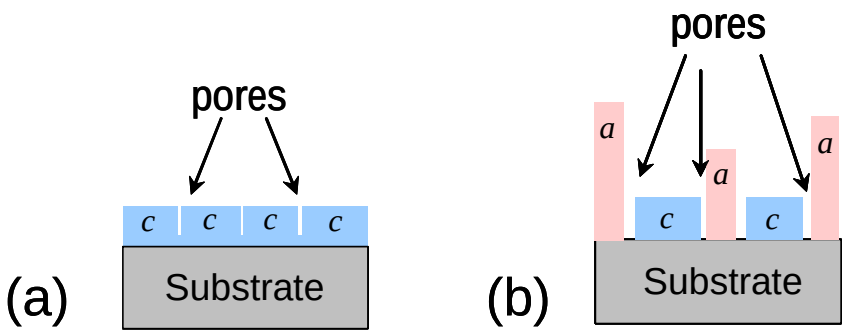


Figure 5.35. Scheme of porous formation in (a) fully *c*-axis oriented and (b) almost *a*-axis oriented film

The influence of porosity on normal state resistivity and superconducting properties of TFA films has been investigated. We found that the temperature dependence of the resistivity $\rho(T)$ is strongly modified for three particular films grown at 700 $^{o}$C, 750 $^{o}$C and 795 $^{o}$C (keeping the remaining processing parameters constant) having different δ values. A normal state linear behaviour $\rho(T) = \rho_o + AT$ with $\rho_o \approx 0$ is observed for all the samples properly grown[1.24] ($T_c$ = 90K), but the slope *A* is strongly dependent on δ. This is clearly represented in figure 5.36a. This linearity in $\rho(T)$ suggests that electrical transport is only governed by the *ab*-planes and that there is no *out-of-plane* or grain boundary contributions. These are typical features of high quality thin films such as those grown through vacuum processes [1.24,5.15].

Therefore, there exists a correlation between the normal state resistivity measured at 300K and the concentration of *c*-axis oriented grains, δ. Figure 5.36b shows the monotonous relation between δ and $\rho_{300K}$. The lowest measured values $\rho_{300K}$ ~ 200 μΩ-cm is comparable with that obtained in YBCO single crystals[5.8], thus confirming that optimized films are pores free. On the contrary, the enhancement of the resistivity value is due to an increase of the sample porosity which reduces the effective cross section of the sample $S_{eff}$ and increases the effective percolation length $l_{eff}$ through the sample[5.8]. The correlation showed in figure 5.36b confirms then that a correlation exists between porosity and *a*-axis grain concentration.

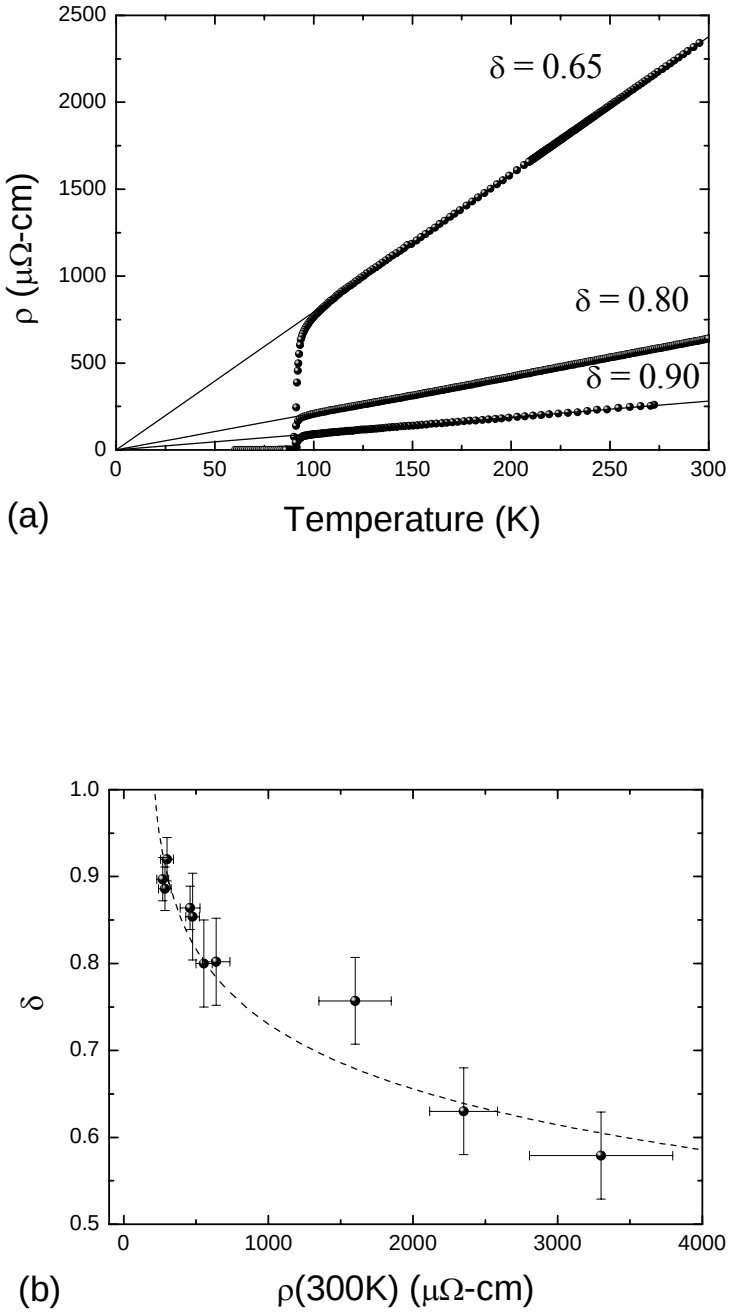


Figure 5.36. (a) Resistivity as a function of temperature for three samples grown at 700 $^{o}$C, 750 $^{o}$C and 795 $^{o}$C with $\delta \sim 0.65$, $\delta \sim 0.80$ and $\delta \sim 0.90$, respectively. (b) Relationship between the measured room temperature resistivity, $\rho(300K)$ and $\delta$ calculated from micro-Raman measurements for YBCO TFA-MOD films with different porosities. Dashed line is a guide to the eye.

We have also investigated the influence of *a*-axis grain concentration and porosity on the zero field critical current density, $J_c$ which deserves some attention. The temperature dependence of $J_c$ for three samples with different concentration of *c*-axis grains, δ, is presented in figure 5.37. We can observe that the main difference between the samples is the absolute value of their critical current, being the temperature dependence quite similar. Furthermore, higher critical currents ($J_c$ ~ 3MA/cm$^2$ at 77 K and $J_c$ ~ 20MA/cm$^2$ at 5 K) were obtained for the less porous samples which as seen above also correspond to the less resistive samples. This close relationship between both quantities is illustrated in figure 5.38, where room temperature resistivity is represented as a function of the critical currents measured at 5 K for samples having a wide range of δ (between 0.5 and 0.9). This clear correlation suggests that the dominant factor of the degradation of the critical current in the more porous samples is the reduction of the effective cross section.

On the other hand, in almost *c*-axis oriented and dense films (Figure 5.34a), the *c*-axis growth mode is performed by islands. This is a typical growth mode of *c*-axis grains for MOD process and produces the formation of small pores trapped within *c*-axis grains (residual porosity), as schematically shown in figure 5.35a. Although the precise dependence of the *c*-axis oriented grains concentration on the growth conditions deserves more experimental studies, it seems that the annealing temperature and the water pressure of the reaction atmosphere are key factors. In particular, we have systematically observed that on samples prepared from commercial YBCO powder (section 5.2.2), when we kept the other processing parameters constant, higher annealing temperatures correspond to higher values of *c*-axis oriented grains, ***i.e.***, less fraction of *a/b*-grains (figure 5.17), and therefore low resistivity samples as clearly represented in figure 5.39. However, residual porosity still exists for growth temperatures higher than 750 $^oC$. Figure 5.39 shows a dependence on porosity independent on δ for this temperature range ($T_{growth}$ > 750 $^oC$).

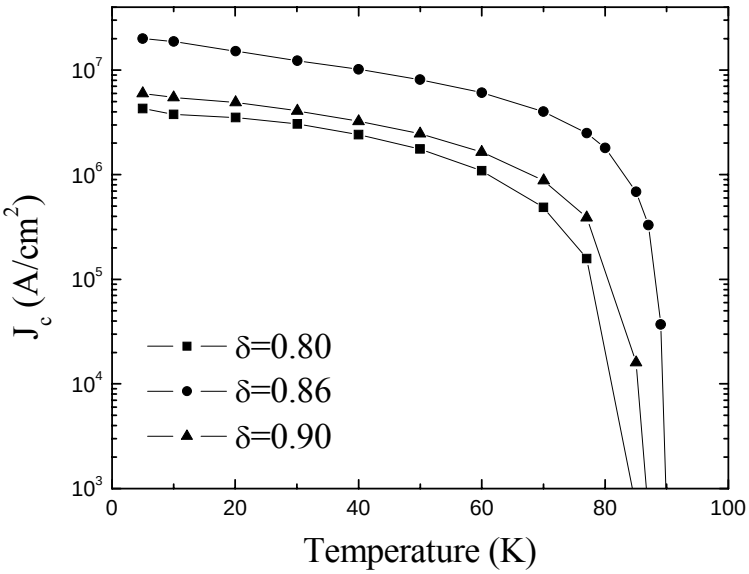


Figure 5.37. Temperature dependence of the critical current density in YBCO TFA films having different concentration of *c*-axis oriented grains and a similar thickness ≈ 300 nm.

At the light of the results obtained, we may conclude that two sources of porosity exist. The first one related to low annealing temperatures ($T_{growth}$ < 750 $^oC$). The growth of *a*-axis oriented grains and the formation of very porous films are strongly linked at low annealing temperatures. A relationship among *a*-axis growth, porosity, resistivity and superconducting properties has been established. On the other hand, the second source of porosity (though in a less extreme case) is related to high annealing temperatures ($T_{growth}$ > 750 $^oC$). Residual porous remain trapped within the *c*-axis grains when they grow. In the next section we will show how to eliminate the porosity in TFA films by a sintering process.

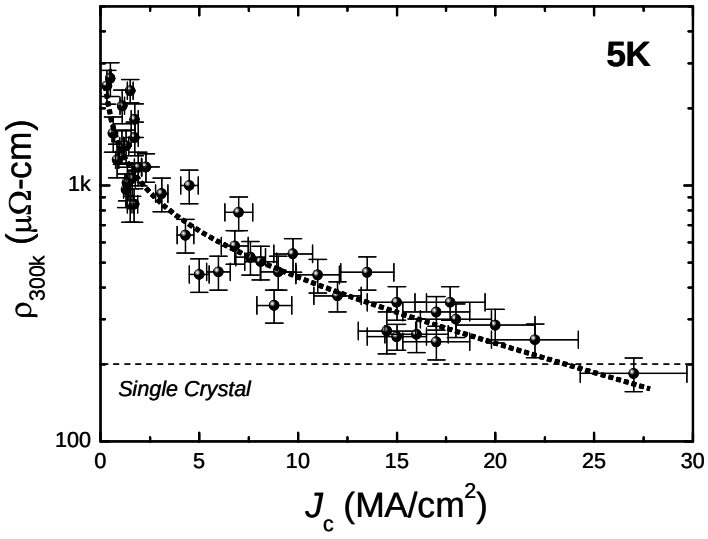


Figure 5.38. Room temperature resistivity $\rho(300K)$ as a function of the critical current density $J_c$ at 5K for YBCO TFA-MOD films with different porosities.

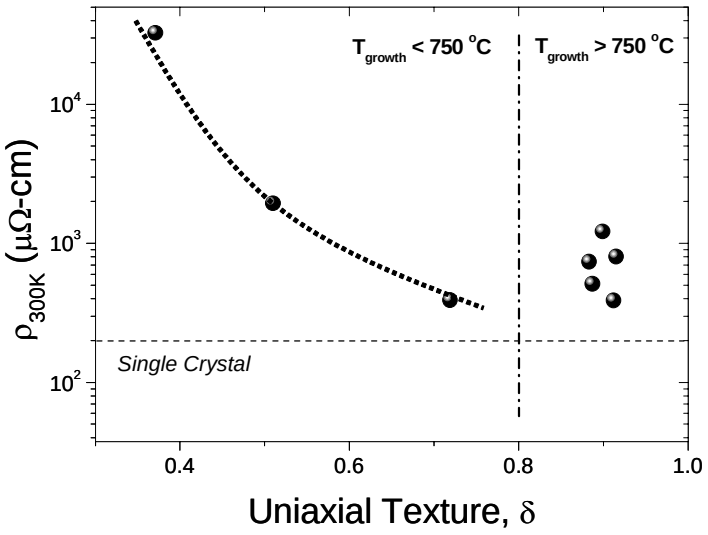


Figure 5.39. Dependence of normal resistivity on uniaxial texture for TFA films grown at low (< 750 °C) and high (> 750 °C) annealing temperatures.

### 5.5.2. Sintering of porous YBCO TFA films

As we have observed in section 5.2, the pores may be reduced by a better densification of YBCO films grown at high annealing temperatures ~ 795 $^{o}$C. We performed two experiments in samples with high porosity grown at low annealing temperature (< 750 $^{o}$C) to prove if a sintering process is able to improve the connectivity among YBCO grains. The first TFA film was grown at 750 $^{o}$C with 250 minutes of reaction time ($P(H_2O)$ = 7 mbar, $P(O_2)$ = 1 mbar, gas flow = 0.024 m/s), the sample shows a large *a*-axis grain concentration as shown in SEM micrographs of figure 5.40a. Raman measurements of the uniaxial texture of the as-grown film was $\delta \sim 0.31$, critical temperature $T_c$ = 87 K, $J_c$(5K) = 0.9 KA/cm$^2$ and normal state resistivity was equal to $\rho_{300K} \sim 3840$ μΩ-cm. After a sintering process at 790 $^{o}$C for 12 hours of reaction time with $P(H_2O) \approx 0.1$ mbar and all the rest of processing parameters were kept constant ($P(O_2)$ = 1 mbar, gas flow = 0.024 m/s), we observed that the uniaxial texture and critical temperature were unchanged, $\delta \sim 0.39$ and $T_c$ = 87 K, respectively, but now the film showed a noticeable drop in the normal state resistivity $\rho_{300K} \sim 350$ μΩ-cm and an increases in the critical current density, $J_c$(5K) = 0.19 MA/cm$^2$. Figure 5.40b shows the SEM micrograph of this sample after the sintering process and we can observe the improvement of the connectivity of YBCO grains although the uniaxial texture and critical temperature remained unchanged.

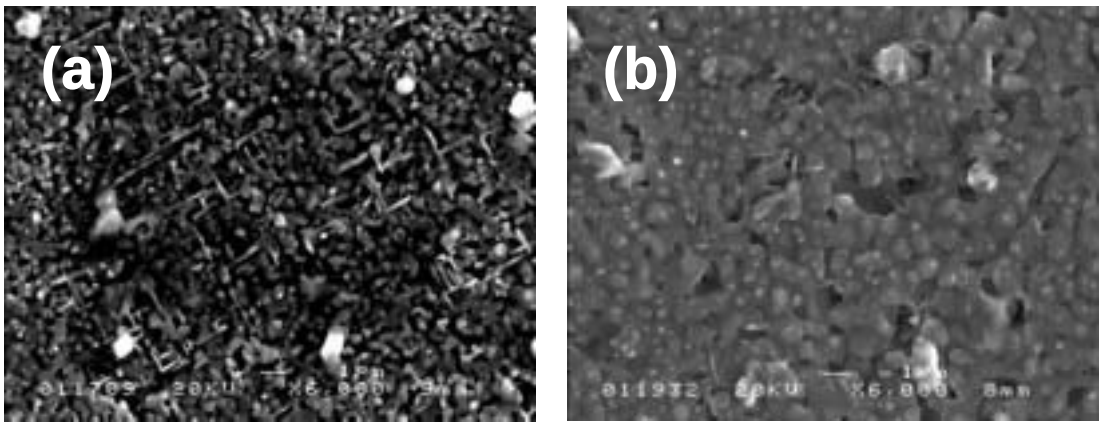


Figure 5.40. (a) as-grown YBCO samples at 750 $^{o}$C for 250 minutes, (b) the same sample after sintering process at 790 $^{o}$C for 12 hours. Notice the reduction of the porosity although the uniaxial texture was unchanged.

The second YBCO TFA film was grown at 700 $^{o}$C with 150 minutes of reaction time and we kept all the remaining processing parameters constant ($P(H_2O)$ = 24 mbar, $P(O_2)$ = 0.2 mbar, gas flow = 0.024 m/s). The sample showed a higher *c*-axis concentration as determined by Raman measurements, the uniaxial texture of the as-grown film was $\delta \sim 0.75$, the critical temperature $T_c$ = 89 K, $J_c$(5K) = 4.4 MA/cm$^2$ and normal state resistivity was equal to $\rho_{300K} \sim 605$ μΩ-cm (Figure 5.41a). After a sintering process at 830 $^{o}$C for 12 hours of reaction time with $P(H_2O) \approx 0.1$ mbar and all the rest of processing parameters kept constant ($P(O_2)$ = 0.2 mbar, gas flow = 0.024 m/s), the uniaxial texture and critical temperature were unchanged too, $\delta \sim 0.80$ and $T_c$ = 89 K, but we observed that the normal state resistivity value dropped to $\rho_{300K} \sim 205$ μΩ-cm and the critical current density slightly increased, $J_c$(5K) = 5.3 MA/cm$^2$, as illustrated in figure 5.41b.

At the light of these results, we may conclude that the transport properties of YBCO TFA-MOD films, such as normal state resistivity and $J_c$, are highly dependent on the porosity which is seen to be linked to *a*-oriented grains in samples grown at low annealing temperatures (< 750 $^{o}$C). However, still a residual porosity which is seen to be linked to trapped pores within *c*-oriented grains grown at high temperatures (> 750 $^{o}$C), may be present for high δ-values. In any of the cases porosity reduction will bring to an enhancement of transport superconducting properties. Sintering process is seen to be a possible post-processing treatment to reduce the porosity linked to *a*- or *c*-oriented grains.

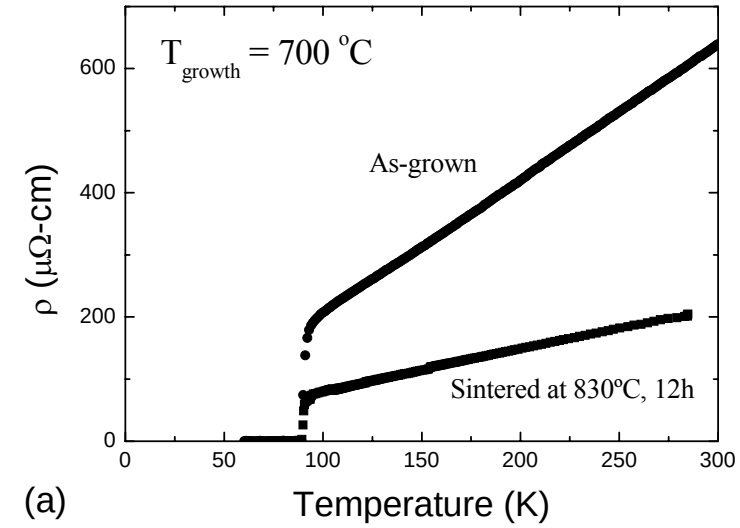


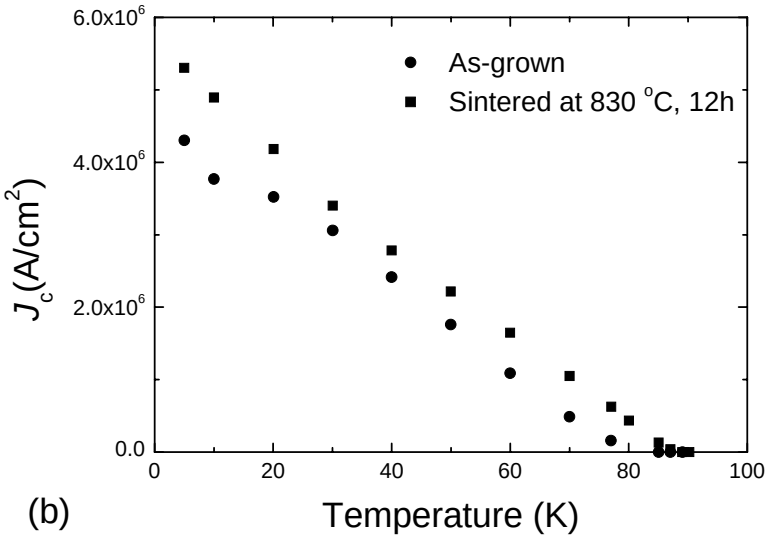


Figure 5.41. (a) Change in the temperature dependence of the resistivity induced by the sintering process (830 °C for 12 hours) in a sample grown at 700 °C for 150 minutes. (b) Measurement of $J_c$(T) for the sample before and after the sintering process

## 5.6. YBCO TFA films grown with optimized conditions

All the results obtained in the previous sections, helped us to optimize the experimental processing parameters used in the superconductivity group at ICMAB to obtain highly biaxial textured YBCO TFA-MOD films with high superconducting properties and high reproducibility. The processing parameters are shown in table 5.7.

**Table 5.7**

Growth conditions for optimized YBCO TFA-MOD films

| |
|---|
| Precursor solution prepared from Y, Ba and Cu oxides |
| Concentration = 1.5 M |
| LAO substrate |
| Optimized pyrolysis process |
| $T_{growth}$ = 795 $^{o}$C |
| Reaction time = 150 min wet + 30 min dry |
| $P(H_2O)$ = 7 mbar |
| $P(O_2)$ = 0.2 mbar |
| Gas flow rate = 0.024 m/s |
| Standard oxygenation |
| Thickness = 0.40 μm |

The concentration of *c*-axis oriented grains was found to be higher than 90% by means of μRS and XRD. Figure 5.42 displays a typical θ–2θ XRD and polarized micro-Raman spectra corresponding to a pure YBCO TFA-MOD sample deposited on a LAO single crystal substrate, while figures 5.43a-b display typical ω- and ϕ-scans. A high quality *out-of-plane* and *in-plane* texture is achieved for high annealing temperature ~ 795 $^{o}$C: ω- and ϕ-scans of these samples lead to FWHM values of $\Delta\omega = 0.48^{o}$ for the (*005*) reflection and $\Delta\phi = 1.0^{o}$ for the (*102*) reflection, respectively. SEM micrographs showed that very low porosity was achieved in these optimized films. The same conclusion can be reached from cross section TEM micrographs (figure 5.44) of these optimized samples, which show a continuous structure all across the film without any evidence of

pores or secondary inclusions. These films grown on LAO substrates also display a very sharp interface quality while the film crystallinity is often slightly perturbed after the growth of a few tens of nanometres from the interface where a structure full of stacking faults is usually observed (see figure 5.44b), a feature which has also been reported by others authors in YBCO films grown by TFA route[5.16,5.17].

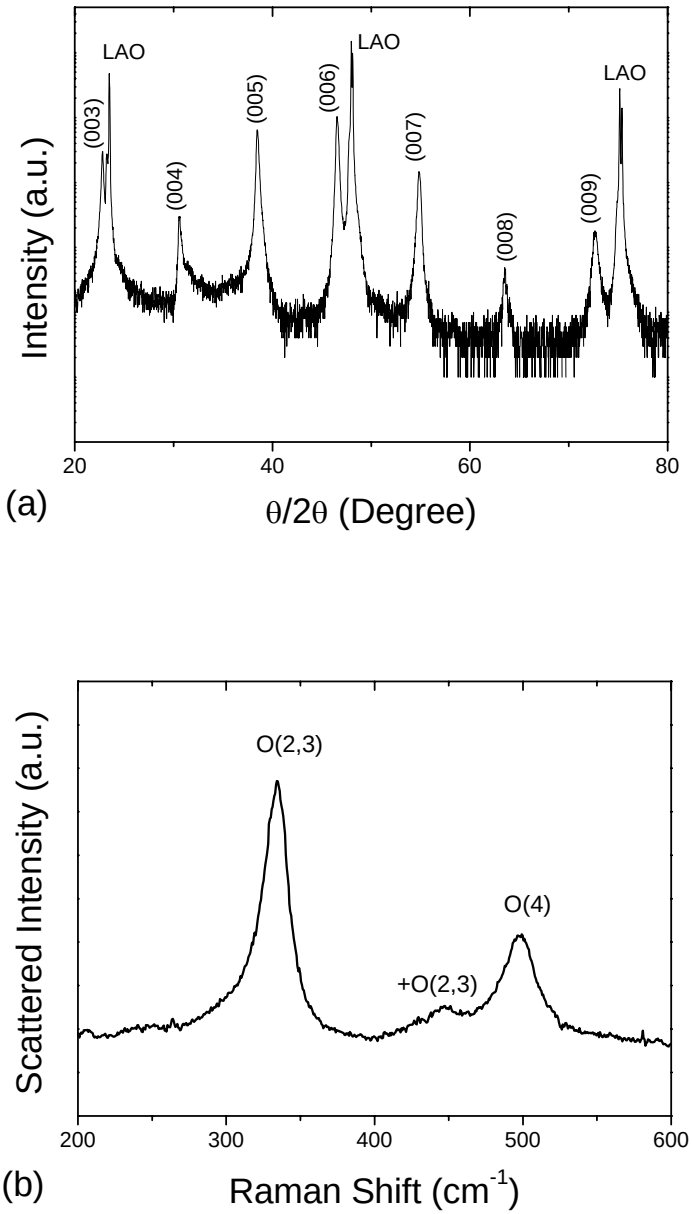


Figure 5.42. YBCO TFA-MOD sample with high biaxially texture, $J_c$(5K) ~ 27 MA/cm$^2$ and $J_c$(77 K) ~ 3.2 MA/cm$^2$, obtained at the superconductivity group at ICMAB. (a) XRD pattern and (b) Polarized Raman spectra with only YBCO phonon modes.

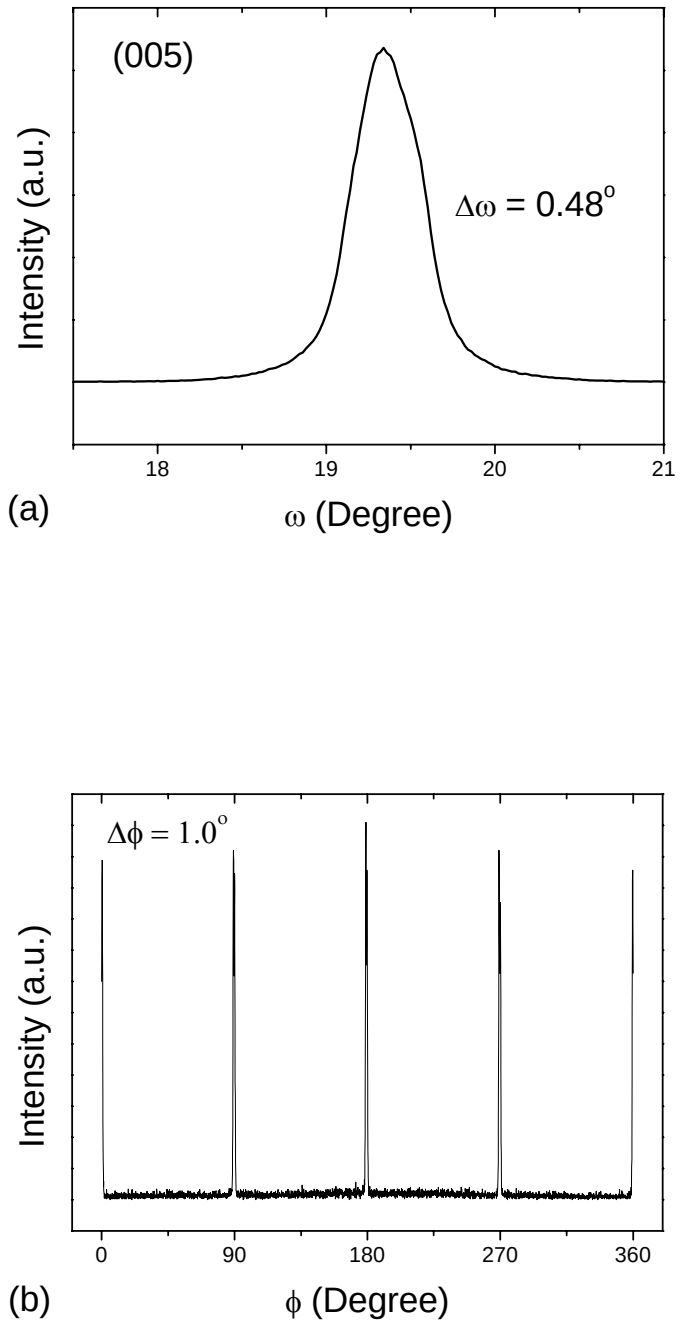


Figure 5.43. (a) ω-scan of the (*005*) reflection to determine the *out-of-plane* texture, $\Delta\omega = 0.48^{o}$ and (b) ϕ-scan of the (*102*) reflection used to determine the *in-plane* texture, $\Delta\phi = 1.0^{o}$, of a YBCO TFA-MOD film.

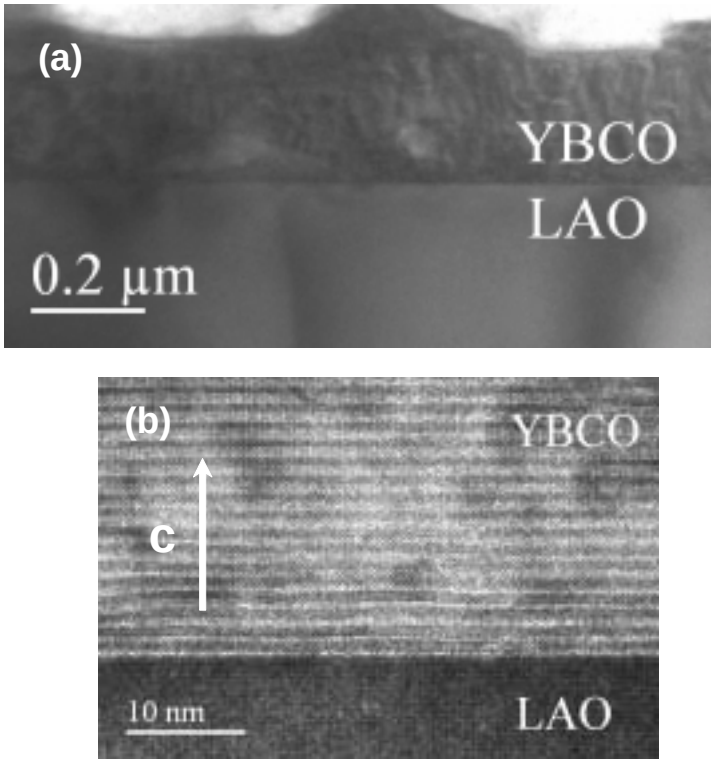


Figure 5.44. Cross section TEM micrographs of an optimized YBCO TFA-MOD film: (a) low magnification wide view of the film, (b) detail of the interface of the YBCO film with the LAO substrate.

## Conclusions

High quality epitaxial YBCO films on LAO single crystal substrate have been obtained using TFA precursors. The influence of growth parameters on the final film quality (structure and superconducting properties) has been investigated. We have shown the influence of growth temperature, water pressure and gas flow rate on final microstructure in samples where the annealing time has been carefully adjusted to reaction completion (150 minutes) determined by monitoring the $BaF_2$ Raman signal. These three parameters (growth temperature, water pressure and gas flow rate) are seen to be the most important. The influence of growth temperature becomes apparent due to the strong dependence of the reaction kinetics. We observed that, at high growth temperatures in acetates- and oxides-based samples the $\delta$, $J_c$ and $\rho$ values evidence an improving of *c*-axis oriented grains and superconducting performances, meanwhile low temperatures treatments evidence *a*-axis oriented films and low superconducting performances. The chemical reaction for YBCO phase formation requires water vapour

pressure in order to decompose the $BaF_2$ intermediate phase. We observed that low water vapour pressure involve low conversion rates and not enough HF release, this might not complete the reaction, or even entrap HF, precipitate of precursor phases or generate disorder; meanwhile for high water vapour pressure we have a high conversion rate and obtain a distorted growth front producing a distorted growth. We may conclude that the water vapour pressure values optimum for the preparation of highly *c*-axis oriented and high-$J_c$ YBCO films are in the range between 6 mbar ≤ $P(H_2O)$ ≤ 11 mbar. On the contrary, by mean of the gas flow rate more o less moisture ($H_2O$) is carried in the reaction zone and HF of the reaction is swept out from the reaction zone more or less efficiently. Thus, low gas flow rates may block the YBCO growth front because the HF of the reaction is not swept out of the reaction zone efficiently; whilst high flow rates involve high conversion rates inducing a distorted growth. We concluded that there exists an optimum gas flow for a given geometry which is not correlated with *a*-axis oriented grains growth. However the gas flow rate is still in discussion in the scientific community, because the growth mechanisms are not enough known to date. The highest critical currents ($J_c$ = 3.2 MA/cm$^2$ at 77 K and 27 MA/cm$^2$ at 5 K) and the lowest normal state resistivity $\rho_{300K}$ ≈ 200 μΩ-cm) were found in YBCO TFA films grown at 795 $^oC$, $P(H_2O)$ = 7mbar, $P(O_2)$ = 0.2 mbar and gas flow rate = 0.024 m/s.

SEM observations have shown that porosity is the main microstructural feature deeply modified by the annealing temperature, being strongly enhanced in films annealed at low temperatures. The influence of this parameter has been evidenced by the close correlation existing among uniaxial texture, normal state resistivity and the critical currents in samples with different degrees of porosity. There exist two sources of porosity on the YBCO TFA films, one related to *a*-oriented grains growth and other not related to *a*-oriented grains growth (residual porosity). High-$J_c$ YBCO films are obtained if the parameters δ and normal state resistivity, ρ, are optimized. The sintering process is a very useful post-processing to close pores, but it is a solid state process very slow thus it is not very practical for fast production.

In conclusion, the present work shows that the preparation of high performance YBCO TFA-MOD films actually does not require the use of vacuum processes and hence our work gives further support to the view that chemical solution growth techniques have a

great potential to become competitive, from the performance and cost points of view, with the vacuum techniques. The advancement on the understanding of the relationship among microstructural parameters and superconducting performance of YBCO films should enable the optimization of the growth conditions on metallic substrates.

# Chapter 6

## *Intermediate Phases in the YBCO-TFA Conversion from Precursor Phases*

In recent years, considerable efforts have been devoted to better understanding the reaction mechanism and to optimize the processing of the TFA-MOD process for YBCO growth. Understanding of the nucleation process is particularly important for the fabrication of technologically viable thick YBCO CC. The mechanism of crystallization in the TFA-MOD process has not been well understood, because the method includes the process of crystallization from liquid solution (gel), which is different from other vapour deposition methods (section 1.3.3).

Nowadays the intermediate phases proposed to obtain YBCO TFA are still an open issue. The most accepted intermediate phases are $BaF_2$, CuO and $Y_2Cu_2O_5$ as suggested by Smith *et al*[1.28], based on their investigations on YBCO MOD grown onto LAO single crystal. On the other hand, Araki *et al*[1.26] proposed the intermediate phases CuO and Y-Ba-O-F (oxyfluoride) from their observations on YBCO TFA-MOD samples characterized by TEM and XRD studies. In addition, Venkataraman *et al*[6.1] stated the same intermediate phases like Smith *et al* but followed by a series of plausible individual steps producing $Y_2O_3$, Ba(OH)F and $BaCuO_2$ on their YBCO samples prepared onto Ni-3% RABiTS substrates by $BaF_2$ process and characterized by XRD and micro-Raman studies. Moreover, Wu *et al*[6.2] suggested the intermediate phases $Cu_2O$ and Y-Ba-O-F (oxyfluoride) based on their studies on YBCO films grown onto STO substrates. Finally, McIntyre *et al*[4.9] assumed that the intermediate film consist of $BaF_2$, CuO and $Y_2O_3$ prior to decomposition of $BaF_2$ and formation of $BaCuO_2$ and $Y_2Cu_2O_5$ to form YBCO samples onto LAO substrates prepared by post-annealing process characterized by TEM and XRD studies.

As we saw in chapter 4, the study by micro-Raman spectroscopy of the precursor phases has been applied to identify precursor phases related to the solution precursor and pyrolysis process. In this chapter, we will present the results of our preliminary studies toward further knowledge on the mechanisms of the YBCO nucleation and the role of the intermediate phases, such as $BaF_2$, $Y_2O_3$, CuO and $Y_2Cu_2O_5$, in the growth of the YBCO phase in the TFA-MOD process, by using precursor films which were deposited on LAO substrates and either quenched at different temperatures of the heating ramp or grown at temperatures below 700 $^oC$. By quenched samples we mean precursor films that were heated up to a particular temperature and then quickly pulled out from the furnace to room temperature. All specimens were studied by XRD and micro-Raman, while TEM techniques were used for selected specimens.

## 6.1. Quenched films at low temperatures

We showed in section 5.6 that the members of the superconductivity group at ICMAB were able to growth YBCO films onto LAO substrate at 795 $^oC$ with excellent superconducting performances. Now, in this section, we shall focus on the study of the role of the YBCO intermediate phases after the pyrolysis step when the heating ramp arrives to 650, 700 and 750 $^oC$. The quenched samples studied in this section, called *samba011*, *samba036* and *samba035* were quenched at 650, 700 and 750 $^oC$, respectively. The main features of these samples are shown in table 6.1. The samples were quenched by quickly pulling them out from the furnace to room temperature. The quenched profile used is shown in figure 6.1.

As we saw in chapter 4, the CuO, $BaF_2$ and $Y_2O_3$ phases resulted from the decomposition of the metal trifluoroacetates. The presence of these phases were corroborated from electron diffraction patterns of the cross section TEM specimens[6.3] in pyrolyzed films fired at 400 $^oC$ and P(O2) = 1 bar in a study performed by members of the superconducting group at ICMAB. They also detected the presence of $Cu_2O$ and $Ba_{1-x}Y_xF_2$ phases as shown in figure 6.2.

**Table 6.1**

Conditions of samples quenched at low temperatures

| |
|---|
| Precursor solution prepared from YBCO powder |
| Concentration = 1.5 M |
| LAO Substrate |
| Optimized pyrolysis process |
| Heating ramp = 500 $^{o}$C/h |
| P($H_2O$) = 7 mbar |
| P($O_2$) = 0.2 mbar |
| Gas flow rate= 0.0024 m/s |
| Quench temperature = variable |

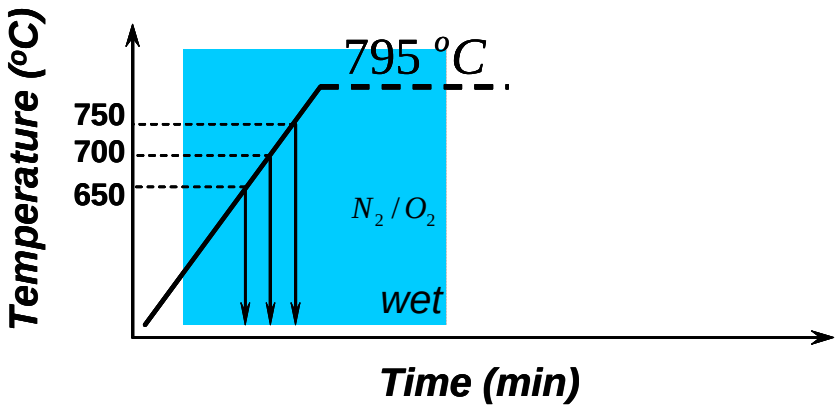


Figure 6.1. Firing profile of samples quenched at 650, 700 and 750 $^{o}$C. Humidified gas introduced at 110 $^{o}$C. The samples were quickly pulled out from the furnace to room temperature at the quench temperature.

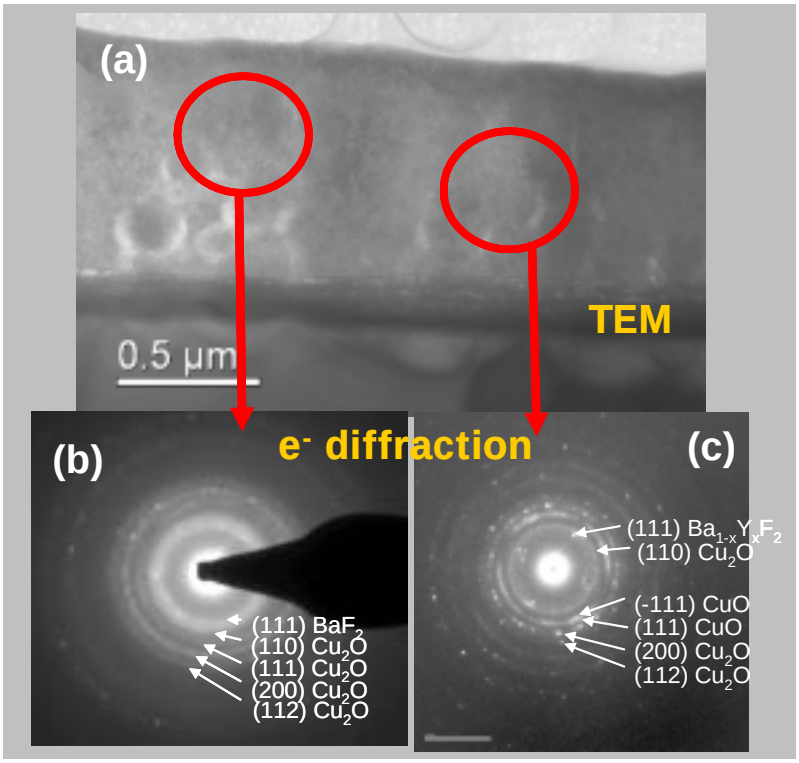


Figure 6.2. (a) Cross sectional TEM micrographs of a sample after the pyrolysis process. (b) and (c) electron diffraction patterns of two selected areas.

We have performed long accumulation time XRD measurements (12 hours) of TFA film after the pyrolysis step to characterize the possible phases in the structure. Figure 6.3 shows the XRD pattern where the presence of CuO, $BaF_2$, $Ba_{1-x}Y_xF_2$ and $Y_2O_3$ phases are clearly detected. We have assigned the peak at $2\theta = 26$ degree to the (*111*) $Ba_{1-x}Y_xF_2$ reflection in agreement with Yoshizumi *et al*[4.18], which evidences the existence of a solid solution between barium and yttrium in the $BaF_2$ phase. On the other hand, the presence of oxy-fluorides, *i.e.* BaF-O and $Ba_{1-x}Y_xF$-O compounds, in the precursor films can not be discarded, as we will show in the next sections, since they could not be distinguished by XRD due to the small shifts in lattice parameters with respect to the $BaF_2$ and $Ba_{1-x}Y_xF_2$ phases[4.18]. However, we did not see any peak of the $Cu_2O$ phase in the XRD pattern; this fact may be attributed to the small nanometric size of the $Cu_2O$ nanocrystallites or amorphous like phase in the pyrolyzed film which would not be thus detected by XRD.

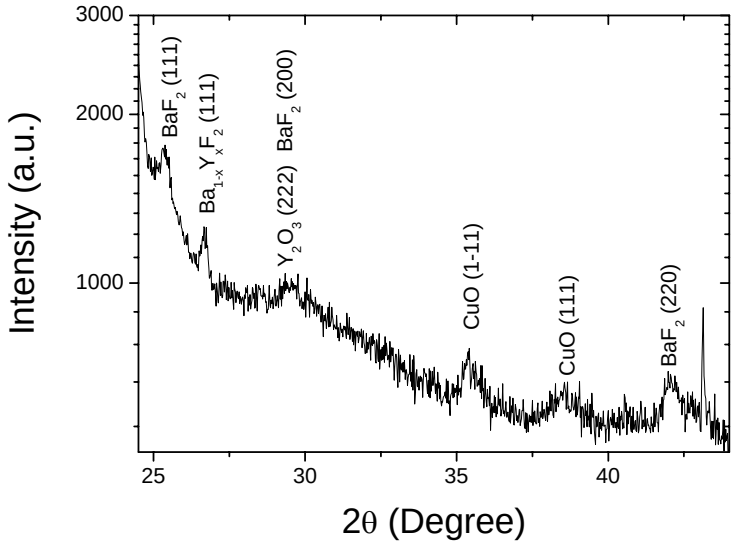


Figure 6.3 Logarithmic XRD pattern, measured with 12 hours accumulation time, of a TFA film after pyrolysis step. The $BaF_2$, $Y_2O_3$, CuO nanocrystalline phases resulted from the decomposition of metaltrifluoroacetates. The curved background is due to the presence of (*100*) LAO profile tail at ~ 23 degree.

As it is expected, the standard XRD patterns (~1 hour of accumulation time) of the quenched samples at 650°, 700° and 750 °C did not show any clear signature of any intermediate or $YBa_2Cu_3O_{6.5}$ phases, we just observe a blurred signal of (*111*) $BaF_2$ profile mixed with the XRD background.

The chemical overall reaction, equation (6.1), during the heat treatment requires humidified gas, to decompose $BaF_2$ and thus grow YBCO.

$$0.5Y_2O_3 + 2BaF_2 + CuO + 2H_2O \xrightarrow{O_2} YBa_2Cu_3O_{7-\delta} + 4HF(g), \quad (6.1)$$

Then, we turn to micro-Raman spectroscopy to complement the information on these quenched films between 650 and 750 °C. We have added the Raman spectra of a TFA film after the pyrolysis step at 400 °C and of a sample quenched at 795 °C for completeness. The micro-Raman spectra, shown in figure 6.4, display the appearance of the CuO phase as the first crystalline phase and the presence of additional phases, $BaF_2$ and $Y_2Cu_2O_5$, which can only be clearly identified above 750 °C. The micro-Raman

spectrum of the film just after the optimized pyrolysis process, shows broad CuO phonon band signals, at 288 $cm^{-1}$, 330 $cm^{-1}$ and 630 $cm^{-1}$ (see figure 6.4). It is important to remark that the $Cu_2O$ phase detected in the pyrolyzed sample by electron diffraction was not observed in the Raman spectra of figure 6.4 not even at 795 $^oC$ though $Cu_2O$ has a strong Raman phonon mode at ~ 217 $cm^{-1}$[6.4]. The presence of scattered intensity from the LAO phonon at ~489 $cm^{-1}$ signal indicates that the laser radiation reached the substrate interface. As the quenched temperature is increased, the CuO phonon bands get sharper indicating that the CuO nanocrystallites grow in size following a coarsening process. A possible explanation of CuO nanocrystals coarsening when the temperature is increased, as shown in figure 6.5, it may just be due to the major density of CuO than $BaF_2$ and $Y_2O_3$ phases imposed by TFA salts stoichiometry $Y(TFA)_3 : 2Ba(TFA)_2 : 3Cu(TFA)_2$. These results above obtained are in accordance with Raman measurements of Venkataraman *et al*[6.4], which just observed the presence of CuO Raman signal for growth temperatures between 650 and 740 $^oC$. Moreover, Araki *et al*[1.26] also reported the presence of many CuO nanocrystallites dispersed uniformly in an amorphous matrix film from their XRD patterns and TEM micrographs during heat treatment.

We have evidenced the coarsening of the CuO nanocrystals by increasing the quenched temperature and observing that the Raman peak associated to the CuO-$A_g$ mode gives a stronger signal that shifts from 288 to 298 $cm^{-1}$ and sharpens the corresponding FWHM from 34 $cm^{-1}$ to 15 $cm^{-1}$[6.5,6.6], as displayed in figures 6.6 and 6.7, respectively. On the other hand, micro-Raman shows that any possible nanocrystallites of $Cu_2O$ present after the pyrolysis process (as seen by TEM) does not crystallize (coarsen) as we increase the temperature.

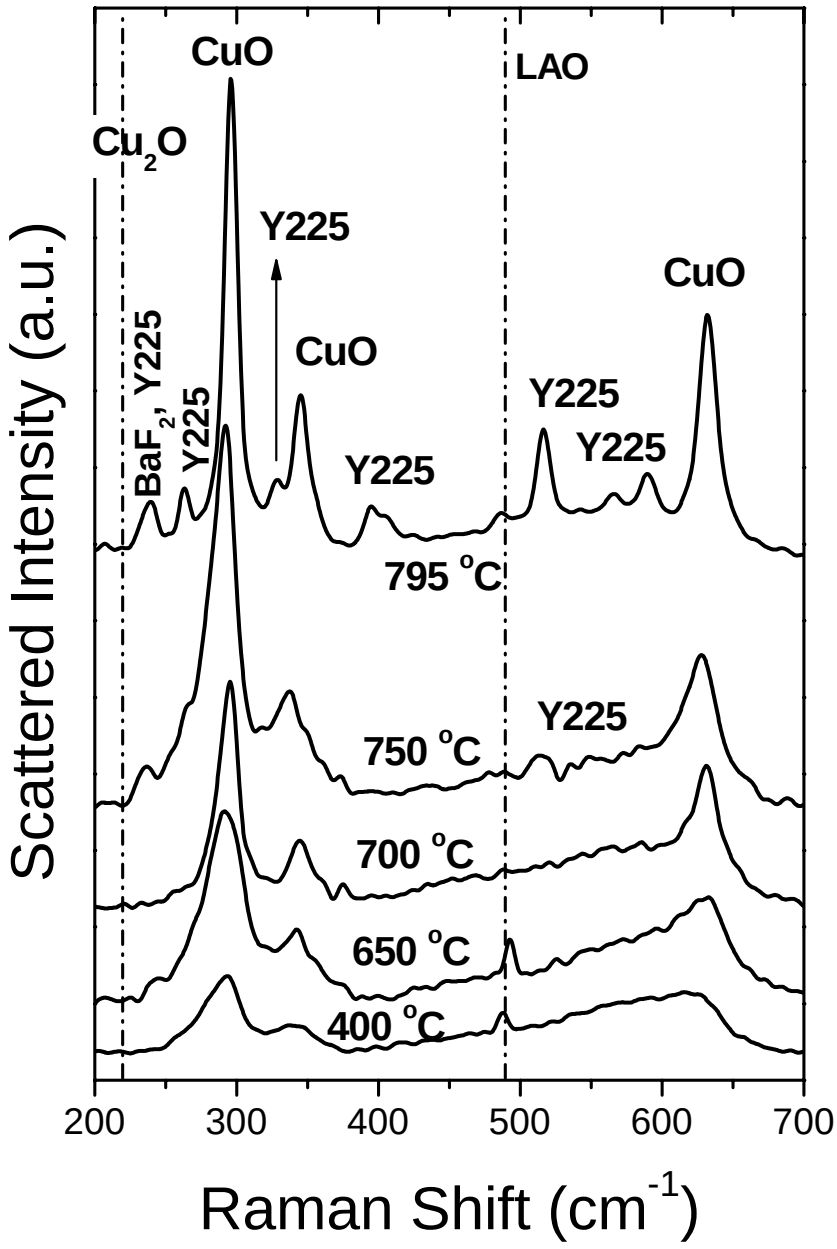


Figure 6.4. Raman spectra of samples quenched at 400, 650, 700, 750 and 795 $^{o}$C. Notice the crystallization of CuO nanocrystals in the samples by increasing temperature. The Raman scattered intensity increases and the FWHM of the CuO peaks decreases. Above 750 $^{o}$C Raman modes adscribed to $BaF_2$ and $Y_2Cu_2O_5$ are detected.

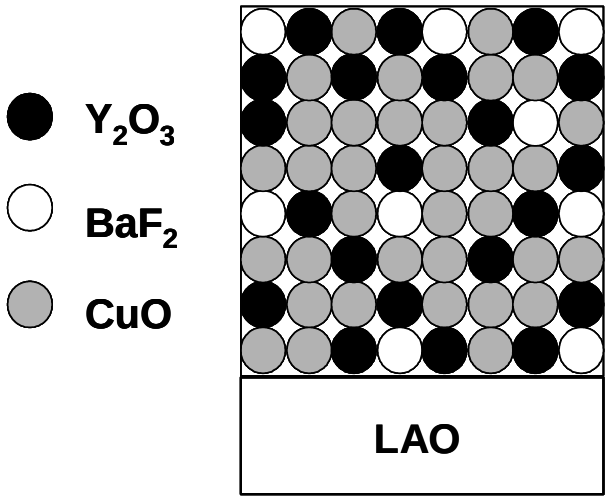


Figure 6.5. A possible explanation of the CuO nanocrystals coarsening when the temperature is increased. Notice that there is more density of CuO particles than $Y_2O_3$ and $BaF_2$ particles together.

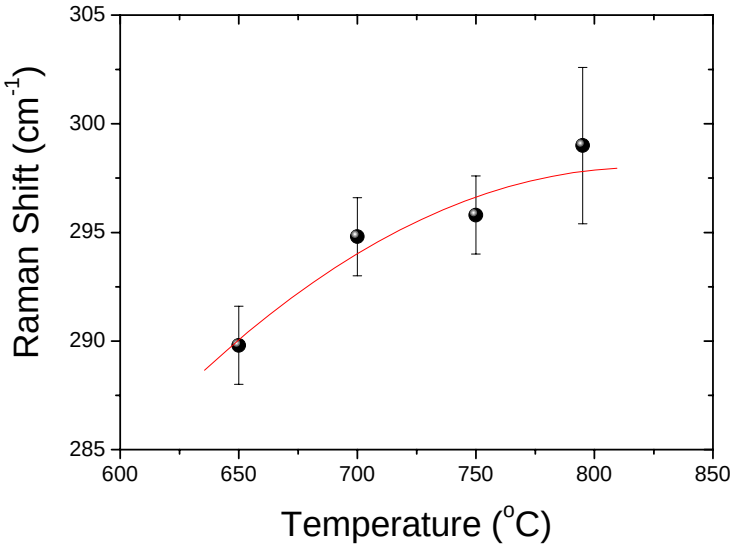


Figure 6.6. Measured dependence of the CuO $A_g$ phonon mode frequency with increasing of quench temperature. Notice the clear red shift of this CuO-$A_g$ phonon mode to ~ 300 cm$^{-1}$ when the temperature was increased.

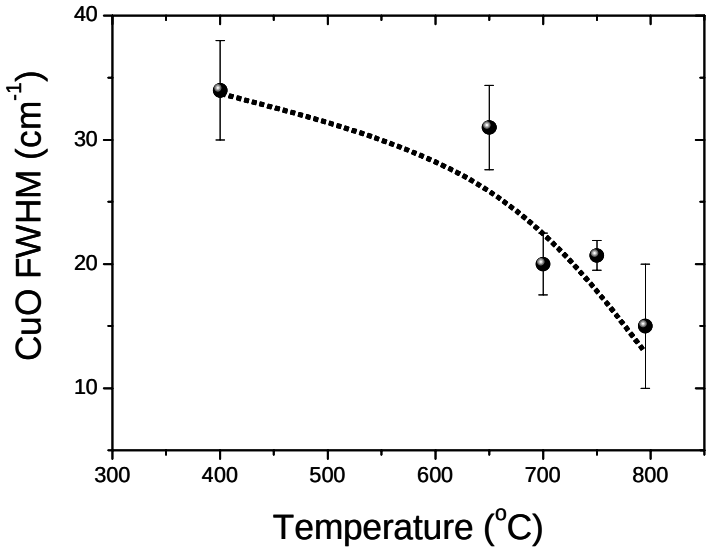


Figure 6.7. Measured dependence of the FWHM of the CuO Raman peak at 300 $cm^{-1}$ as a function of the quench temperature.

We have observed the coarsening and crystallization of the CuO phase at intermediate temperatures of the heat treatment. The precursor film consists of CuO, $Cu_2O$, $BaF_2$, $Ba_{1-x}Y_xF_2$ and $Y_2O_3$ from TEM and XRD analysis after pyrolysis. In the next section we will study the role of the intermediate phases on the YBCO nucleation at 795 $^oC$.

## 6.2. Quenched films at intermediate growth state

In this section, we shall focus on the study of the role of YBCO intermediate phases in the growth of $YBa_2Cu_3O_{6.5}$ when the sample is quenched at 795 $^oC$. We present the novel observations in two samples, called *samba098* and *samba090* with their main features described in tables 6.2 and 6.3, respectively. The main difference between them is the heating ramp and the gas flow rate. These samples were prepared in standard conditions ($P(H_2O)$ = 7 mbar, $P(O_2)$ = 0.2 mbar) to obtain films of high-$J_c$ and they were subsequently quenched at 795 $^oC$ by quickly pulling them out from the furnace to room temperature. The quenched profile used is shown in figure 6.8.

The XRD pattern of *samba098* displays the (*00l*) $YBa_2Cu_3O_{6.5}$ profiles denoting *c*-axis oriented grains with respect to LAO substrate is shown in figure 6.9. The presence of $YBa_2Cu_3O_{6.5}$ tetragonal phase indicates that the quenching conditions did not allow oxygen uptake required for the transformation of the non superconducting tetragonal phase to the superconducting orthorhombic phase. On the other hand, we also identify the coexistence of intermediate phases profiles such as $BaF_2$, $Y_2O_3$ and CuO. The $BaF_2$ profiles observed in the XRD pattern denote the presence of several crystalline *out-of-plane* orientations: (*h00*) and (*hkl*). In addition, the $Y_2O_3$ phase also shows the (*h00*) and (*hkl*) orientations and finally for the CuO phase the (*h0l*) orientation is detected.

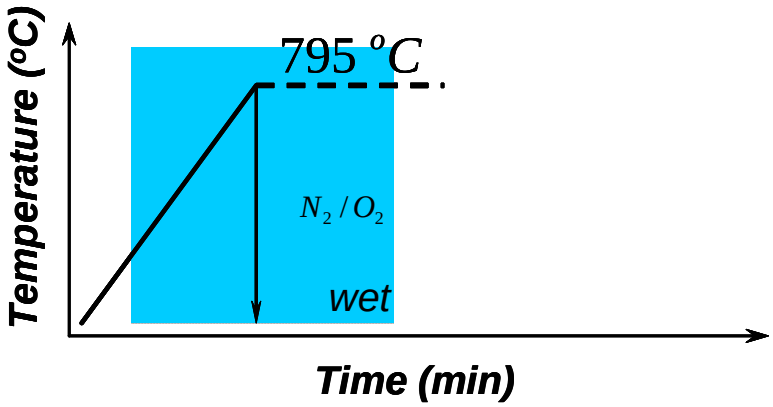


Figure 6.8. Quench profile of a sample quenched at 795 °C. Humidified gas introduced at 110 °C. The samples were quickly pulled out from the furnace to room temperature.

**Table 6.2**

Conditions of quenched film *samba098*

| |
|---|
| Precursor solution prepared from YBCO powder |
| Concentration = 1.5 M |
| LAO substrate |
| Optimized pyrolysis process |
| Heating ramp = 1500 °C/h |
| $P(H_2O)$ = 7 mbar |
| $P(O_2)$ = 0.2 mbar |
| Gas flow rate= 0.024 m/s |
| Quench temperature = 795 °C |

**Table 6.3**

Features of quenched film *samba090*

| |
|---|
| Precursor solution prepared from YBCO powder |
| Concentration = 1.5 M |
| LAO Substrate |
| Optimized pyrolysis process |
| Heating ramp = 500 $^{o}$C/h |
| P($H_2O$) = 7 mbar |
| P($O_2$) = 0.2 mbar |
| Gas flow rate = 0.0024 m/s |
| Quench temperature = 795 $^{o}$C |

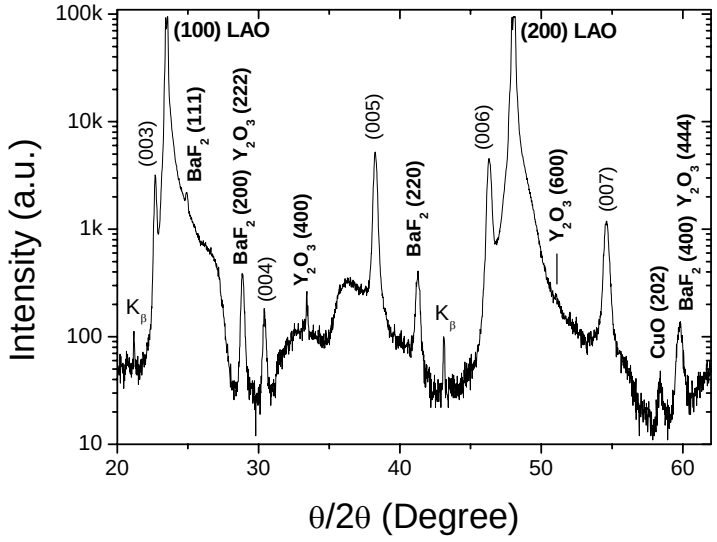


Figure 6.9. XRD pattern in logarithmic scale of a YBCO film *samba098* quenched at 795 $^{o}$C. Notice the presence of *c*-axis oriented grains and the coexistence of secondary phases such as $BaF_2$, $Y_2O_3$ and CuO.

We have performed the micro-Raman analysis of this quenched film. The representative micro-Raman spectrum of *samba098* sample is shown in figure 6.10, where we can observe the coexistence of $Y_2Cu_2O_5$, CuO and $BaF_2$ intermediate phases. As we saw in section 4.3, the $Y_2Cu_2O_5$ phase is Raman active and its phonon modes are clearly seen in the Raman spectra. However, the $Y_2Cu_2O_5$ phase has not been detected by XRD as a crystalline phase (figure 6.9) though micro-Raman could detect it. This fact could probably indicate that it forms nanocrystallites segregated at the surface. On the contrary, we will expect $Y_2O_3$ Raman signal, because this phase has a larger scattering efficiency than the other YBCO intermediate phases, as we saw in chapter 4. However this was not the case and we shall discuss it later. Although, the presence of small intensity signal of the LAO phonon at ~ 489 $cm^{-1}$ is an indication that the laser radiation arrived to the interface, we were not able to obtain any tetragonal $YBa_2Cu_3O_{6.5}$ Raman signal contrary to the XRD observation, probably because YBCO is only nucleated at the substrate interface. In addition, we remind that the scattering efficiency of impurities or secondary phases (and LAO) is larger than for $YBa_2Cu_3O_{6.5}$.

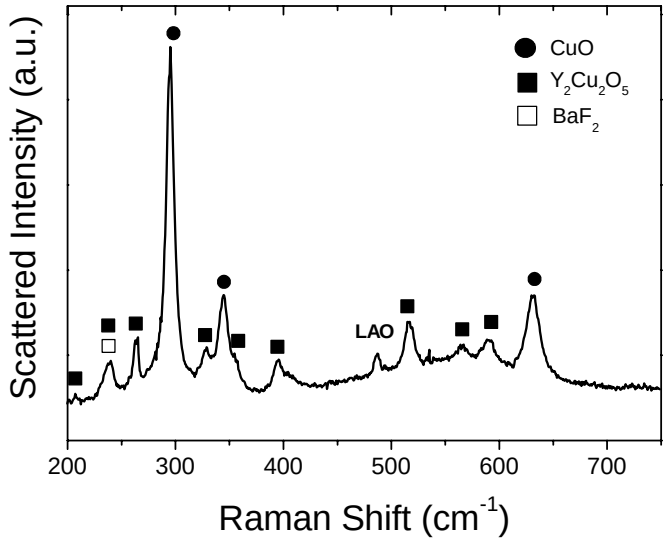


Figure 6.10. Raman spectrum of the sample *samba098* quenched at 795 $^oC$, laser spot ~ 1μm. Notice the coexistence of $Y_2Cu_2O_5$ (Y225), CuO and $BaF_2$ phases.

From a careful Raman analysis of this sample, we also observed that the CuO phase may have some degree of texture evidenced by an angular dependence of the phonon modes. By rotating the sample 45 degree one observes a change of the scattered

intensity of CuO phonon at 300 $cm^{-1}$, as shown in figure 6.11. The Y225 phase, did not presents any texture because it did not shows any meaningful intensity variation, as also seen in figure 6.11.

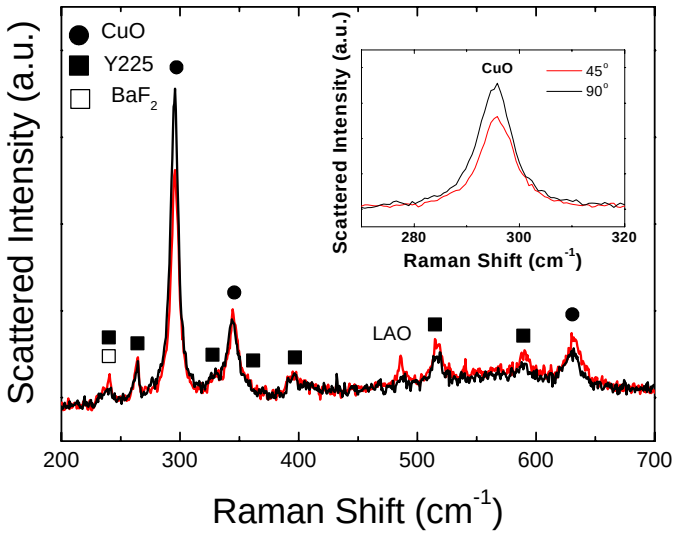


Figure 6.11. Raman spectrum of the sample *samba098* quenched at 795 $^{o}$C showing the variation of intensity of the CuO phonon mode when the sample is rotated 45 degree. The inset shows the scattered intensity variation of CuO phonon mode at 300 $cm^{-1}$ in the inset.

Figure 6.12 displays the morphology along the [*100*] direction of LAO substrate of the *samba098* quenched at 795 $^{o}$C observed by TEM. We may clearly observe a signature of the $YBa_2Cu_3O_{6.5}$ nucleation. The $YBa_2Cu_3O_{6.5}$ grains are indeed nucleated at the interface with similar growth rates and isolated grains inhomogeneously distributed are clearly observed. In addition, we do not observe nucleation of $YBa_2Cu_3O_{6.5}$ in other parts of the film. This fact evidences that YBCO TFA-MOD grows in an island-like growth and laminar growth mode contrasting with the columnar like growth mode of the physical deposition techniques[6.7]. Moreover, the presence of an *a*-axis oriented grain grown up to the film surface of length ~ 0.5 μm and of *c*-axis oriented grains grown up onto the LAO substrate surface of thickness between ~ 50-100 nm, corroborate that growth of YBCO is much faster (about 5 times) in the [*100*] direction than in the [*001*] direction.

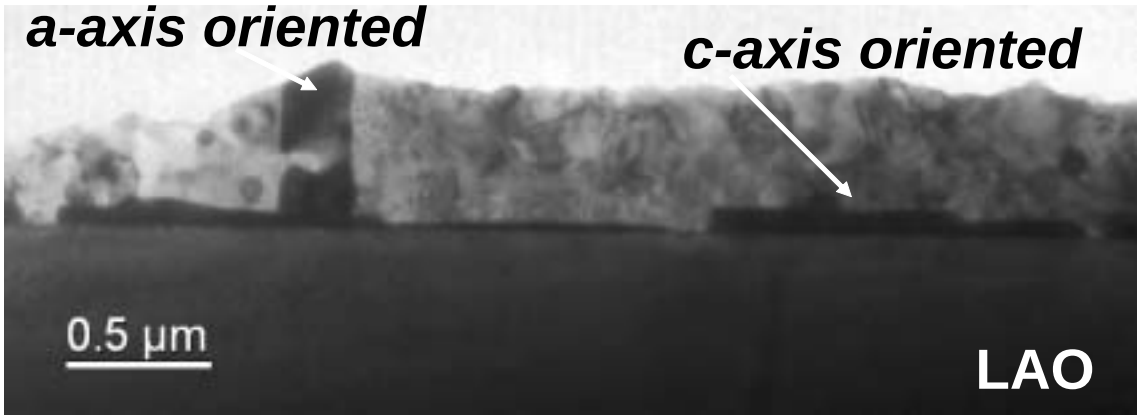


Figure 6.12. Low magnification cross sectional TEM micrograph of the quenched film *samba098* quenched from 795 $^{o}$C to room temperature, taken along the [*100*] direction of LAO. The white arrows point an *a*-axis oriented grain grown up to film surface and a *c*-axis oriented grains grown on to the interface.

On the other hand, higher magnification of the cross sectional TEM micrographs of *samba098* evidences very strong phase segregation in the precursor film, as shown in figure 6.13. The film consists of a nanocrystalline matrix with a diffusive boundary between the nanocrystallites. We have observed a mixture of segregate phases such as Ba-O-F, Ba-Y-O-F, Ba-Y-(Cu)-F-O and Y-Cu-O as determined from electron diffraction pattern (EDP) and electron energy loss spectroscopy (EELS) analysis[6.3] performed onto selected areas (the compound in parentheses means poor content of this element on the selected area analyzed by EELS). Therefore, the coexistence of segregated phases such as Ba-O-F, Ba-Y-O-F, Ba-Y-(Cu)-F-O and Y-Cu-O, gives evidence on the fact that the YBCO formation must involve long length atomic diffusion at least of hundreds micrometric distances through these intermediate crystalline phases. Y-Cu-O polyhedral crystal were found very near to the film surface (after EDP and EELS analysis), as shown in figure 6.13a, this fact is strongly correlated with micro-Raman results on this film (figure 6.10) due to the clear presence of the $Y_2Cu_2O_5$ phonon modes in the Raman spectra. Our TEM results only partially agree with those of Yoshizumi *et al*[4.18], since they suggest that the $Y_2Cu_2O_5$ phase is not present as a discrete crystalline phase but may form an amorphous alloy. In addition, the Y-Ba-O-F compound claimed by Araki *et al*[1.26] and Wu *et al*[6.14] was also found in our EDP and EELS analysis. However we did not find any evidence of a liquid phase surrounding the YBCO growing interface as claimed by McIntyre *et al*[4.9] and

Solovyov *et al*[6.8], but we found the nanocrystalline phases of $BaF_2$ (or $Ba_{1-x}Y_xF_2$), BaO and $Y_2O_3$ very close to the YBCO growth front and/or near to the substrate interface, as it can be observed in the high resolution TEM micrographs 6.13b-d. We also observed that BaO nanocrystals are embebed in a matrix of $BaF_2$ which are in contact with the substrate surface (figure 6.13c). Other phases, such as $BaCuO_2$, reported by other authors[4.9,6.1] in YBCO films prepared by TFA-MOD process were not observed in our samples[6.3].

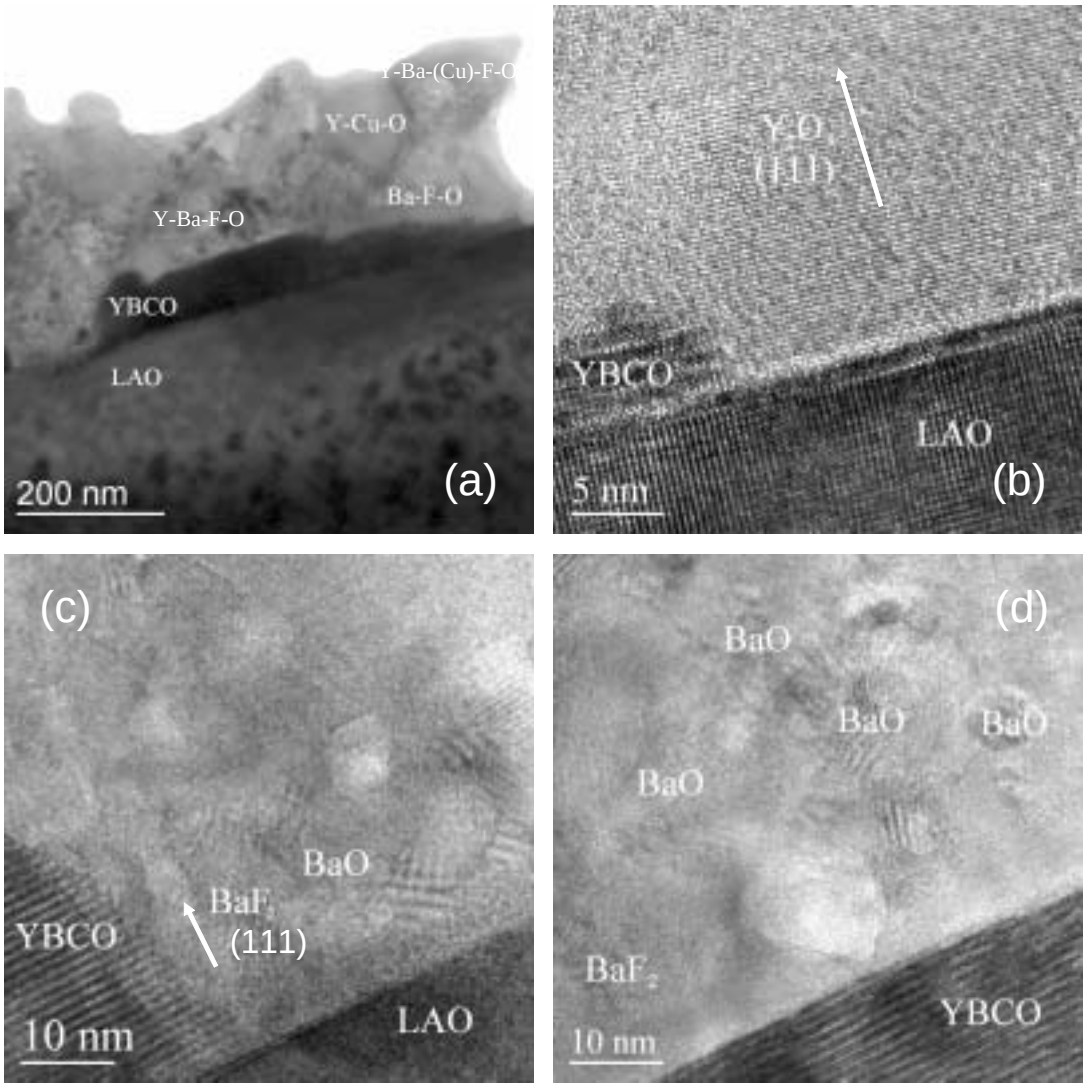


Figure 6.13. (a) Low magnification cross sectional TEM micrograph along the [*100*] direction of LAO. Notice the coexistence of Y-Cu-O, Ba-O-F, Y-Ba-O-F, Y-Ba-(Cu)-O-F and *c*-axis oriented $YBa_2Cu_3O_{6.5}$ phases, while (b), (c) and (d) show high resolution TEM micrographs where we observed the presence of $Y_2O_3$, $BaF_2$ and BaO phases near to the YBCO growth front and to the LAO substrate surface.

In addition, from a detailed analysis of the quenched film by EDP and EELS in some regions of the interface, we have observed that parts of the substrate were covered with some inclusions of the $Y_2O_3$ epitaxial crystals aligned with (*111*) $Y_2O_3$ // (*001*) LAO, as shown in figure 6.13b. In addition, other important information about this phase is that [*-12-1*] $Y_2O_3$ // [*100*] LAO. These $Y_2O_3$ epitaxial crystals are detected at the interface in contact with YBCO and LAO substrate, and may be acting as precursor phase but they also could be kept as precipitates. However at the YBCO growth interface regions, we mainly found the $BaF_2$ phase aligned with (*111*) $BaF_2$ // (*001*) LAO. Moreover, other important information about this phase is that [*011*] $BaF_2$ // [*100*] LAO. These (*111*) planes seem to act as a nucleus for the YBCO formation, as shown in figure 6.13c. Since interplanar distance of (*111*) of $BaF_2$ phase ~ 3.58 Å, is similar to 1/3(*001*) of $YBa_2Cu_3O_{6.5}$ (~3.95 Å), it is possible that this is the initial stage of the nucleation of $YBa_2Cu_3O_{6.5}$, as schematically shown in figure 6.13b.

On the contrary, the $BaF_2$ phase is clearly observed in XRD with large peaks but it has a poor Raman signal overlapped with the $Y_2Cu_2O_5$ phase at ~ 238 $cm^{-1}$, this fact may be due to the following causes:

(a) high rates of heating ramp accelerate the decomposition of the $BaF_2$ phase into some kind of metastable phase of Ba oxy-fluoride, not Raman active, in contact with water vapour.

(b) this oxyfluoride phase (Y-Ba-O-F) may be a solid solution with Y as shown by XRD and TEM studies and in any case neither Raman active. This is in agreement with Wu *et al*[6.2], who suggest the existence of oxy-fluorides of Y and Ba, with composition $[Ba_{0.7}Y_{0.3}][F_{0.85}O_{0.15}]_2$, and with a crystal structure and lattice parameters very similar to the $BaF_2$ phase. This possible Y-Ba-O-F phase has a more compact unit cell because yttrium ions partially substitute for large barium ions. This substitution is compensated by the substitution of fluorine ions by oxygen ions and the resulting lattice parameter is ~ 5.9 Å[6.9].

(c) The presence of nanometric $BaF_2$ not yet decomposed by the humidified gas could be disseminated near to the YBCO growth front or segregate close to the interface, as it was determined by TEM observations.

(d) The possible existence of the Ba(OH)F compound as a YBCO intermediate phase after $BaF_2$ decomposition, as suggested by Venkataraman *et al*[6.1] also not Raman active in our work range [200 – 700 $cm^{-1}$].

On the other hand, concerning to the absence of $Y_2O_3$ phonon modes in the micro-Raman spectra, we suggest that this fact can be due to:
(a) Large transformation of yttrium TFA into $Y_2Cu_2O_5$ rather than into $Y_2O_3$ phase in the reaction process.
(b) $Y_2O_3$ phase is transformed to Y oxy-fluoride compound (Y-O-F) as claimed by Shibata *et al*[6.10] after thermal decomposition in a humidified atmosphere and then this fact changes its Raman tensor and frequency, and this Y oxyfluoride compound is not Raman active in our work range [200 – 700 $cm^{-1}$].
(c) As in the case of $BaF_2$ phase, $Y_2O_3$ is very disseminate and localized very near to interface of YBCO growth front, as it was in fact observed in TEM micrographs discussed before.

Now, we look at the second quenched sample studied, called *samba090*, where we lowered the heating ramp rate to 500 $^oC/h$ and decreased the gas flow rate to 0.0024 m/s with respect to the quenched sample just analyzed and we kept all remaining parameters constant. In these growth conditions, low heating ramp and low gas flow rate, we expect the $BaF_2$ decomposition rate to be slower; because decomposition rate is temperature and humidified gas dependent[4.11] and then few YBCO nucleuses will be at the substrate interface. Thus, we shall expect to observe more clearly the role of YBCO intermediate phases, when the heating ramp reaches 795 $^oC$ in approximately ~ 90 minutes, than in ~ 30 min (*samba098*). The main processing features of this sample are shown in table 6.3. The quenched profile used is the same as *samba098* (figure 6.8).

We performed the XRD of this quenched samples, as shown in figure 6.14. The XRD pattern of *samba090* displays low intensity (*00l*) $YBa_2Cu_3O_{6.5}$ profiles, due to YBCO growth conditions (table 6.3). We can also observe the coexistence of intermediate phases profiles such as $BaF_2$, $Y_2O_3$ and CuO. Moreover, since the standard XRD $\theta/2\theta$-scan performed has low scattered signal and low statistics of intermediate phases, we performed a XRD $\theta/2\theta$-scan of 12 hours of accumulation time with a step of $\Delta 2\theta \sim 0.02$

degree, as displayed in figure 6.15. Thus, we have been able to observe more clearly the intermediate phases of CuO, $Y_2O_3$, $BaF_2$ and $Ba_{1-x}Y_xF_2$ and now even $Y_2Cu_2O_5$. We can appreciate clearly the XRD profiles of the $Y_2Cu_2O_5$ phase, and it has just the (*hkl*) orientation. Moreover, the $BaF_2$ phase has two orientations (*h00*) and (*hkl*), for the $Ba_{1-x}Y_xF_2$ phase (*hkl*) orientation, for the CuO phase (*hkl*) orientation, finally $Y_2O_3$ phase has only a (*h00*) orientation. In addition, concerning to $Y_2O_3$ (*hkl*) orientation, we have tentatively assigned to the peak at 2θ ~ 29 degree the (*200*) $BaF_2$ and (*222*) $Y_2O_3$ profiles since they are very close: $2\theta_{BaF_2}^{(200)} \approx 28.77^{o}$ and $2\theta_{Y_2O_3}^{(222)} \approx 29.15^{o}$. The majority of orientations observed in XRD are correlated with the TEM results of *samba098*. The curved background observed in the XRD pattern, between approximately $24^{o}$ – $30^{o}$ degree, is due to the presence of (*100*) LAO profile tail at ~ 23 degree.

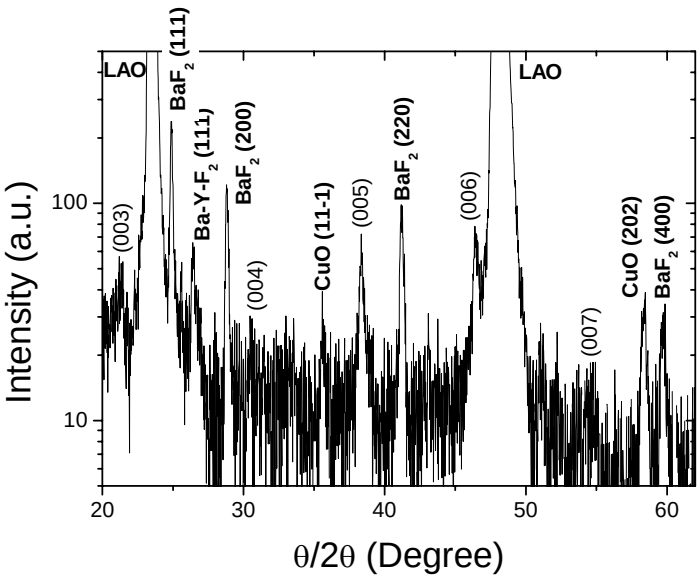


Figure 6.14. Logarithmic XRD pattern of YBCO film quenched at 795 $^{o}$C with low heating ramp and low gas flow rate (*samba090*). Notice the coexistence of the intermediate phase's profiles such as $BaF_2$, $Ba_{1-x}Y_xF_2$ (Ba-Y-$F_2$) and CuO.

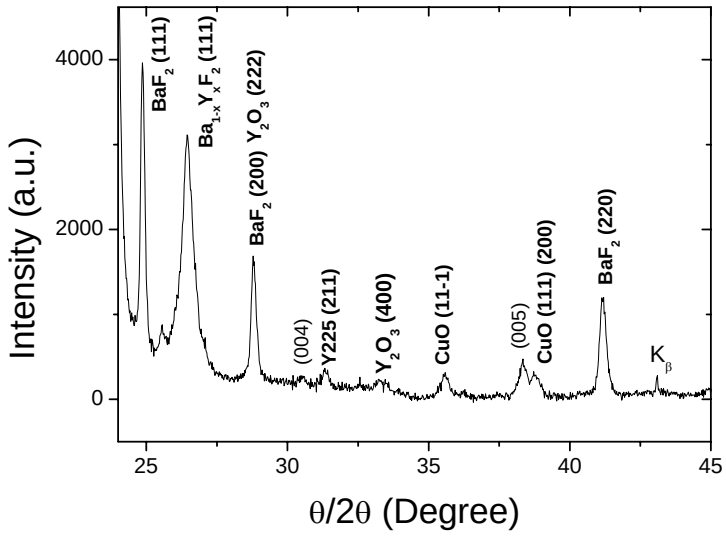


Figure 6.15. XRD pattern taken with 12 hours of accumulation time of a YBCO film quenched at 795 $^{o}$C with low heating ramp and low gas flow rate. Notice the coexistence of segregate phases such as $BaF_2$, $Ba_{1-x}Y_xF_2$, $Y_2Cu_2O_5$ (Y225), $Y_2O_3$, CuO.

We have been able to obtain the grain size[‡] of these intermediate and precursor phases by using the *Debye-Scherrer* equation[6.11,6.12] and its corresponding ASTM files (table 6.4). Therefore, from the $BaF_2$ reflections (*111*), (*200*) and (*220*) a grain size of approximately ~ 385 nm is obtained, while from the (*400*) $Y_2O_3$ profile we obtain ~ 20 nm, from the (*211*) $Y_2Cu_2O_5$ profile ~ 45 nm, finally from (11-1) and (*111*) CuO profiles ~ 25 nm grain size.

**Table 6.4**

Possible observed phases in the YBCO growth by TFA-MOD process.

[‡] For grain size calculation of the YBCO intermediate phases, we used the *Deybe-Scherrer* equation and worked with corrected broadening of the profile, $\beta$, *i.e.* $\beta = \sqrt{\beta_{\exp}^2 - \beta_{Si}^2}$, where $\beta_{\exp}$ is the FWHM of the corresponding profile and $\beta_{Si}$ is the FWHM of the $SiO_2$ single crystal.

$$Grain\ Size = \frac{0.9\lambda}{\beta \cos\theta}$$

| Phase | Structure (S.G.) | Cell parameters (Å) | Reference ASTM |
|---|---|---|---|
| $Y_2O_3$ | Cubic (Ia3) | *a* = 10.604 | 41-1105 |
| $YF_3$ | Orthorhombic | *a* = 6.3654 | 32-1431 |
| | (Pnma) | *b* = 6.8566 | |
| | | *c* = 4.3916 | |
| $BaF_2$ | Cubic (Fm3m) | *a* = 6.2001 | 04-0452 |
| BaO | Cubic (Fm3m) | *a* = 5.355 | 30-142 |
| CuO | Monoclinic | *a* = 4.685 | 41-254 |
| | (C2/c) | *b* = 3.423 | |
| | | *c* = 5.132 | |
| $CuF_3$ | Monoclinic | *a* = 3.2973 | 42-1244 |
| | ($P2^1/n$) | *b* = 4.5624 | |
| | | *c* = 4.6157 | |
| $Cu_2O$ | Cubic (Pn3m) | *a* = 4.269 | 05-667 |
| $BaCuO_2$ | Cubic (Im3m) | *a* = 18.285 | 38-1402 |
| $Y_2Cu_2O_5$ | Orthorhombic | *a* = 10.799 | 33-511 |
| | ($Pna2_1$) | *b* = 3.496 | |
| | | *c* = 12.456 | |
| $YBa_2Cu_3O_7$ | Orthorhombic | *a* = 3.886 | 38-1433 |
| | (Pmmm) | *b* = 3.818 | |
| | | *c* = 11.680 | |
| $YBa_2Cu_3O_6$ | Tetragonal | *a* = 3.857 | 39-1496 |
| | (P4/mmm) | *c* = 11.839 | |

Then, we performed micro-Raman analysis of this film *samba090*. The micro-Raman spectrum is displayed in figure 6.16. We observe the coexistence of three intermediate phases such as $Y_2Cu_2O_5$, $BaF_2$ and CuO phases as in the case of *samba098*. The micro-Raman spectrum obtained was very similar to *samba098* (figures 6.10 and 6.16), we have not found any noticeable difference between both spectra.

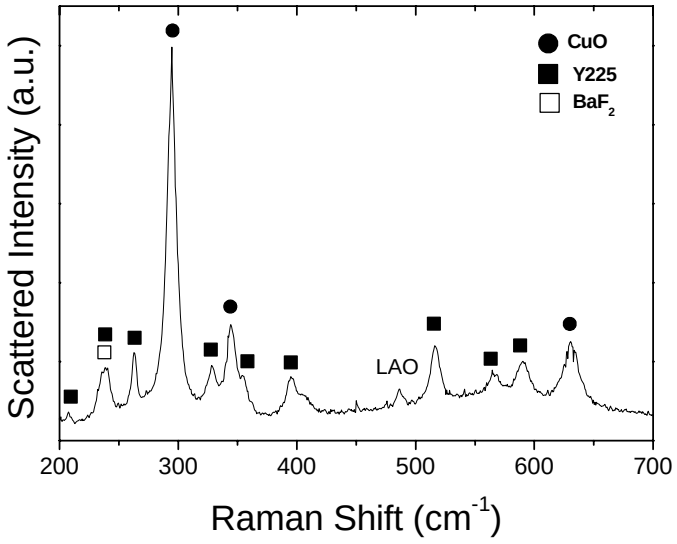


Figure 6.16. Raman spectrum of sample quenched at 795 $^{o}$C at low heating ramp and low gas flow rate (*samba090*). Notice the coexistence $BaF_2$, $Y_2Cu_2O_5$ and CuO phases

The presence of the LAO phonon Raman signal at ~ 489 $cm^{-1}$, is a signature that the laser light reached the LAO substrate surface, but we have not obtained any Raman signal of $YBa_2Cu_3O_{6.5}$ or $Y_2O_3$ phases in the same manner as in *samba098* sample. Moreover, we expected to obtain a Raman signal of $Y_2O_3$ phase in this growth conditions (low $BaF_2$ decomposition rate), because this phase has a larger scattering efficiency than the other YBCO intermediate phases (section 4.3). Therefore we suspect that also $Y_2O_3$ phase is transformed to an oxy-fluoride of Y compound (Y-O-F) as claimed by Shibata *et al*[6.10] after thermal decomposition in a humidified atmosphere. On the contrary, Venkataraman *et al*[6.1] proposed that in the chemical overall reaction:

| | |
|---|---|
| $0.5Y_2O_3 + 2BaF_2 + CuO + 2H_2O \xrightarrow{O_2} YBa_2Cu_3O_{7-\delta} + 4HF(g)$, | (6.1) |

the $Y_2O_3$ phase reacted with CuO nanocrystals to form the $Y_2Cu_2O_5$ phase, as stated in equation (6.2):

| | |
|---|---|
| $0.5Y_2O_3 + 2BaF_2 + CuO + 2H_2O \xrightarrow{O_2} Y_2Cu_2O_5 + BaF_2 + H_2O \xrightarrow{O_2} \xrightarrow{O_2} YBa_2Cu_3O_{7-\delta} + 4HF(g)$ | (6.2) |

In addition, Wu *et al*[6.14] suggested, on the basis of their TEM analysis, that the fraction of $Y_2O_3$ phase on the quenched films was very small. In any case, the fact of changing atoms (fluor by oxygen) in the $Y_2O_3$ structure, changes its Raman tensor and frequency and this new compound is not Raman active in our work range [200 – 700 $cm^{-1}$].

It is clear that the transformation of the intermediate phases into $YBa_2Cu_3O_{6.5}$ is a very complex issue. We have observed that the period of time at high temperature is very important parameter, as we saw in chapter 5; moreover the conversion time of the intermediate phases into $YBa_2Cu_3O_{6.5}$ is very short. To evidence this fact, we performed micro-Raman analysis on three samples kept at 795 $^oC$ for 0, 15 and 30 minutes, respectively. Figure 6.17a shows the presence of only precursor phases in the Raman spectrum of *samba090*. Instead, in figure 6.17b-c we present two particular samples grown in the same processing conditions than *samba090* sample and kept at 795 $^oC$ for just 15 and 30 minutes respectively. We have observed that with 15 minutes at 795 $^oC$ the full precursor layer is converted into $YBa_2Cu_3O_{6.5}$ though still some disorder is present, due to presence of the disorder induced Raman modes O(1) and Cu(1) (figure 6.17b), meanwhile with 30 minutes at 795 $^oC$ the Raman spectra gives a pure YBCO signal, where we only observe YBCO Raman phonon modes (figure 6.17c).

On the basis of all the above results, we propose that the reaction mechanism of the YBCO intermediate phases is not seen to be simple, several phase combinations may be plausible and several simultaneous reactions may likely occur to convert the precursor phases into $YBa_2Cu_3O_{6.5}$, as shown schematically in figure 6.18.

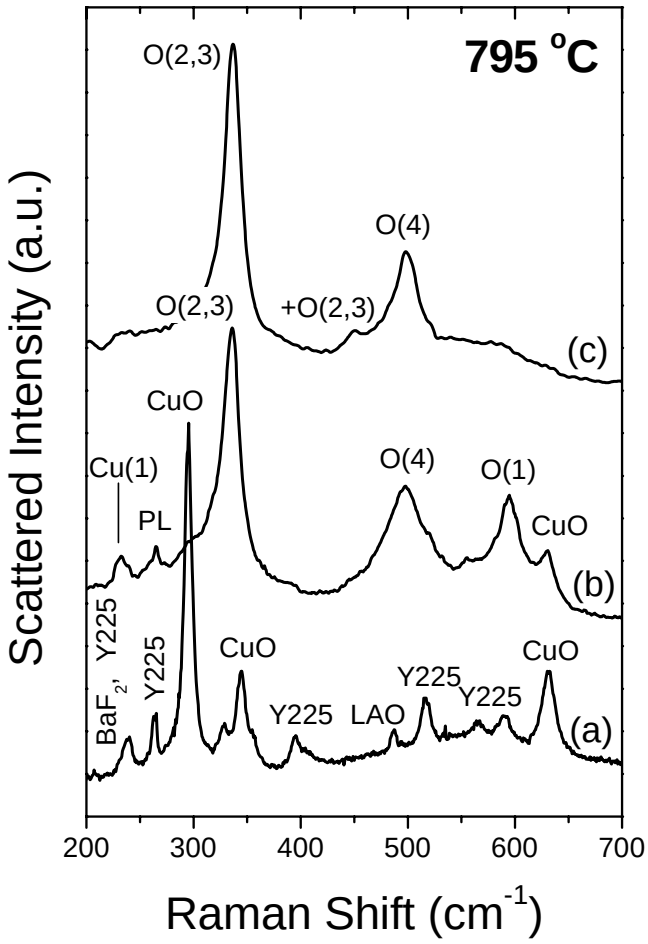


Figure 6.17. Raman spectra of sample (a) quenched at 795 $^{o}$C (figure 6.16), maintained during (b) 15 minutes at 795 $^{o}$C and (c) 30 minutes at 795 $^{o}$C after oxygenation step.

Finally, we evidenced on the basis of XRD, micro-Raman and TEM analysis of quenched samples at 795 $^{o}$C, that strong phase segregation exists denoting the complex behaviour of the precursor film and the complex chemical reaction involved in YBCO epitaxial conversion growth at this stage of the heat treatment. The behaviour of the YBCO intermediate phases as not fully clarified in the quenched films studied at low temperatures. Thus, we did a quenched sample applying long time heat treatment to give the opportunity to these YBCO intermediate phases to coarsen in non YBCO growth conditions and thus be able to better to analyze their behaviour. We selected the intermediate temperature of 700 $^{o}$C, because it is claimed that nucleation of $YBa_2Cu_3O_{6.5}$ requires a temperature that exceeds 700 $^{o}$C[4.18].

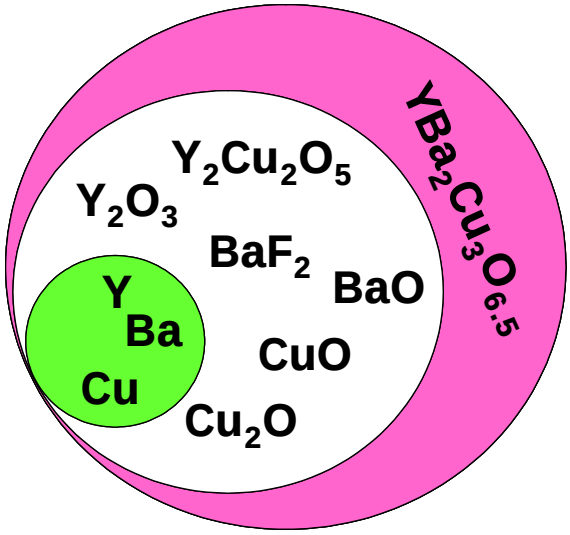


Figure 6.18. Several simultaneous reactions may likely occur to convert the precursor phases to YBCO films. Notice that $BaF_2$ may also indicate Ba-F-O and Ba-Y-F-O.

## 6.3. Growth at 700 $^{o}$C after long time heat treatment

We have chosen the intermediate temperature of 700 $^{o}$C to better analyze the YBCO intermediate phases after long time heat treatment with the main features described in table 6.5. The sample was hold at 700 $^{o}$C for about 1100 minutes (~18 hours), at P($H_2O$) ≈ 0.1 mbar and gas flow rate = 0.0024 m/s. These values are non favourable YBCO growth conditions to give opportunity to the YBCO intermediate phases coarsening, besides the CuO previously observed (section 6.1). Then, the film was quickly pulled out from the furnace to room temperature. We came back to high heating rates of 1500 $^{o}$C/h, to quickly arrive to 700 $^{o}$C in approximately ~ 27 minutes. The thermal profile used is shown in figure 6.19.

**Table 6.5**

Features of the film *samba097* maintained 18 hours at 700 $^{o}$C

| |
|---|
| Precursor solution prepared from YBCO powder |
| Concentration = 1.5 M |
| LAO Substrate |
| Optimized pyrolysis process |
| Heating ramp = 1500 $^{o}$C/h |
| $P(H_2O) \approx 0.1$ mbar |
| $P(O_2) = 0$ mbar |
| Gas flow rate = 0.0024 m/s |
| Reaction time = 1100 minutes |
| Growth temperature = 700 $^{o}$C |

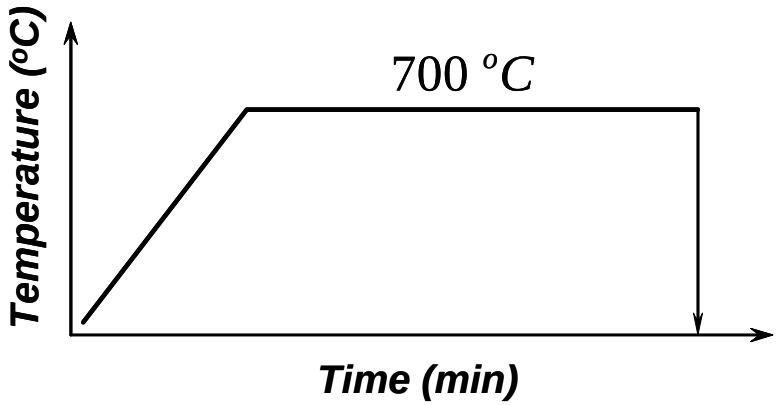


Figure 6.19. Thermal profile of a sample kept at 700 $^{o}$C for 1100 minutes (~18 hours). The sample was quickly pulled out from the oven to room temperature. Main features of this sample are shown in table 6.5.

Figure 6.20 shows the XRD pattern of *samba097* sample which clearly displays (*00l*) $YBa_2Cu_3O_{6.5}$ profiles denoting *c*-axis oriented grains growth perpendicular to the LAO substrate surface. We can also observe the crystallization of the intermediate phases such as $BaF_2$ and $Y_2O_3$. The $BaF_2$ profiles observed in the XRD pattern also denoting the presence of two crystalline *out-of-plane* orientations: (*h00*) and (*hkl*), the same situation is found for the $Y_2O_3$ profiles. On the other hand, we have tentatively assigned to the peak at $2\theta \sim 29$ degree as composed of the (*200*) $BaF_2$ and (*222*) $Y_2O_3$ profiles

due to the fact that they are very close: $2\theta_{BaF_2}^{(200)} \approx 28.77^o$ and $2\theta_{Y_2O_3}^{(222)} \approx 29.15^o$. The same situation was observed for the peak at 2θ ~ 59.9 degree where the (*400*) $BaF_2$ and (*444*) $Y_2O_3$ profiles are overlapped because they are very close too: $2\theta_{BaF_2}^{(400)} \approx 59.60^o$ and $2\theta_{Y_2O_3}^{(444)} \approx 60.44^o$. Moreover, despite of the non YBCO growth conditions, the appearance of the $YBa_2Cu_3O_{6.5}$ phase among the intermediate phases is ascribed to the presence of the ambient water vapour pressure inside the furnace ($P(H_2O) \approx 0.1$ mbar) even when non additional pressure is injected. It is clear that this low water vapour pressure is enough to partially decompose $BaF_2$ after a long time heat treatment.

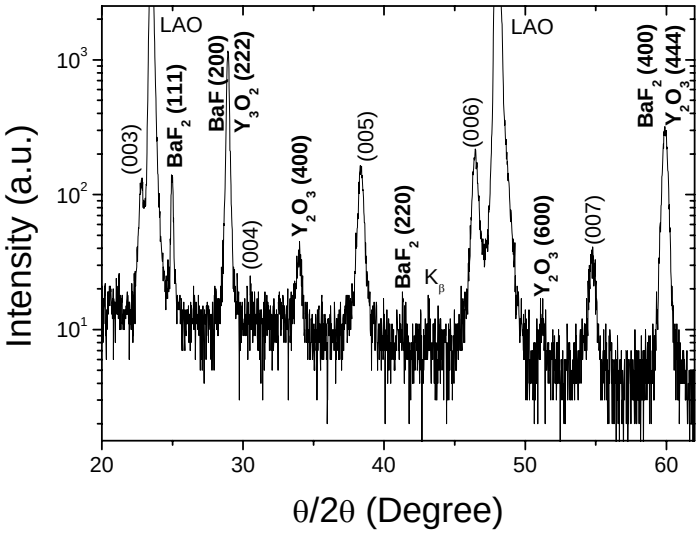


Figure 6.20. XRD pattern in logarithmic scale of YBCO film quenched at 700 $^oC$ with previous long time heat treatment. Notice the presence of small amounts of *c*-axis oriented grains, and coexistence of the intermediate phase's profiles such as $Y_2O_3$ and $BaF_2$.

Due to the fact that the standard XRD θ/2θ-scan performed has a noisy background, to clearly identify the YBCO intermediate phases, we performed again a XRD θ/2θ-scan of 12 hours of accumulation time with a step of Δ2θ ~ 0.02 degree, as displayed in figure 6.21. We can observe the coexistence of the $BaF_2$, $Ba_{1-x}Y_xF_2$ , $Y_2Cu_2O_5$, $Y_2O_3$ and CuO intermediate phases in the XRD pattern. The $Y_2Cu_2O_5$ phase has a random orientation; the same situation is seen for the CuO phase, (*hkl*) orientation too, meanwhile the $Y_2O_3$ phase has two orientations: (*h00*) and (*hkl*), whilst the $Ba_{1-x}Y_xF_2$

phase has just (*111*) orientation and finally the $BaF_2$ phase shows the (*h00*) and (*hkl*) orientations. The curved background observed, between $24^o$ – $30^o$, is due to the presence of (*100*) LAO profile tail at ~ 23 degree. We have also been able to obtain the grain size of these phases by using the *Deybe-Scherrer* equation[6.1,6.2] and its corresponding ASTM files (table 6.4), as it was performed in section 6.2. Therefore, from the (*111*) and (*220*) $BaF_2$ reflections the grain size approaches to ~ 225 nm, while from the (*400*) $Y_2O_3$ profile ~ 21 nm grain size is obtained.

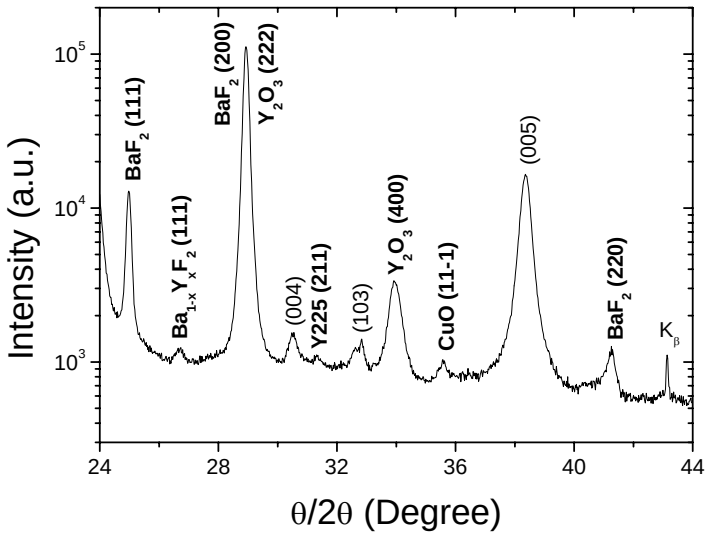


Figure 6.21. XRD pattern in logarithmic scale of YBCO film quenched at 700 $^oC$ with previous long time heat treatment. Notice the coexistence of segregated phases such as $BaF_2$, $Ba_{1-x}Y_xF_2$, $Y_2Cu_2O_5$, $Y_2O_3$ and CuO.

Next, we are interested in knowing if the $BaF_2$ phase is textured. We have chosen the (*200*) $BaF_2$ reflection to investigate the texture. To clarify this issue, we performed a pole figure of the (*111*) direction, as shown in figure 6.22. The pole figure displays an *in-plane* texture of this reflection, due to the presence of four sharp peaks arranged 90 degree of each other. Therefore, the (*111*) and (*200*) $BaF_2$ epitaxial texture is clearly observed due to lattice-matched substrate surface. Moreover, the $\Delta\phi$ value obtained $<1^o$ is characteristic of compounds grown onto single crystals. In addition, the interplanar distances between $BaF_2$ and LAO are in fact rather close: $d_{BaF_2}^{(111)} \approx 3.58$ Å, and $d_{LAO}^{(100)} \approx 3.7$ Å, respectively.

On the other hand, we are also interested in knowing if the $Y_2O_3$ phase is textured too. We have chosen the (*400*) $Y_2O_3$ reflection to investigate the texture. We performed XRD ϕ-scan of the [*404*] direction with $\psi \sim 45^o$ and $2\theta \sim 48^o$. Figure 6.23 shows the four sharp peaks with a 90 degree period of the (*404)* $Y_2O_3$ profile with $\Delta\phi \sim 1.10^o$, corroborating its *in-plane* texture due to lattice-matched substrate surface.

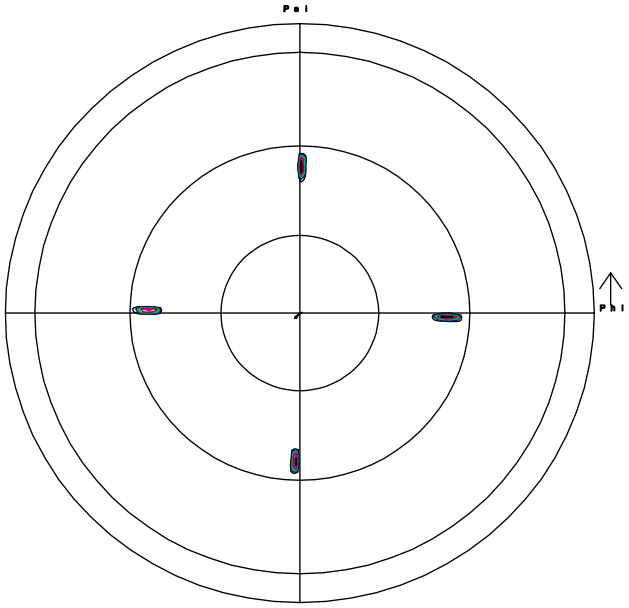

Figure 6.22. XRD pole figure of biaxially textured (*111*) profile of the $BaF_2$ phase.

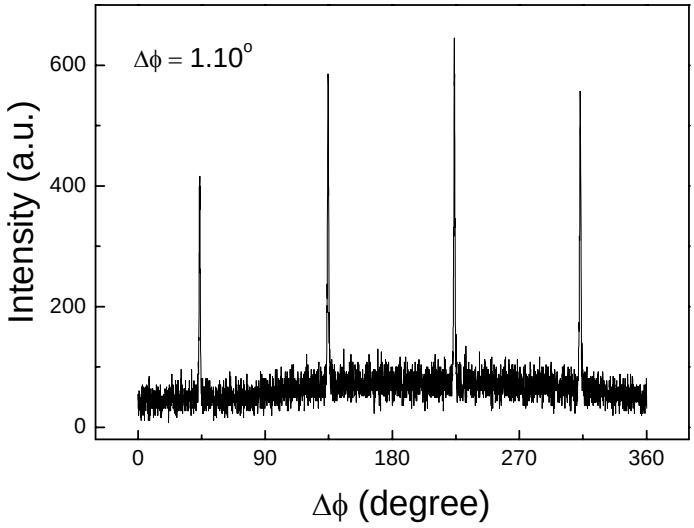


Figure 6.23. XRD ϕ-scan of (*404*) $Y_2O_3$ profile, denoting biaxial texture.

Then, we performed micro-Raman analysis of *samba097* sample. The representative micro-Raman spectrum is displayed in figure 6.24. We can observe the coexistence of three intermediate phases such as $Y_2Cu_2O_5$, $BaF_2$ and CuO phases. The appearance of these phases is correlated with the results on XRD (figure 6.21). But instead, the high peaks obtained in XRD for $BaF_2$ and $Y_2O_3$ phases neither were correlated with micro-Raman results. Additionally, we expected to obtain $Y_2O_3$ Raman signal, because this phase has a large scattering efficiency than the other YBCO intermediate phases (scattering efficiency of $Y_2O_3$ >> $BaF_2$ > $Y_2Cu_2O_5$ > CuO). Therefore, we suggest again that the $Y_2O_3$ phase is transformed to an oxy-fluoride of Y compound (Y-O-F), as it also might happen with the $BaF_2$ phase. Moreover, we have also obtained the $YBa_2Cu_3O_{6.5}$ Raman phonon modes, overlapped with CuO and $Y_2Cu_2O_5$ phonons at 340 and 486 $cm^{-1}$, respectively. We confirm the oxygen content of the YBCO phase by the O(4) position (section 4.4) at 486 $cm^{-1}$ corresponding to an oxygen content of ~ 6.5 (equation 4.12). As it was expressed above, the low water vapour pressure used is enough to produce $BaF_2$ decomposition and in addition, the growth temperature(700 $^oC$) is high enough too to produce YBCO nucleation.

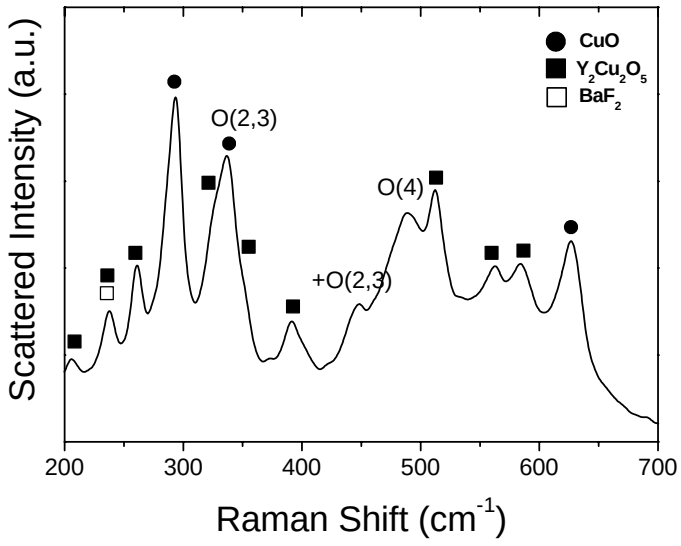


Figure 6.24. Raman spectra of quenched at 700 $^oC$ with previous long heat treatment. Notice the coexistence $BaF_2$, $Y_2Cu_2O_5$, CuO phases and $YBa_2Cu_3O_{6.5}$. The $YBa_2Cu_3O_{6.5}$ Raman phonons are overlapped with CuO and $Y_2Cu_2O_5$ phonons at 340 and 486 $cm^{-1}$, respectively.

From a careful angular Raman analysis performed on this sample, we also observed that the CuO phase may have some degree of texture evidenced by the angular dependence of the phonon mode. By rotating the sample 45 degree the scattered intensity of the CuO phonon at 300 $cm^{-1}$ change. The $Y_2Cu_2O_5$ phase did not present any Raman detectable texture. On the other hand, we suspect that the texture observed in XRD for $BaF_2$ phase is due to Ba oxy-fluoride (Ba-O-F) compound.

Figure 6.25 shows the TEM cross section of *samba097* along the direction of [*100*] LAO substrate. We can also observe $YBa_2Cu_3O_{6.5}$ nucleation at interface pointed by white arrows. The *c*-axis oriented grains of thickness approximately ~ 25 nm, are isolated and inhomogeneously distributed grains grown onto the LAO substrate surface. In a similar manner of *samba098* sample, cross sectional TEM micrographs of *samba097,* confirm the complex behaviour of precursor film after long time heat treatment. The film is composed of phases with well defined boundaries (by contrast). There exist an amorphous layer that consists of a $Cu_2O$ nanocrystalline amorphous matrix with embedded CuO nanocrystals randomly oriented, as determined by EDP and EELS[6.3]. In addition, on the top of the *c*-axis oriented grains of $YBa_2Cu_3O_{6.5}$ grown at the interface, there appear Ba-F-O, Y-Ba-O-F and Y-Ba-(Cu)-O-F compounds. We observed that YBCO islands nucleate inhomogeneously at the interface with similar growth rates.

The observable difference comparing to *samba098* sample is the YBCO concentration at the substrate interface (figure 6.12). A major concentration and large grain sizes of the YBCO intermediate phases are observed in *samba098* (figure 6.13a). Additionally, in this sample *samba097* we have observed the presence of the $Cu_2O$ and CuO phases for first time. On the other hand, one fact correlated with TEM results of *samba098* is the presence of the $BaF_2$ phase (Y-Ba-O-F) very close to $YBa_2Cu_3O_{6.5}$ growth front with its (*111*) planes parallel to the (*100*) planes of LAO substrate. This result gives further evidence on the fact that *c*-axis oriented grains of $YBa_2Cu_3O_{6.5}$ were nucleated from (*111*) $BaF_2$ orientation at the interface. Moreover, the $BaCuO_2$ phase was neither observed here.

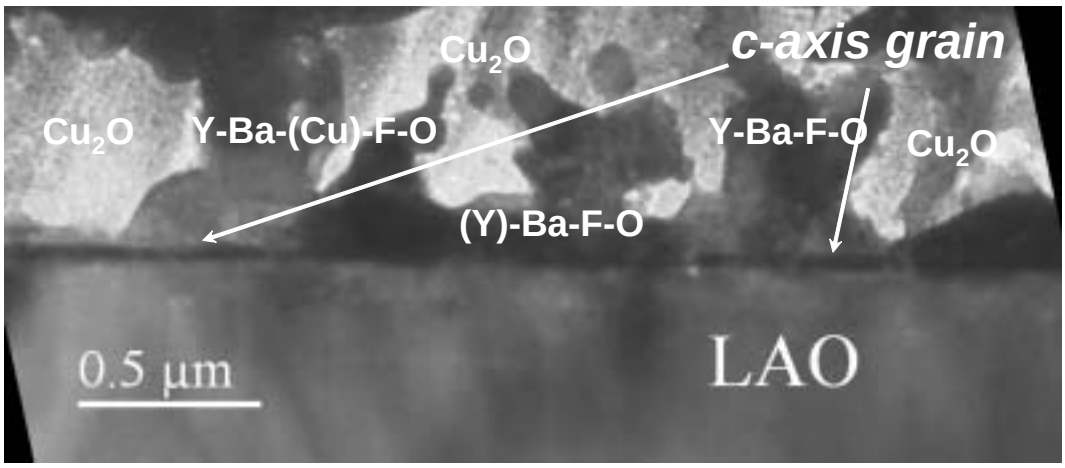


Figure 6.25. A low magnification TEM micrograph of sample *samba097* cooled from 700 $^{o}$C to room temperature with previous long time heat treatment, taken along the [*100*] direction of LAO. The white arrow points a *c*-axis oriented YBCO film grown at the interface.

On the contrary, a closer examination of the amorphous matrix of $Cu_2O$ by EELS suggests a collection of nanometric polycrystals randomly oriented, as shown in figure 6.26a. Moreover, another important observation is the fact that there is no $Cu_2O$ in contact with the LAO interface. This indicates a strong affinity of the nanocrystals of $Y_2O_3$, Ba-Y-F and $BaF_2$ for the LAO surface; this affinity seems to play an important role in the nucleation of YBCO which occurs at the interface but not in other regions in the precursor film. However, the $Cu_2O$ phase neither was observed in micro-Raman measurements (figure 6.24) nor XRD (figure 6.21), probably due to the nanometric amorphous character of this phase. In addition, the $Cu_2O$ phase has a single Raman active phonon mode at ~ 217 $cm^{-1}$[6.4] and XRD peak at $2\theta$ ~ 36.4 degree (table 6.4). Therefore, it is clear from high resolution TEM micrographs that the $Cu_2O$ phase does not tend to coarsen, which also indicates that is not a stable phase at the used temperature and pressure conditions. This is corroborated with the (P,T) phase diagram[5.10] which indicate that $Cu_2O$ is a metastable phase in our growth conditions whereas the CuO is the stable phase. Thus, the equilibrium phase CuO seems to grow at expenses of the $Cu_2O$.

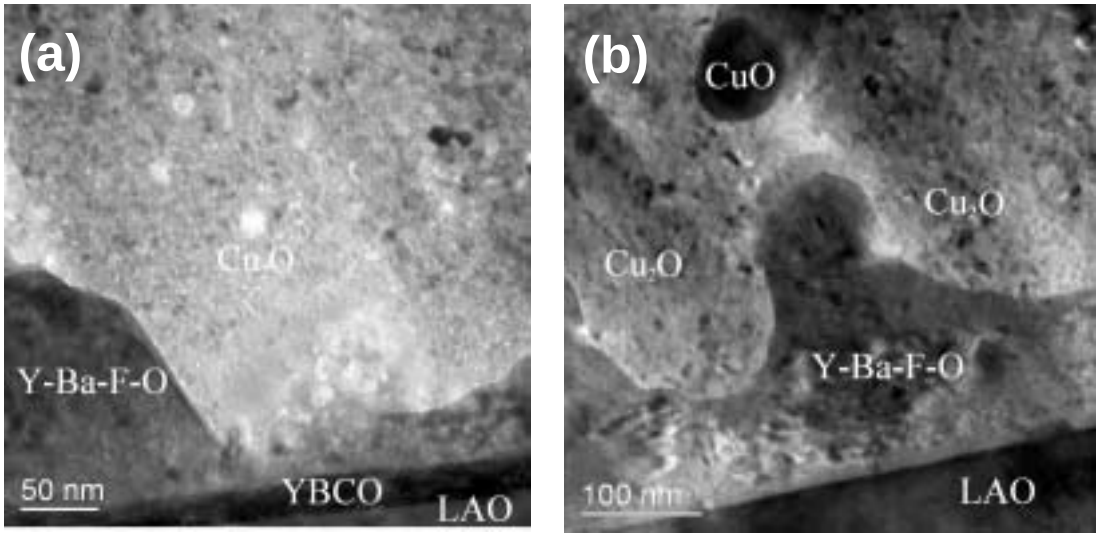


Figure 6.26. Cross sectional TEM micrographs of *samba097* sample along the [*100*] LAO direction. Notice the coexistence of $Cu_2O$, Ba-Y-F-O and $YBa_2Cu_3O_{6.5}$ epitaxial growth front onto interface in (a), while in (b) we observe the presence of nanocrystals of Ba-Y-F-O, CuO and $Cu_2O$ close to YBCO epitaxial growth front.

Based on the XRD, micro-Raman measurements and TEM micrographs obtained, we propose a sketch of the intermediate phase segregation in the films studied, as shown in figure 6.27. Intermediate phases of $BaF_2$, BaO, $Y_2Cu_2O_5$, CuO, $Cu_2O$. Ba-O-F and Y-Ba-O-F with defined boundaries exist. Moreover, the $YBa_2Cu_3O_{6.5}$ islands nucleate inhomogeneously at the interface with similar growth rates. On the other hand, on top of the YBCO growth front, the Y-Ba-O-F, $BaF_2$ and $Y_2O_3$ phases are found and separate the YBCO phase from the surrounding by CuO and $Cu_2O$ phases. We know that the formation of YBCO requires Y, Ba, Cu and O atoms, so the Cu atoms coming from the CuO nanocrystals or the $Cu_2O$ amorphous phase must have an extraordinary mobility to reach the YBCO growth front through the Y-Ba-O-F-like layer. We suspect that the Cu atom enter into the oxyfluorides structures through their vacancies to form YBCO.

In conclusion, we have observed a strong phase segregation of the intermediate phases and long length atomic diffusion at 700 $^oC$ for long heat treatments on the way to YBCO conversion. Moreover, there exists a strong tendency to epitaxial growth of precursor phases such as $BaF_2$ and $Y_2O_3$ at the interface showing an extraordinary mobility of the atomic species of the precursor phases. We have also observed the intermediate phases CuO, $Cu_2O$ and Y-Ba-O-F-like at long heat treatments. In addition, we have seen that there is a strong tendency to precursor phases coarsening except for

$Cu_2O$ phase. This is due to the fact that the equilibrium CuO phase is the stable phase and grows at expenses of the $Cu_2O$ phase. Finally, despite of the non YBCO growth conditions ($T_{growth}$ = 700 $^oC$, $P(H_2O)$ = 0.1 mbar and gas flow rate =0.0024 m/s) used to growth *samba097*, we have found that YBCO islands nucleated inhomogeneously at the substrate interface with similar growth rates, implying that the YBCO nucleation temperature is below 700 $^oC$. In the next section we will focus on three intermediate temperatures selected to define the YBCO nucleation temperature.

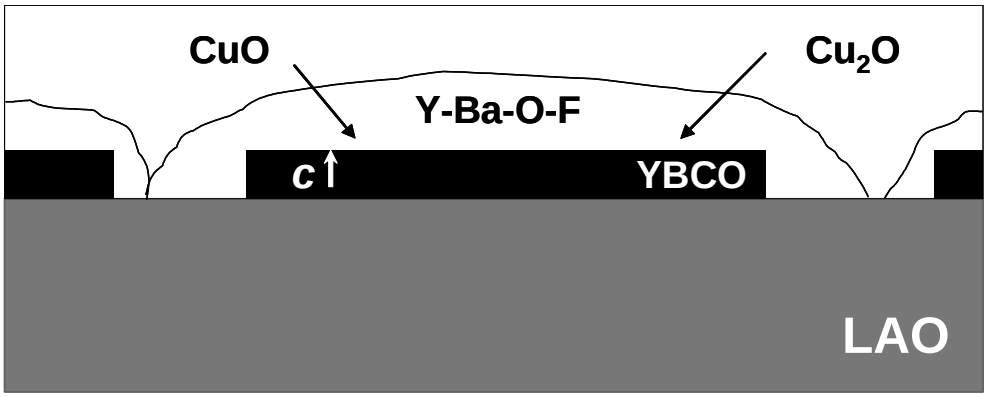


Figure 6.27. (a) Sketch of phase segregation in quenched sample that consist of phases with well defined boundaries. Around YBCO epitaxial growth a Y-Ba-O-F phase exist.

## 6.4. Temperature for YBCO formation

At the light of the results that we have obtained in the previous sections, we can affirm that strong phase segregation exists before the $YBa_2Cu_3O_{6.5}$ nucleation and that YBCO nucleation occurs solely at the substrate interface. This phase segregation was clearly observed in TEM micrographs, and it is directly related to temperature and duration of the heat treatment. Thus, the conversion of the intermediate phases into YBCO TFA film generates the following questions: What is the temperature for $YBa_2Cu_3O_{6.5}$ formation? And, is it true that above 700 $^oC$ the nucleation of YBCO occurs as claimed by McIntyre *et al*[6.13]?. In the next section we will give some evidence about this issue on the basis of the information obtained until now, and our preliminary results in three samples prepared towards clarifying this issue.

We have seen in the previous section that films quenched at 795 $^{o}$C present a majority of *c*-axis oriented YBCO grains normal to the substrate interface during the transformation of the intermediate phases under the conditions used to prepare YBCO films with optimal $T_c$ and $J_c$ ($T_{growth}$ = 795 $^{o}$C, P($H_2O$) = 7 mbar, P($O_2$) = 0.2 mbar and gas flow rate = 0.024 m/s). On another hand, quenched films at 700 $^{o}$C in non ideal YBCO grow conditions showed *c*- but also *a*-axis oriented YBCO grains normal to substrate interface during the transformation of the intermediate phases under long time heating temperature. Moreover, from measurements of the uniaxial texture by micro-Raman (see figure 5.17), we know that above 650 $^{o}$C, YBCO grains nucleated at the interface already exist with a large fraction of *a*-axis growth. Therefore, we performed thermal treatments of the precursor films at temperatures below 650 $^{o}$C to study the temperature of YBCO nucleation and to answer the above mentioned questions.

Three samples named *samba069*, *samba063* and *samba088* were prepared for this purpose. The growth parameters of these precursor samples are shown in tables 6.6, and 6.7, respectively. The main difference between *samba069* and *samba063* is the intermediate growth temperature, 575 and 525 $^{o}$C, respectively. These samples were annealed at an intermediate temperature and kept at this stage for 16 hours; afterwards an annealing at 795 $^{o}$C with the standard conditions was performed. Figure 6.29 displays the annealing profile used to growth the film *samba069* at 575 $^{o}$C for 16 hours. We arrived at 575 $^{o}$C in approximately ~ 22 minutes: The sample was quickly pulled out from the furnace to room temperature. A subsequent *ex-situ* annealing at 795 $^{o}$C was performed by using the annealing profile of figure 6.1.

**Table 6.6**

Conditions for YBCO film named *samba069* and *samba063*

| |
|---|
| Precursor solution prepared from YBCO powder |
| Concentration = 1.5 M |
| LAO Substrate |
| Optimized pyrolysis process |
| Heating ramp = 1500 $^{o}$C/h |
| P($H_2O$) = 7 mbar |
| P($O_2$) = 0.2 mbar |
| Gas flow rate = 0.024 m/s |
| Intermediate growth temperature = variable |
| Second growth temperature = 795 $^{o}$C |
| *ex-situ* process |

**Table 6.7**

Features of film *samba088*

| |
|---|
| Precursor solution prepared from YBCO powder |
| Concentration = 1.5 M |
| LAO Substrate |
| Optimized pyrolysis process |
| Heating ramp = 1500 $^{o}$C/h |
| P($H_2O$) = 7 mbar |
| P($O_2$) = 0.2 mbar |
| Gas flow rate = 0.024 m/s |
| Intermediate growth temperature = 475 $^{o}$C |
| Second growth temperature = 795 $^{o}$C |
| *in-situ* process |

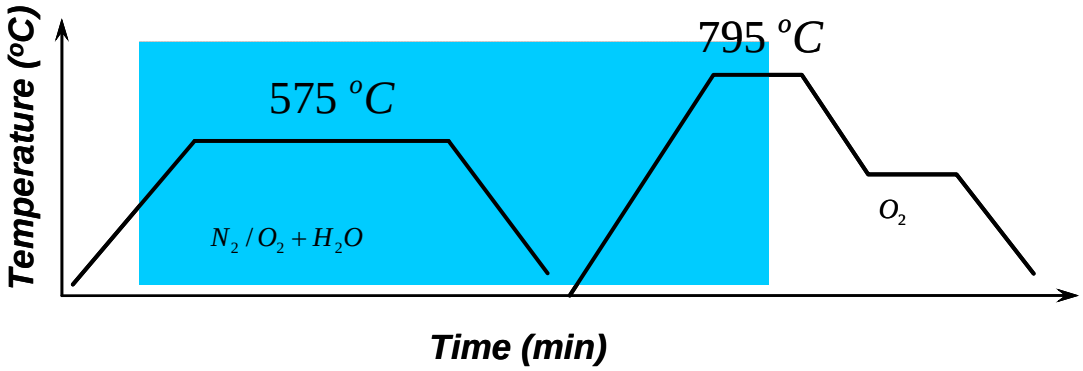


Figure 6.29. Annealing profile of *samba069* sample kept at 575 ºC for 16 hours and subsequently *ex-situ* annealed at 795 ºC. Humidified gas was introduced at 110 ºC. Main features of this sample are shown in table 6.6.

We performed standard XRD θ/2θ-scans (~ 1 hour scan) to sample named *samba069*, after the first growth temperature (575 ºC) as shown in figure 6.30. It displays the existence of the $BaF_2$ intermediate phase and $YBa_2Cu_3O_{6.5}$. We may observe the (*hkl*) and (*h00*) blurred $BaF_2$ profiles, and the (*00l*) $YBa_2Cu_3O_{6.5}$ profiles. In addition, an intense signature of the (*200*) reflection when compared to the (*00l*) $YBa_2Cu_3O_{6.5}$ profiles denotes the presence of a major concentration of *a*-axis oriented grains nucleated onto the interface, *i.e.*, *a*-axis oriented grains growth perpendicular to LAO surface, denoting a reduced quantity of *c*-axis oriented grains, as shown in figure 6.30. This YBCO growth is in agreement with the results of section 5.2.2.

Because the standard XRD θ/2θ-scan performed has low scattered signal and low statistical of intermediate phases, we performed a long accumulation time XRD θ/2θ-scan for 12 hours with a step Δ2θ ~ 0.02 degree. Now we may observe the coexistence of the intermediate phases $BaF_2$, $Ba_{1-x}Y_xF_2$, $Y_2Cu_2O_5$, $Y_2O_3$ and CuO, as shown in figure 6.31. The $Y_2Cu_2O_5$, $Y_2O_3$, $BaF_2$ and CuO phases just have random orientation. Moreover, the $BaF_2$ phase has the (*h00*) and random orientation. The curved background observed again, between 24º – 30º, is due to the presence of (*100*) LAO profile tail at ~ 23 degree.

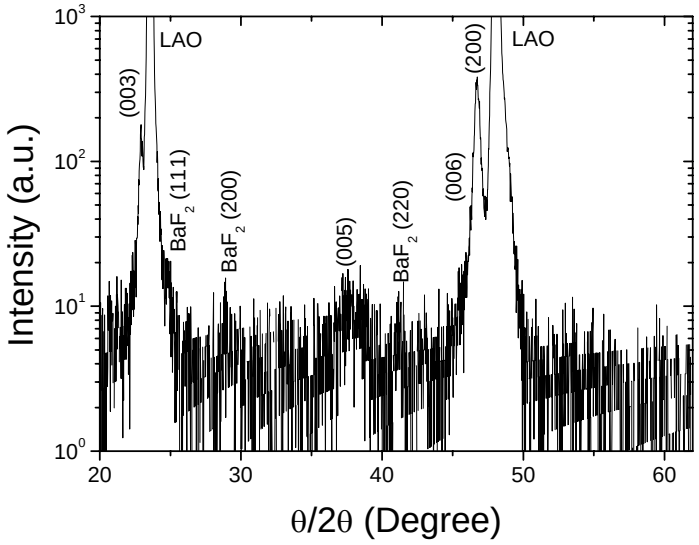


Figure 6.30. XRD pattern in logarithmic scale of a precursor film kept at 575 $^{o}$C for 16 hours (*samba069*). Notice the blurred signal of the $YBa_2Cu_3O_{6.5}$ *c*-axis oriented grains and of the $BaF_2$ intermediate phase, while a clear signature of $YBa_2Cu_3O_{6.5}$ *a*-axis oriented grains grown perpendicular to substrate surface, is seen.

After the subsequent annealing at 795 $^{o}$C in standard conditions ($P(H_2O)$ = 7 mbar, $P(O_2)$ = 0.2 mbar and gas flow rate = 0.024 m/s), we performed again standard XRD θ/2θ-scans as shown in figure 6.32. We observe that all intermediate phases reacted with each other to form epitaxial YBCO. On the other hand, we may also observe, in the magnification in the range between $44^{o} \leq 2\theta \leq 52^{o}$, an intense (*200*) than (00*l*) YBCO profile, as shown in figure 6.33. The major intensity of the (*h00*) profile compared to the (*00l*) YBCO profiles evidences the presence of a large fraction of *a*-axis oriented grains in the YBCO TFA film. This *a*-axis oriented growth is expected if at the intermediate temperature treatments of 575 $^{o}$C YBCO had already nucleated since low growth temperatures are favourable to *a*-axis oriented growth, as we saw in section 5.2.2. We have calculated the *c*-axis grain fraction using the (*005*) and (*200*) YBCO reflections by XRD, in similar way as done in section 3.1.1.2, the *c*-axis fraction, $f_c$ is equal to ~ 0.10±0.05.

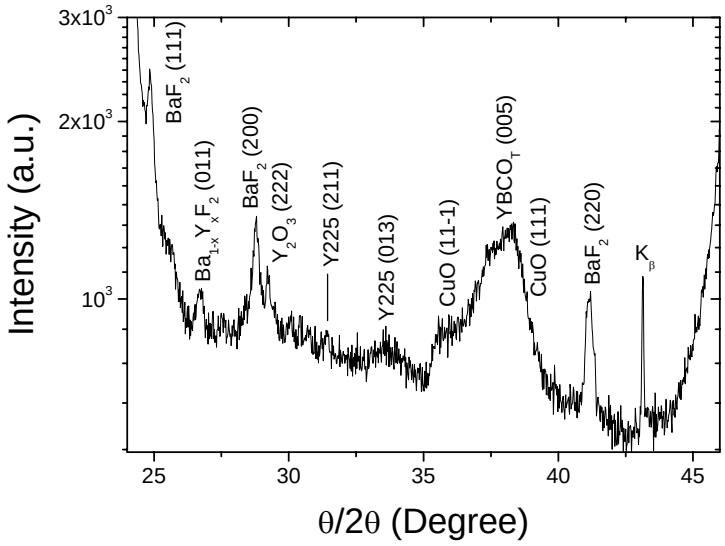


Figure 6.31. XRD pattern in logarithmic scale of precursor film stand by at 575 $^{o}$C for 16 hours (*samba069*). Notice the coexistence of $BaF_2$, $Ba_{1-x}Y_xF_2$, $Y_2O_3$, CuO, $Y_2Cu_2O_5$ and $YBa_2Cu_3O_{6.5}$ phases and the resolved peak at $2\theta \sim 29^{o}$ degree that consist of a mixing of (*200*) $BaF_2$ and (*222*) $Y_2O_3$ profiles. Curved background is due to (*100*) LAO tail.

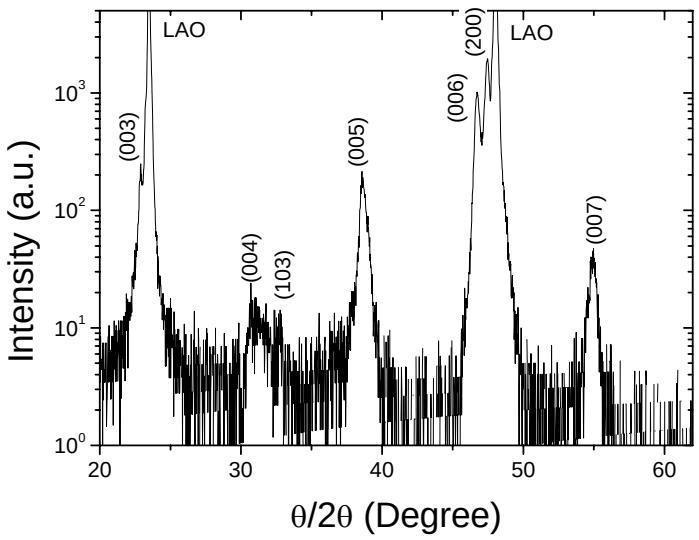


Figure 6.32. XRD pattern in logarithmic scale of the precursor film of figure 6.30 after annealing at 795 $^{o}$C. Notice the presence of *a*- and *c*-axis oriented grains perpendicular to the substrate surface.

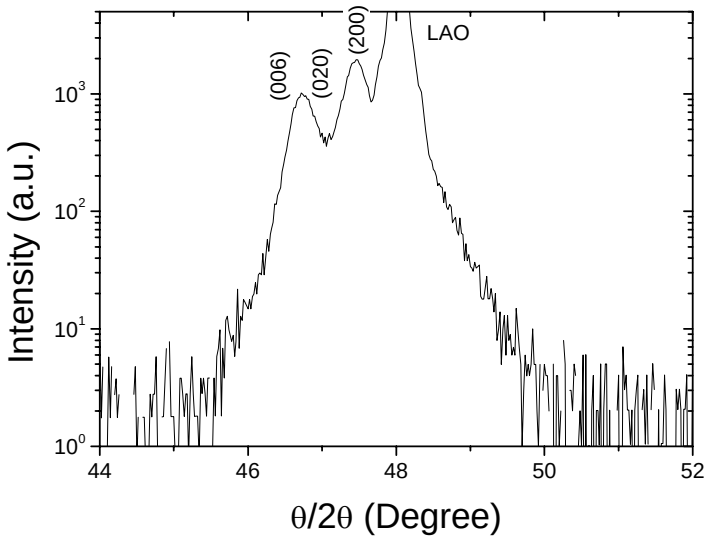


Figure 6.33. Magnification of the XRD pattern in logarithmic scale of figure 6.32 displaying the *a*-axis oriented grains feature of this film by the presence of the (*200*) YBCO profile.

We turn to micro-Raman measurements to obtain complementary information on the microstructure evolution of sample *samba069*. Figure 6.34 shows the Raman spectra of this sample measured after the two heat treatments. After the long intermediate treatment (575 $^{o}$C, 16 hours) the Raman spectrum only shows the presence of CuO phonon modes, as expected from section 6.1 (figure 6.4). Observations of the Raman spectrum after the annealing process at 795 $^{o}$C shows mainly an *a*-axis oriented YBCO film. An *a*-axis oriented film is characterized by a larger O(4)-$A_g$ Raman signal compared to the O(2,3)-$B_{1g}$ phonon mode signal. The uniaxial texture value was determined to be $\delta \sim 0.20 \pm 0.05$ in good agreement with the value determined by XRD data, and texture map and SEM micrographs shown in figure 6.35a and 6.35b, respectively, clearly showing the *a*-axis growth uniformity.

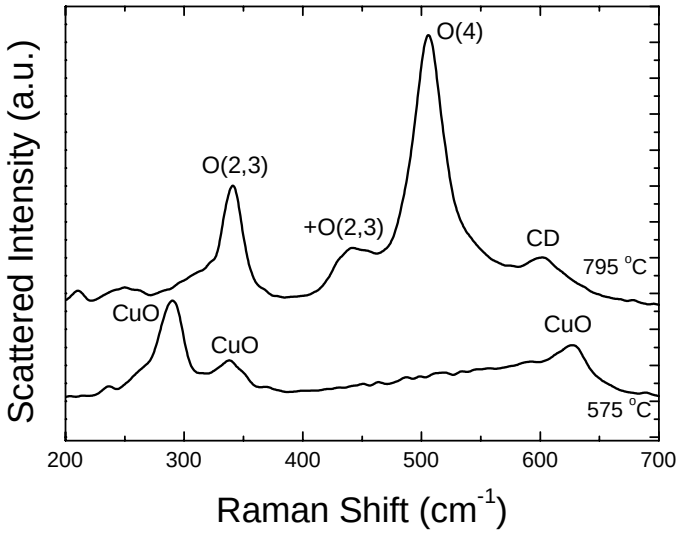


Figure 6.34. Raman spectra of a precursor film maintained at 575 °C for 16 hours and subsequently annealed at 795 °C (sample *samba069*). Notice the transformation of the precursor film to a highly *a*-axis oriented film due to presence of an intense Raman signal of the O(4)-$A_g$ compared to the O(2,3)-$B_{1g}$ phonon mode. The uniaxial texture value was $\delta \sim 0.20 \pm 0.05$.

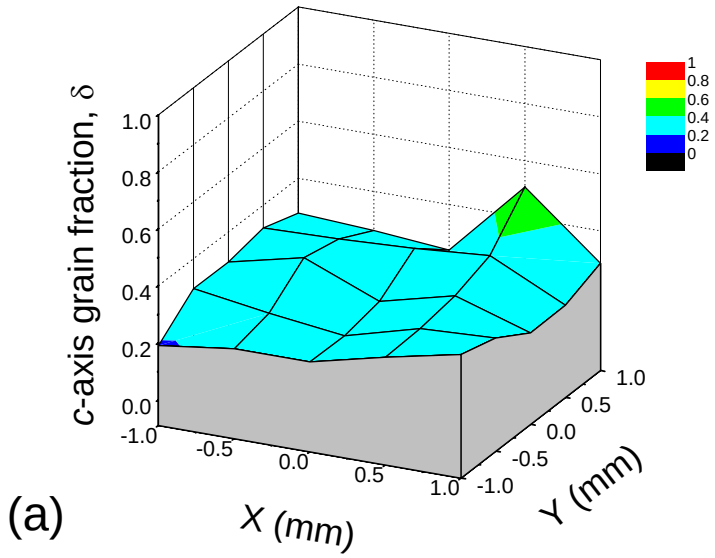


Figure 6.35 (a)

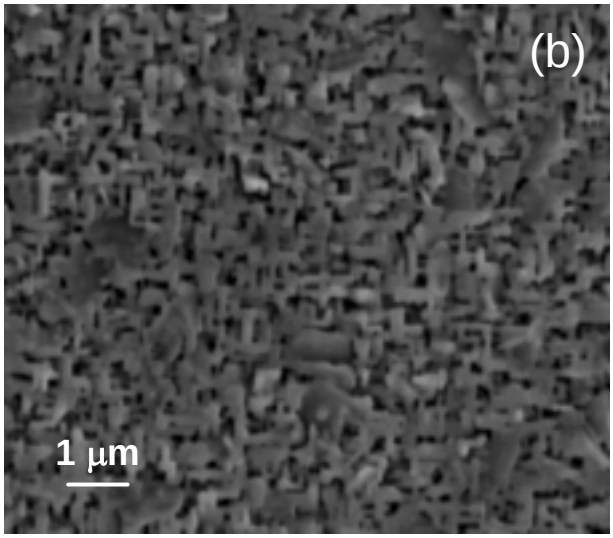


Figure 6.35. (a) Texture map and (b) SEM micrograph of *samba069* sample with a low *c*-axis oriented grain fraction, $\delta \sim 0.20 \pm 0.05$.

As it was mentioned above, the fact that an *a*-axis oriented film is observed after the high temperature treatment of 795 C evidence that at the intermediate growth temperature (575 $^{o}$C), *a*-axis nucleus had already formed. Therefore at this low growth temperature (575 $^{o}$C), it is possible to nucleate YBCO at the interface if we wait enough time.

We therefore lowered the intermediate temperature down to 525 $^{o}$C. The sample is named *samba063*. This sample was first annealed up to 525 $^{o}$C and kept in this stage for 16 hours. We arrive at 525 $^{o}$C in approximately ~ 20 minutes. The sample was quickly pulled out from the furnace to room temperature and subsequently *ex-situ* annealed at 795 $^{o}$C by using the annealing profile of figure 6.36. The main features of this sample are shown in table 6.6.

We performed a standard XRD θ/2θ-scan and the diffractogram only displays the presence of the blurred $BaF_2$ profiles, as shown in figure 6.37. We suspect that the other intermediate phases are probably highly nanocrystalline or amorphous, and therefore they are not displayed in the diffractogram. On the contrary, we have not found any signature of $YBa_2Cu_3O_{6.5}$ reflections. After a subsequent annealing at 795 $^{o}$C in standard conditions ($P(H_2O)$ = 7 mbar, $P(O_2)$ = 0.2 mbar and gas flow rate = 0.024 m/s), we performed again standard XRD measurements and the spectra is shown in figure

6.38. We observe that the diffractogram mainly consist of (*00l*) YBCO profiles. Thus, the film is mainly composed of *c*-axis oriented YBCO grains and the presence of the (*200*) YBCO profile is not appreciated in the magnified diffractogram shown in figure 6.39.

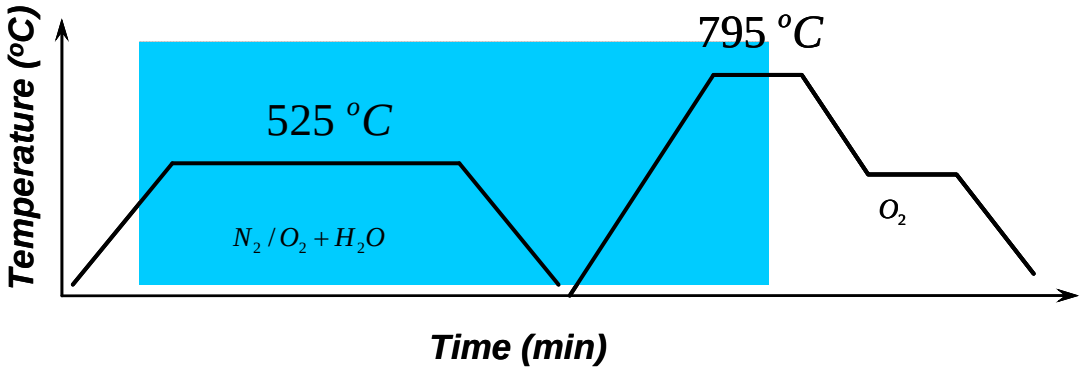


Figure 6.36. Annealing profile of a precursor sample maintained at 525 ºC for 16 hours and subsequent *ex-situ* annealed at 795 ºC (*samba063*). Humidified gas was introduced at 110 ºC. Main features of this sample are shown in table 6.6.

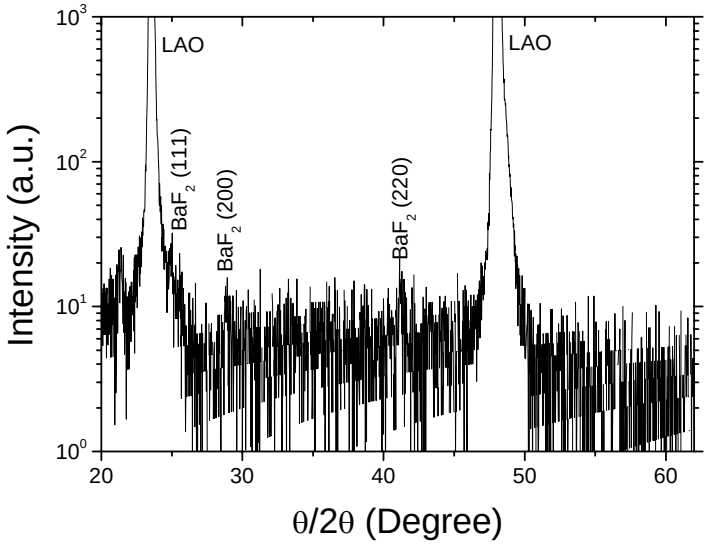


Figure 6.37. XRD pattern in logarithmic scale of a precursor film kept at 525 ºC for 16 hours (*samba063*). Notice the sole presence of $BaF_2$ phase, other intermediate phases or the $YBa_2Cu_3O_{6.5}$ phase were not detected.

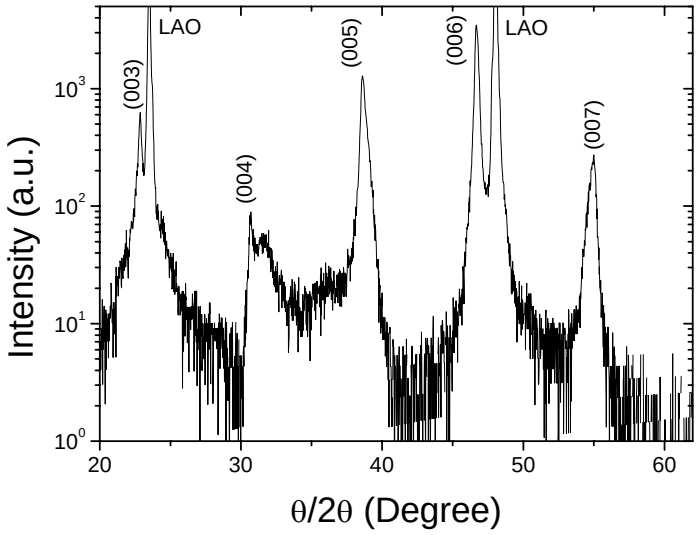


Figure 6.38. XRD pattern in logarithmic scale of the precursor film of figure 6.35 (*samba063*) after annealing at 795 $^{o}$C. Notice the existence of the (*00l*) $YBa_2Cu_3O_{6.5}$ profiless, the intermediate phases were not detected.

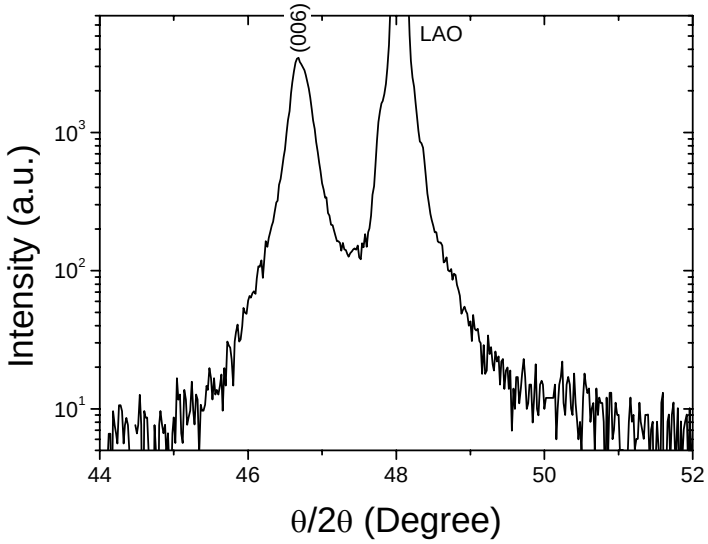


Figure 6.39. Magnification of the XRD pattern in logarithmic scale of figure 6.38 displaying the *c*-axis oriented grains feature of this film by the presence of the (*006*) YBCO profile. The (*200*) YBCO profile is not resolved in this figure.

We also performed micro-Raman measurements to obtain complementary information on the uniaxial texture of *samba063*. Figure 6.40 shows the Raman spectra of this sample measured after the two heat treatments. At 525 $^{o}$C the Raman spectrum clearly

shows the presence of CuO phonon modes meanwhile after annealing at 795 $^{o}$C a complete transformation of the intermediate phases into mainly *c*-axis oriented YBCO grains appears. We did not obtain any Raman signal of the intermediate phases within the detection limits, and a *c*-axis oriented film is clearly displayed due to large Raman signal of the O(2,3)-$B_{1g}$ mode when compared to the O(4)-$A_g$ phonon mode ($\delta \sim 0.90\pm0.05$).

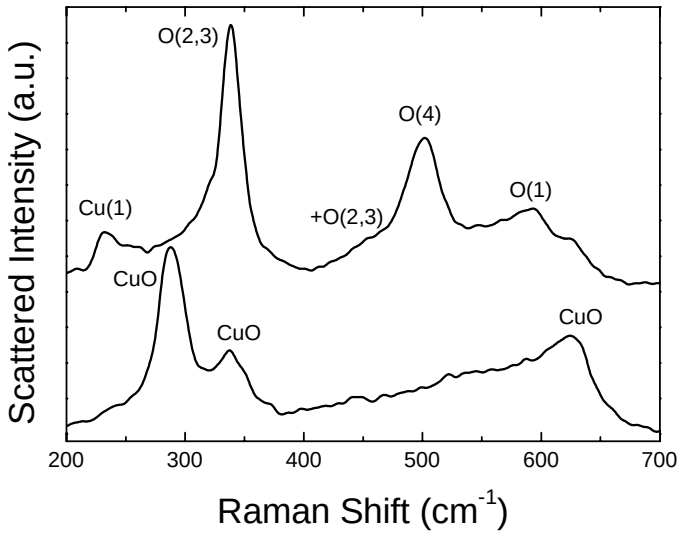


Figure 6.40. Raman spectra of a precursor film stand by at 525 $^{o}$C for 16 hours and subsequently *ex-situ* annealed at 795 $^{o}$C. Notice the transformation of the precursor film consisting mainly of CuO nanocrystals to a *c*-axis oriented film ($\delta \sim 0.90\pm0.05$).

At the light of these results we can state that at the intermediate growth temperature of 525 $^{o}$C, the YBCO nucleus are not formed at the interface, although we waited for long time (16 hours), their nucleation was not produced. Therefore, YBCO nucleation occurred in the second heat treatment at 795 $^{o}$C where the *c*-axis nucleation is already favourable.

Finally, the last even lower growth temperature selected to study the YBCO nucleation was 475 $^{o}$C. The sample is named *samba088*. This sample was first annealed up to 475 $^{o}$C, and kept at this stage for 5 hours, and subsequently *in-situ* annealed at 795 $^{o}$C. The annealing profile is shown in figure 6.41. We arrive at 475 $^{o}$C in approximately ~ 18 minutes. The main features of this sample are shown in table 6.7.

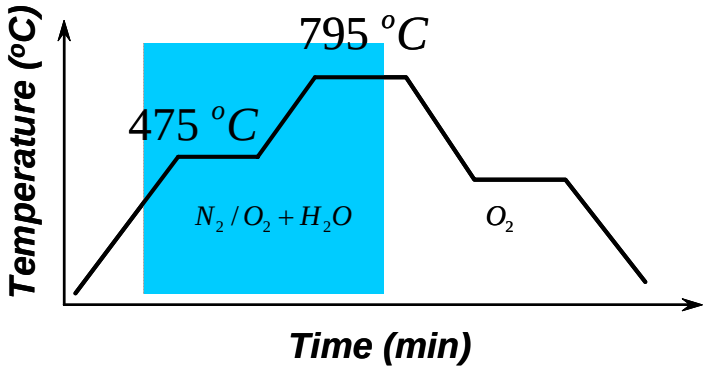


Figure 6.41. Annealing profile of a precursor sample maintained at 475 °C for 5 hours and subsequently *in-situ* annealed at 795 °C (*samba088*). Humidified gas was introduced at 110 °C. Main features of this sample are shown in table 6.7.

After subsequent *in-situ* annealing at 795 °C in standard conditions ($P(H_2O)$ = 7 mbar, $P(O_2)$ = 0.2 mbar and gas flow rate = 0.024 m/s), as the previous samples, we performed a standard XRD θ/2θ-scan. The corresponding diffractogram is shown in figure 6.42. We have observed intense (*00l*) YBCO profiles and also the (*400*) $Y_2O_3$ profile. We suspect that the $Y_2O_3$ phase is left as precipitates in the film. Moreover, a large fraction of *c*-axis oriented YBCO grains is obtained as evidenced by very intense (*00l*) YBCO profiles when compared to the (*200*) YBCO profile ($f_c$ ~ 0.90), as shown in figure 6.43.

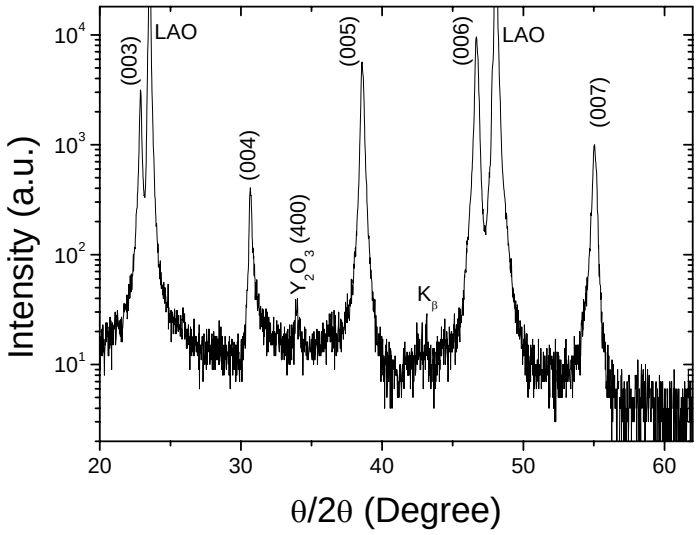


Figure 6.42. XRD pattern in logarithmic scale of YBCO film stand by at 475 °C for 5 hours and subsequently annealed at 795 °C. Notice the presence of YBCO *c*-axis oriented grains and the $Y_2O_3$ phase.

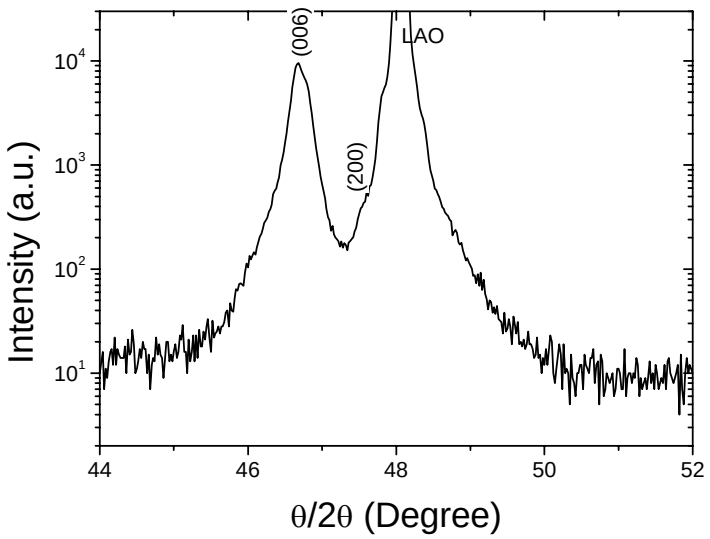


Figure 6.43. Magnification of the XRD pattern in logarithmic scale of figure 6.42 displaying a large *c*-axis oriented grain fraction of this film by the presence of an intense (*006*) YBCO profile ($f_c \sim 0.90$).

We also performed micro-Raman measurements to obtain complementary information on the microstructure evolution of *samba088*. Figure 6.44 shows the Raman spectra of *samba088*. We did not obtain any Raman signal of the intermediate phases such as the $Y_2O_3$ phase (at 377 $cm^{-1}$) probably due to the fact that our Raman probe scarcely reaches the interface as evidenced by the absence of LAO phonon mode in the spectra. A *c*-axis oriented YBCO film is clearly displayed due to presence of a larger Raman signal of O(2,3)-$B_{1g}$ mode when compared to the O(4)-$A_g$ phonon mode ($\delta \sim 0.92 \pm 0.05$).

In the same manner as in previous sample *samba063* discussion, we can conclude that at the intermediate temperature (475 $^oC$), YBCO nucleus can not be formed at the interface. Therefore, the YBCO nucleation temperature is found to be between 525 and 575 $^oC$. Further studies may refine this range. This is the first time that these low YBCO nucleation temperatures are experimentally evidenced and reported for the TFA process.

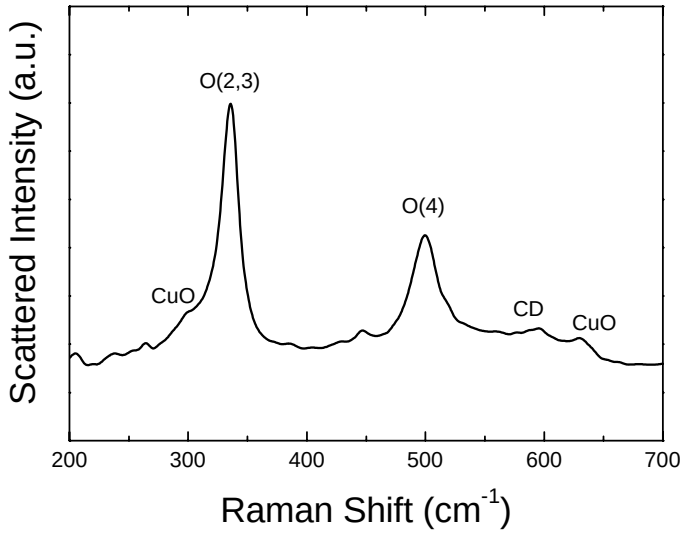


Figure 6.44. Micro-Raman spectra of a precursor film maintained at 475 $^{o}$C for 5 hours and subsequently *in-situ* annealed at 795 $^{o}$C (*samba088*). Notice that the film consists mainly of *c*-axis oriented grains due to presence of larger Raman signal of the O(2,3)-$B_{1g}$ mode ($\delta \sim 0.92 \pm 0.05$).

# Conclusions

Intermediate phases of YBCO MOD-TFA films on quenched samples at selected temperatures in the ramp of heat treatment were studied by XRD, micro-Raman and TEM techniques. The films consist of segregated phases such as: $BaF_2$, $Ba_{1-x}Y_xF_2$, $Y_2O_3$, CuO, BaO, $Cu_2O$, $Y_2Cu_2O_5$ and corresponding oxy-fluorides Ba-O-F, Y-Ba-O-F and Y-Ba-(Cu)-O-F. We have observed strong phase segregation and long length atomic diffusion at high temperatures. Moreover, we have seen a strong tendency of the precursor phases to coarse except for the $Cu_2O$ phase. The equilibrium phase CuO seems to grow at expenses of the $Cu_2O$ phase.

The chemical overall reaction of these intermediate phases to transform into YBCO is still an open issue. Moreover, several simultaneous kinetics reactions may likely occur involving the participation of the $BaF_2$, $Ba_{1-x}Y_xF_2$, $Y_2O_3$, CuO, BaO, $Cu_2O$, $Y_2Cu_2O_5$ and Y-Ba-(Cu)-O-F phases. On the other hand, TEM micrographs indicated that YBCO

islands nucleate inhomogeneously with similar growth rates at the substrate surface and not in other parts of the film.

We have observed that there exists a strong tendency to epitaxial growth of the precursor phases at the interface. The intermediate phases show an extraordinary mobility of the atomic species. In addition, based on TEM high resolution micrographs, EDP and EELS , the epitaxial formation of YBCO is strongly related to initial formation of Ba oxy-fluoride that aligns its (*111*) planes parallel with the (*100*) planes of LAO at the initial stage of the reaction. Finally, from the results of long time intermediate temperature heat treatments, and subsequent high temperature treatments at 795 $^{o}$C we may conclude that the YBCO nucleation is found to be between 575 and 525 $^{o}$C. This is the first time that this low YBCO nucleation temperatures are experimentally evidenced and reported for the TFA process.

# General Conclusions

1. The Micro-Raman spectroscopy study performed in this thesis, has allowed us to make progress in the knowledge of the growth mechanism of YBCO TFA films deposited onto single crystals substrates by chemical solutions. The high performance of the YBCO TFA-MOD films actually does not require the use of vacuum processes and hence our work gives further support to the view that chemical solution growth techniques have a great potential to become competitive. The knowledge acquired on the understanding of the relationship betwenn microstructural and superconducting properties of YBCO films will allow us now to optimize the growth conditions on metallic substrates for a continuous fabrication of high performance coated conductors.
2. Micro-Raman spectroscopy was used for non-destructive biaxial texture analysis of YBCO films and CC. We developed a new and simple methodology adapted to CC based on the specific Raman selection rules for YBCO and polarized Raman scattering experiments. Detailed information on the epitaxial quality of the superconducting films was obtained from two parameters: *c*-axis oriented grain fraction, $\delta$, and the degree of the *in-plane* orientation of the *c*-crystals, $Q_c$. We have demonstrated that micro-Raman spectroscopy is a very suitable technique to determine the surface uniformity and homogeneity of the uniaxial texture of films, to identify the appearance of *a*-crystals even in large *c*-crystal fraction samples and to estimate their size and distribution. We have theoretically modeled the Raman scattering intensities using different grain misorientation distribution functions and defining the $Q_c$ parameter accordingly. The analysis of several samples with different *in-plane* orientation has proved that the YBCO grains population in CC is governed by a Lorentz distribution. We have confirmed, therefore, that $Q_c$ is a true parameter to extract the degree of *in-plane* texture and grain misorientation distribution of YBCO CC. The feasibility and uniqueness possibility of micro-Raman to study the biaxial

texture sample uniformity has been demonstrated for CC and a simplification of the model developed has been presented in this case.

3. We have shown that the analytical capabilities of micro-Raman spectroscopy to analyse YBCO films are very broad. Raman scattering has developed into a very powerful tool in the field of high-$T_c$ superconductivity, providing information on the fundamental physical properties of superconducting materials. At a first glance the Raman spectra may provide a lot of information and features of the TFA films such as orientation, secondary phases, impurities, oxygen content and defects. The information obtained at the molecular scale basis by Raman scattering can sometimes help to deduce the mechanism of activity or reactivity of some process. We have used this technique to optimize of the YBCO TFA-MOD process by determining the factor inducing an aging of the solution or control by the pyrolysis process. Precipitates such as CuO and $BaCuO_2$, may be avoided by right storage of precursor solution in special sealed containers which avoid the contact of the solution with the air. We have also demonstrated the assistance of micro-Raman spectroscopy complemented with SEM to characterize the pyrolysis step. We have shown that in order to achieve high quality YBCO TFA-MOD films, during the pyrolysis process the film homogeneity must be preserved and any kind of phase segregation should be avoided, otherwise the final microstructure and superconducting properties are degraded.
4. High quality epitaxial YBCO films on LAO single crystal substrate have been obtained using TFA precursors. The influence of growth parameters on the final film quality (structure and superconducting properties) has been investigated. We have shown the influence of the growth temperature, water pressure and gas flow rate on the final properties has by investigating samples where the annealing time has been carefully adjusted to reaction completion (150 minutes) determined by monitoring the $BaF_2$ Raman signal.
5. SEM observations have shown that porosity is the main microstructural feature deeply modified by the growth temperature, being strongly enhanced in films grown at low temperatures. The influence of this parameter has been evidenced by the close correlation existing among uniaxial texture, normal state resistivity and the critical current densities in samples with different degrees of porosity.

The highest critical currents ($J_c$ = 3.2 MA/cm$^{-2}$ at 77 K and 27 MA/cm$^{-2}$ at 5 K) and the lowest normal state resistivity ( $\rho_{300K} \approx$ 200 μΩ-cm) were found in samples grown at 795 $^{o}$C. We note that under the present experimental conditions (P($H_2O$) = 7mbar, P($O_2$) = 0.2 mbar and gas flow = 0.024 m/sec) we obtained the best samples regarding microstrucure and physical properties.

6. Strong phase segregation and long length atomic diffusion is observed in YBCO MOD-TFA films quenched at selected temperatures in the growth temperature ramp by XRD, micro-Raman spectroscopy and TEM analysis have been performed. After the pyrolysis, the films consist of segregated nanocrystals of $BaF_2$, $Ba_{1-x}Y_xF_2$, $Y_2O_3$, CuO, BaO, $Cu_2O$ and $Y_2Cu_2O_5$ and a strong tendency to precursor phases coarsening has been observed except for the $Cu_2O$ phase. The equlibrium phase CuO seems to grow at expenses of the $Cu_2O$ phase. The chemical overall reaction of these intermediate phases to transform into YBCO is a still an open issue. Several simultaneous kinetics reactions may likely occur involving the $BaF_2$, $Ba_{1-x}Y_xF_2$, $Y_2O_3$, CuO, BaO, $Cu_2O$ and $Y_2Cu_2O_5$ phases. TEM results indicated that YBCO nucleates heterogeneously at the substrate surface and not in any other part of the film. There exists a strong tendency to epitaxial growth of the precursor phases at the interface. The epitaxial formation of YBCO is strongly related to initial formation of Ba oxy-fluoride that aligns its (*111*) planes parallel with the (*100*) planes of LAO at the initial stage of the reaction. The intermediate phases showing an extraordinary mobility of the atomic species. From the results of long time heat treatment, the YBCO nucleation is found to be between 575 and 525 $^{o}$C.
7. The usefulness and completeness of the micro-Raman spectroscopy in the study of the coated conductors and YBCO TFA-MOD films is proved. The uniqueness and easiness of micro-Raman spectroscopy to study and to characterize samples non destructively convert this technique in an invaluable and necessary tool in the field of material science.

# Bibliography

## *Chapter 1*

[1.1] A.C. Rose-Innes and E.H. Rhoderick. “Introduction to superconductivity”. Chapter 1, page 5. International Series in Solid State Physics. Pergamon Press Ltd. 1978.

[1.2] James F. Annet. “Superconductivity, Superfluids and Condensates”. Chapter 3, page 47. Oxford Master Series in Condensed Matter Physics. Oxford University Press. 2004.

[1.3] J. D. Jorgensen, M. A. Beno, D. G. Hinks, L. Soderholm, K. J. Volin, R. L. Hitterman, J. D. Grace, and Ivan K. Schuller. “Oxygen ordering and the orthorhombic-to-tetragonal phase transition in $YBa_2Cu_3O_{7-x}$”. Phys. Rev. B. **36** (1987) 3608 – 3615.

[1.4] R. J. Cava. “Oxide Superconductors”. J. Am. Ceram. Soc. **83** (2000) 5 – 28.

[1.5] P. Tixador “Les supraconducteurs”. Chapter 2, page 96. Ed. Hermès. 1995.

[1.6] D. Labalestier, A. Gurevich, D. Mathew F. And A. Polyanskii. “High-$T_c$ superconducting materials for electric power applications”. Nature **414** (2001) 368 – 377.

[1.7] T. Sasagawa, K. Kishio, Y. Togawa, J. Shimoyama and K. Kitazawa. “First-order vortex-lattice phase transition in $(La_{1-x}Sr_x)_2CuO_4$ single crystals: universal scaling of the transition lines in high-temperature superconductors”. Phys. Rev. Lett. **80** (1998) 4297 – 4300.

[1.8] U. Welp, J. A. Fendrich, W. K. Kwok, G. W. Crabtree, and B. W. Veal. “Thermodynamic evidence for a flux line lattice melting transition in $YBa_2Cu_3O_{7-\ delta}$”. Phys. Rev. Lett. **76** (1996) 4809 – 4812.

[1.9] H.C. Freyhardt; J. Hoffmann, J. Wiesmann, J. Dzick, K. Heinemann, A. Isaev, F. Garcia-Moreno, S. Sievers and A. Usoskin.. “YBaCuO thick films on planar and curved technical substrates”. IEEE Trans. Appl. Supercond. **7** (1997) 1426 – 1431.

[1.10] D. Dimos and P. Chaudhari and J. Mannhart. “Superconducting transport properties of grain boundaries in $YBa_2Cu_3O_7$ bicrystals”. Phys. Rev. B **41** (1990) 4038 – 4049.

[1.11] D. T. Verebelyi, D. K. Christen, R. Feenstra, C. Cantoni, A. Goyal, D. F. Lee, M. Paranthaman, P. N. Arendt, R. F. DePaula, J. R. Groves and C. Prouteau. “Low angle grain boundary transport in $YBa_2Cu_3O_{7-\delta}$ coated conductors”. Appl. Phys. Lett. **76** (2000) 1755 – 1757.

[1.12] L. T. Wille, A. Berera, and D. de Fontaine. “Thermodynamics of oxygen ordering in $YBa_2Cu_3O_z$”. Phys. Rev. Lett. **60** (1988) 1065 – 1068.

[1.13] J. D. Jorgensen, B. W. Veal, A. P. Paulikas, L. J. Nowicki, G. W. Crabtree, H. Claus, and W. K. Kwok. “Structural properties of oxygen-deficient $YBa_2Cu_3O_{7-\ delta}$”. Phys Rev B. **41** (1990) 1863 – 1877.

[1.14] M. N. Illiev, V. G. Hadjiev and V. G. Ivanov. “Raman spectroscopy of local structure and reordering process in $YBa_2Cu_3O_{7-x}$-type compounds”. J. Raman Spectros. **27** (1996) 333 – 342.

[1.15] K. Heine, J. Tenbrink, and M. Thöner. “High-field critical current densities in $Bi_2Sr_2Ca_1Cu_2O_{8+x}$/Ag wires”. Appl. Phys. Lett. **55** (1989) 2441 – 2443.

[1.16] Q. Li, G.N. Riley, R.D. Parrella, S. Fleshier, M.W. Rupich, W.L. Carter, J.O. Willis, J.Y. Coulter, J.F. Bingert, V.K. Sikka, J.A. Parrell and D.C. Larbalestier. “Progress in superconducting performance of rolled multifilamentary Bi-2223 HTS composite conductors”. IEEE Trans. Appl. Supercond. **7** (1997) 2026 – 2029.

[1.17] J. M. Phillips. “Substrate selection for high-temperature superconducting thin films”. J. Appl. Phys. **79** (1996) 1829 – 1848.

[1.18] S. Foltyn, P. Arendt, P. Dowden, R. DePaula, J. Groves, J. Coulter, Q. Jia, M. Maley and D. Peterson. “High-$T_c$ coated conductors-Performance of meter-long YBCO/IBAD flexible tapes”. IEEE Trans. Appl. Supercond. **9** (1999) 1519 – 1522.

[1.19] D. P. Norton, A. Goyal, J. D. Budai, D. K. Christen, D. M. Kroeger, E. D. Specht, Q. He, B. Saffian, M. Paranthaman, C. E. Klabunde, D. F. Lee, B. C. Sales and F. A. List. “Epitaxial $YBa_2Cu_3O_7$ on Biaxially Textured Nickel (001): An Approach to Superconducting Tapes with High Critical Current Density”. Science **274** (1996) 755 – 757.

[1.20] Y. Iijima and K. Matsumoto. “High-temperature-superconductor coated conductors: technical progress in Japan”. Supercond. Sci. Technol. **13** (2000) 68 – 81.

[1.21] J. L. MacManus-Driscoll. “Recent developments in conductor processing of high irreversibility field superconductor”. Annu. Rev. Sci. Matter. **28** (1998) 421 – 462.

[1.22] D. P. Norton. “Science and technology of high-temperature superconducting films”. Annu. Rev. Sci. Matter. **28** (1998) 299 – 343.

[1.23] J. M. Phillips. “High-temperature superconducting thin films”. Chapter 7 page 305, *in* High-Temperature Superconducting Materials Science and Engineering: New concepts and technology. Donglu Shi Editor. Ed. Pergamon Press. 1995.

[1.24] R. Wöndenweber. “Growth of high-$T_c$ films”. Supercond. Sci. Technol. **12** (1998) R86 – R102.

[1.25] T. Manabe, I. Yamaguchi, S. Nakamura, W. Kondo, T. Kumagai and S. Mizuta. “Crystallization and in-plane alignment behaviour of $YBa_2Cu_3O_{7-y}$ films on MgO(001) prepared by the dipping-pyrolysis process”. J. Mater. Res. **10** (1995) 1635 – 1643.

[1.26] T. Araki and I. Hirabayashi. “Review of a chemical approach to $YBa_2Cu_3O_{7-x}$-coated superconductors—metalorganic deposition using trifluoroacetates”. Supercond. Sci. Technol. **16** (2003) R71 – R94.

[1.27] K. Yamagiwa, T. Araki, Y. Takahashi, H. Hiei, S.B. Kim, K. Matsumoto, J. Shibata, T. Hirayama, H. Ikuta, U. Mizutani, I. Hirabayashi. “Epitaxial growth of $REBa_2Cu_3O_{7-y}$ films on various substrates by chemical solution deposition”. J. Cryst. Growth. **229** (2001) 353 – 357.

[1.28] J. A. Smith, M. J. Cima and N. Sonnenberg. “High critical current density thick MOD-derived YBCO films”. IEEE Trans. Appl. Supercond. **9** (1999) 1531 – 1534.

[1.29] O. Castaño, A. Cavallaro, A. Palau, J. C. González, M. Rossell, T. Puig, F. Sandiumenge, N. Mestres, S. Piñol, A. Pomar and X. Obradors. Supercond. Sci. Technol. **16** (2003) 45 – 53.

[1.30] A. Gupta, R. Jagannathan, E. I. Cooper, E. A. Giess, J. I. Landman, and B. W. Hussey. “Superconducting oxide films with high transition temperature prepared from metal trifluoroacetate precursors”. Appl. Phys. Lett. **52** (1988) 2077 – 2079.

[1.31] F. Parmigiani, G. Chiarello, N. Ripamonti, H. Goretzki and U. Roll. “Observation of carboxylic groups in the lattice of sintered $Ba_2YCu_3O_{7-y}$ high-$T_c$ superconductors”. Phys. Rev. **36** (1987) 7148 – 7150.

[1.32] A. Pinczuk and E. Burstein. “Fundamentals of Inelastic Light Scattering in Semiconductors and Insulators” Chapter 2, page. 23; *in* Light Scattering in Solids Vol. 1, Second Edition. M. Cardona Editor. Ed. Springer-Verlag. 1983.

[1.33] C. Kittel. “Introducción a la Física del Estado Sólido” Chapter 13, page 465. Segunda Edición. Ed. Reverté. 1975.

[1.34] W. Hayes and R. Loudon. “Scattering of Light by Crystals”. Chapter 1, page 1. Ed. John Wiley and Sons. 1978.

[1.35] C. Thomsen and M. Cardona. “Raman Scattering in High-$T_c$ Superconductors”. Chapter 8, page 409; *in* Physical Properties of High Temperature Superconductors Vol. 1. Donald M. Ginsberg Editor. Ed. World Scientific. 1989.

[1.36] M. Cardona. “Resonance Phenomena”. Chapter 2, page 19; *in* Light Scattering in Solids Vol. 2. M. Cardona and G. Güntherodt Editors. Ed. Springer-Verlag. 1982.

[1.37] Charles Poole, Jr. “Superconductivity”. Chapter 15 page 497. Ed. Academic Press. 1995.

[1.38] McCarthy, J. Z. Liu, R. N. Shelton and H. B. Radousky. “Raman-active phonons of a twin-free $YBa_2Cu_3O_7$ crystal: A complete polarization analysis”. Phys. Rev. B **41** (1990) 8792 – 8797.

[1.39]. E, Faulques and S. Lefrant. “Raman spectroscopy of superconducting materials”. Cond. Mater. News **5** (1996) 15 – 24.

## *Chapter 2*

[2.1] E. Heacht. “Optica” Chapter 13, Pag. 587.Ed. Addison Wesley Iberoamericana. 2000.

[2.2] P. Zhang, T. Haage, H.-U. Habermeier, T. Ruf and M. Cardona. “Raman spectra of ultra thin YBaCuO films”. J. Appl. Phys **80** (1996) 2935 – 2938.

[2.3] J. Humlícek, M. Garriga, M. Cardona, B. Gegenheimer and E. SchönherrP. Berberich and J. Tate. “Ellipsometric spectra of $YBa_2Cu_3O_7$ in the 1.7 – 5.3 eV range”. Solid State Comm. **66** (1988) 1071 – 1075.

[2.4] Jovin-Yvon-Spex. “SpectraMax Software”. v1.1. Part Number 31-087-080 Intruments S.A. Group. NP/Sm PSX/1297. Second Edition. December (1994).

[2.5] C. Hammond. “The Basics of Crystallography and Diffraction”. International Union of Crystallography Texts on Crystallography 5. Oxford University Press, Oxford, 2001.

[2.6] David B. Williams and C. Barry Carter. “Transmission Electron Microscopy: a texrbook for material science”. Chapter 10 page 155. Ed Plenium. 1996.

[2.7] L. J. Van der Pauw. “A method of measuring resistivity and may coefficient on lamellae of arbitrary shape”. Philips Tech. Rev. **20** (1958) 220 – 224.

[2.8] Alvaro Sanchez and Carles Navau. “Magnetic properties of finite superconducting cylinders. I. Uniform applied field”. Phys. Rev. **64** (2001) 214506.

## *Chapter 3*

[3.1] L.A. Farrow, T. Venkatesan, W.A. Bonner, X.D. Wu, A. Inam, and M.S. Hegde. “Raman scattering investigation of a single-crystal-like $YBa_2Cu_3O_{7-y}$ film”. J. Appl. Phys. **65** (1989) 4452 – 4453.

[3.2] E. García-González, G. Wagner, M. Reedyk, H.-U. Habermeier. “Raman scattering investigation of a single-crystal-like $YBa_2Cu_3O_{7-y}$ film” J. Appl. Phys., **78** (1995) 353 – 359.

[3.3] O. Martínez, J. Jiménez, D. Chambonnet, and C. Belouet. “Analysis of grain orientation and intergrain properties by micro-Raman spectroscopy in $YBa_2Cu_3O_{7-x}$ thin films”. J. Mat. Res., **15** (2000) 1069 – 1075.

[3.4] T. Puig, A. Puig-Molina, N. Mestres, H. Van Seijen, F. Alsina, J.C. González, X. Obradors, H. Graafsma, A. Usoskin, and H.C. Freyhardt. “Texture analysis of coated conductors by micro-Raman and Synchrotron x-ray diffraction”. Mater. Res. Soc. Symp. **659**, (2001) II5.6.1 – II5.6.6.

[3.5] C. Thomsen. “Light Scattering in High-$T_c$ Superconductors”. Chapter 6, page 285; *in* Light Scattering in Solids Vol. 6. M. Cardona and G. Güntherodt Editors. Ed. Springer-Verlag. 1991.

[3.6] R. Liu, C. Thomsen, W. Kress, M. Cardona, B. Gegenheimer, F. W. de Wette, J. Prade, A. D. Kulkarni and U. Schröder. “Frequencies, eigenvectors, and single-crystal selection rules of k=0 phonons in $YBa_2Cu_3O_{7-\ delta}$ : Theory and experiment”. Phys Rev. B **37** (1988) 7971 – 7974.

[3.7] N. Dieckmann, R. Kursten, M. Lohndorf, A. Bock. “Epitaxial quality of c-axis and a-axis oriented $YBa_2Cu_3O_7$ films: Characterization by Raman spectroscopy” Physica C **245** (1995) 212 – 218.

[3.8] U. Fano. “Effects of Configuration Interaction on Intensities and Phase Shifts” Phys Rev. **124** (1961) 1866 – 1878.

[3.9] A. Usoskin, F. García-Moreno, S. Siever, J. Dzick, H. C. Freyhardt, Appl. Supercond. 1999. Inst. Phys. Conf. Ser. **167** (2000) 447.

[3.10] R. Feenstra. unpublished.

[3.11] A. Palau, T. Puig, X. Obradors, A. Usoskin, H.C. Freyhardt, L Fernández, B. Holzapfel. "Inductive Analysis of Magnetic Granularity Effects in YBCO IBAD and RABiTS Coated Conductors". IEEE Trans on Supercond. **13** (2003) 2599 – 2602.

[3.12] C. Hammond. "The basics of crystallography and diffraction". International Union of Crystallography Texts on Crystallography 5. Oxford University Press. 2001.

[3.13] U. Weimer, R. Freile, P. Leiderer, U. Poppe, J. Schubert, J. Fröhlingsdorf, B. Stritzker, and W. Zander. "Investigation of the epitaxy of thin $YBa_2Cu_3O_{7-\delta}$ films" Physica C **168** (1990) 359 – 362.

[3.14] C. Thomsen, R. Wegerer, H.-U. Habermeier, and M. Cardona. "Determination of the degree of epitaxy in high-$T_c$ thin films by Raman spectroscopy". Solid State Commun. **83** (1992) 199 – 203.

## *Chapter 4*

[4.1] K. Yamagiwa , H. Hiei, Y. Takahashi, S.B. Kim, K. Matsumoto, H. Ikut, U. Mizutani and I. Hirabayashi. "Preparation of bi-axially aligned $YBa_2Cu_3O_{7-\delta}$ film on $CeO_2$-buffered MgO by chemical solution deposition". Physica C **334** (2000) 301 – 305.

[4.2] C. Rice, R. van Dover and G. Fisanick. "Preparation of superconducting thin films of $Ba_2YCu_3O_7$ by a novel spin-on pyrolysis technique". Appl. Phys. Lett. **51** (1987) 1842 – 1844.

[4.3] Y. Xu, A. Goyal, J. Lian, N. A. Rutter, D. Shi, S. Sathyamurthy, M. Paranthaman, L. Wang, P. M. Martin, and D. M. Kroeger. "Preparation of YBCO Films on $CeO_2$-Buffered (001) YSZ Substrates by a Non-Fluorine MOD Method". J. Am. Ceram. Soc. **87** (2004) 1669 – 1676.

[4.4] M. Rupich, Y. Liu, J. Ibechem and J. Hachey. "Synthesis of superconductors from soluble metal oxo alkoxides precursor". J. Mater. Res. **8** (1993) 1487 – 1496.

[4.5] T. Manabe, W. Kondo, S. Mizuta and T. Fumiga. "Crystallization of $YBa_2Cu_3O_{7-y}$ films on $SrTiO_3$ (100) by postannealing of precursors prepared by dipping-pyrolysis process". J. Mater. Res. **9** (1994) 858 – 864.

[4.6] T. Kumagai, T. Manabe, W. Kondo, S. Mizuta and K. Arai. "Preparation of high $J_c$ $Ba_2YCu_3O_{7-y}$-Ag composite films on $SrTi0_3$ (100) substrates by the dipping-pyrolysis process". Appl. Phys. Lett. **61** (1992) 988 – 990.

[4.7] P.-Y. Chu, I. Cmpion and R. Buchanan. "Processing effects on high-Tc properties of $YBa_2Cu_3O_{7-x}$ films from carboxylate solution precursors". J. Mater. Res. **8** (1993) 261 – 267.

[4.8] T. Bowmer and F. Shokoohi. "Synthesis of superconductors from metal neodacanoates". J. Mater. Res. **6** (1991) 670 – 676.

[4.9] P. McIntyre and m. Cima. "Heteroepitaxial growth of chemically derived ex situ $Ba_2YCu_3O_{7-x}$ thin films". J. Mater. Res. **9** (1991) 2219 – 2230.

[4.10] A. Gupta, R. Jannagathan, E. Copper, G. Giess, J. Landman and B. Hussey. "Superconducting oxide films with high transition temperature prepared from metal trifluoroacetate precursors". Appl. Phys. Lett. **52** (1988) 2077 – 2079.

[4.11] Oscar Castaño Linares. "Síntesis y caracterización de láminas delgadas superconductoras de altas corrientes críticas de $YBa_2Cu_3O_{7-\delta}$ obtenidas por MOD". PhD Thesis. ICMAB-CSIC. Barcelona. Abril 2004.

[4.12] P. McIntyre, M. Cima and M. Ng. "Metalorganic deposition of high-$J_c$ $Ba_2YCu_3O_{7-x}$ thin films from trifluoroacetate precursors onto (100) $SrtiO_3$". J. Appl. Phys. **68** (1990) 4183 – 4187.

[4.13] P. McIntyre, M. Cima, J. Smith, R. Hallock, M. Siegal and J. Phillips. "Effect of growth conditions on the properties and morphology of chemically derived epitaxial thin films of $Ba_2YCu_3O_{7-x}$ on (001) $LaAlO_3$". J. Appl. Phys. **71** (1992) 1868 – 1877.

[4.14] D. Verebelyi, U. Schoop, C. Thieme, X. Li, W. Zhang, T. Kodenkandath, A. Malozemoff, N. Nguyen, E. Siegal, D. Buczek, J. Lynch, J. Scudiere, M. Rupich, A. Goyal, E. Specht, P. Martin and M. Paranthaman. "Uniform performance of continuously processed MOD-YBCO-coated conductors using a textured Ni–W substrate". Supercond. Sci. Technol. **16** (2003) L19 – L22.

[4.15] T. Araki, T. Niwa, Y. Yamada, I. Hirabayashi, J. Shibata, Y. Ikuhara, K. Kato, T. Kato and T. Hirayama. "Growth model and the effect of CuO nanocrystallites on the properties of chemically derived epitaxial thin films of $YBa_2Cu_3O_{7-x}$". J. Appl. Phys. **92** (2002) 3318 – 3325.

[4.16] J. Dawley, P. Clem, T. Boyle, L. Ottley, D. Overmyer, M. Siegal. "Rapid processing method for solution deposited $YBa_2Cu_3O_{7-\delta}$ thin films". Physica C **402** (2004) 143 – 151.

[4.17] M. Rupich, D. Verebelyi, W. Zhang, T. Kodenkandath and X. Li. "Metalorganic deposition of YBCO films for second-generation high-temperature superconductor wires". Mat. Res. Soc. Bull. **29** (2004) 572 – 577.

[4.18] M. Yoshizumi. I. Seleznev amd M. J. Cima. "Reactions of oxyfluorides precursors for the preparation of barium yttrium cuprate films". Physica C **403** (2004) 191 – 199.

[4.19] T. Honjo, Y. Nakamura, R. Teranishi, Y. Tokunaga, H. Fuji, J. Shibata, S. Asada, T. Izumi, Y. Shiohara, Y. Iijima, T. Saitoh, A. Kaneko, K. Murata. "Fabrication and growth mechanism of YBCO coated conductors by TFA-MOD process". Physica C **392**–**396** (2003) 873 – 881.

[4.20] K. Char, M. S. Colclough, L. P. Lee, and G. Zaharchuk "Extension of the bi-epitaxial Josephson junction process to various substrates". Appl. Phys. Lett. **59** (1991) 2177 – 2179.

[4.21] M. Kakihana, M. Osada and V. Petrykin. "Raman spectroscopy as a unique tool for characterizing high-$T_c$ superconducting oxides". Physica C **338** (2000) 144 – 150.

[4.22] D. de Waal, K.-J. Range, M. Königstein and W. Kiefer. "Raman spectra of the barium oxide peroxide and strontium oxide peroxide series". J. Raman Spectr. **29** (1998) 109 – 113.

[4.23] P. Denham, G. R. Field, P.L. Morse and G. Wilkinson. "Optical and dielectric properties and lattice dynamics of some fluorite structure ionic crystals". Proc. Roy. Soc. Lond. A **317** (1970) 55 – 70.

[4.24] R. Bhadra, T. O. Brun, M. A. Beno, B. Dabrowski, D. G. Hinks, J. Z. Liu, J. D. Jorgensen, L. J. Nowicki, A. P. Paulikas, Ivan K. Schuller, C. U. Segre, L. Soderholm, B. Veal, H. H. Wang, J. M. Williams, K. Zhang, and M. Grimsditch. "Raman scattering from high-$T_c$ superconductors". Phys. Rev. B **37** (1988) 5142 – 5147.

[4.25] A. Mascarenhas, S. Geller, L. C. Xu, and H. Katayama-Yoshida, J. I. Pankove, and S. K. Deb. "Raman spectroscopic investigation of superconducting $YBa_2Cu_3O_{7-x}$, semiconducting $YBa_2Cu_3O_{6+x}$, and possible impurity phases". Appl. Phys. Lett. **52** (1988) 242 – 243.

[4.26] J. C. Irwin, J. Chrzanowski and T. WeiD. J. LockwoodA. Wold. “Raman scattering from single crystals of cupric oxide”. Physica C **166** (1990) 456 – 464.

[4.27] J. Chrzanowski and J. C. Irwin. “Raman scattering from cupric oxide”. Solid State Comm. **70** (1989) 11 – 14.

[4.28] A. Bhargava, J. A. Alarco, G. J. Millar, R. Bell, T. Yamashita and I. D. Mackinnon. “Fine-grained $Y_2Cu_2O_5$ powder from a co-precipitated precursor”. Mater. Lett. **26** (1996) 89 – 96.

[4.29] H. Chang, Y. T. Ren, Y. Y. Sun, Y. Q. Wang, Y. Y. Xue and C. W. Chu. “Raman studies on $BaCuO_2$, $Ba_2CuO_3$ and $Ba_2Cu_3O_{5.9}$”. Physica C **228** (1994) 383 – 388.

[4.30] D. Kirillov, J. P. Collman, J. T. McDevitt, G. T. Yee, M. J. Holcomb and I. Bozovic. “Raman spectra of $YBa_2Cu_3O_x$ superconductors with different oxygen content”. Phys. Rev. B **37** (1988) 3660 – 3663.

[4.31] M. V. Abrashev and M. N. Iliev. “Polarized Raman spectra of $Y_2BaCuO_5$: Normal-mode assignment from substitutions for Y and Ba”. Phys. Rev. B **45** (1992) 8046 – 8051.

[4.32] Z. V. Popovic, C. Thomsen, M. Cardona, R. Liu, G. Stanisi and W. König. “Optical phonons in $Y_2BaCuO_5$”. Solid State Comm. **66** (1988) 43 – 47.

[4.36] J. Ye and K. Nakamura. “Quantitative structure analyses of $YBa_2Cu_3O_{7\text{-delta}}$ thin films: Determination of oxygen content from x-ray-diffraction patterns”. Phys. Rev. B **48** (1993) 7554 – 7564.

[4.37] G. Gibson, J. L. Macmanus-Driscoll and L. Cohen. “Raman microscopy as a local probe of structural defects and oxygen content in HTS thin films”. IEEE Trans. Appl. Supercond. **7** (1997) 2130 – 2133.

[4.38] G. Gibson, R. Humphreys, L. Cohen and J. L. Macmanus-Driscoll. “Influence of growth temperature and composition on structural disorder in YBCO thin films”. IEEE Trans. Appl. Supercond. **9** (1999) 1848 – 1851.

[4.39] A. Ourzumad, J. Rentschler, J. Spence, M. O’Keeffe, R. Graham, D. Johnson Jr. and W. Rhodes. “Microstructure, oxygen ordering and planar defects in the high-Tc superconductor $YBa_2Cu_3O_{6.9}$”. Science **327** (1987) 308 – 310.

[4.40] E. T. Heyen, R. Liu, C. Thomsen, R. Kremer, M. Cardona, J. Karpinski, E. Kaldis, and S. Rusiecki. “Optical phonons in $YBa_2Cu_4O_8$ and $Y_2Ba_4Cu_7O_{15\text{- delta}}$”. Phys. Rev. B. **41** (1990) 11058 – 11067.

[4.41] G. A. Kourouklis, A. Jayaraman, B. Batlogg, R. J. Cava, M. Stavola, D. M. Krol, E. A. Rietman, and L. F. Schneemeyer. "Raman scattering in $MBa_2Cu_3O_7$ with M=Y, Eu, and Gd: Effect of $^{18}O$ substitution and oxygen vacancies on the Cu-O vibrational modes". Phys. Rev. B **36** (1987) 8320 – 8324.

## *Chapter 5*

[5.1] F. Lange. "Chemical Solution Routes to Single-Crystal Thin Films". Science **273** (1996) 903 – 909.

[5.2] S. Sathyamurthy and K. Salama. "Processing of Y123 coated conductors using metal organic decomposition". IEEE Trans. Appl. Supercond. **9** (1999) 1971 – 1974.

[5.3] T. Araki, Y. Takahashi, K. Yamagiwa, T. Yuasa, Y. Iijima, K. Takeda, S.B. Kim, Y. Yamada, and I. Hirabayashi. "Fabrication of $YBa_2Cu_30_{7-x}$ Films on Buffered Metal Tapes Fired at Low Temperature by MOD Method using Trifluoroacetate Salts". IEEE Trans. Appl. Supercond. **11** (2001) 2869 – 2872.

[5.4] A. Jee, B Ma, V A Maroni, M Li, B L Fisher and U Balachandran. "Texture development and superconducting properties of $YBa_2Cu_3O_x$ thin films prepared by a solution process in low oxygen partial pressure". Supercond. Sci. Technol. **14** (2001) 285 – 291.

[5.5] G. Gibson, L. F. Cohen, R. G. Humphreys and J. L. MacManus-Driscoll. "A Raman measurement of cation disorder in $YBa_2Cu_3O_{7-x}$ thin films". Physica C **333** (2001) 139 – 145.

[5.6] T. Iguchi, T. Araki, Y. Yamada, I. Hirabayashi and H. Ikuta. "Fabrication of Gd-Ba-Cu-O films by metal-organic deposition method using trifluoroacetates". Supercond. Sci. Technol. **15** (2002) 1415 – 1420.

[5.7] O. Castaño, A. Cavallaro, A. Palau, J. C. González, M. Rosell, T. Puig, S. Piñol, N. Mestres, F. Sandiumenge, A. Pomar, and X. Obradors. "Influence of Porosity on the Critical Currents of Trifluoroacetate-MOD $YBa_2Cu_3O_7$ Films". IEEE Trans. Appl. Supercond. **13** (2003) 2504 – 2507.

[5.8] A. Díaz, A. Pomar, G. Domarco, J. Maza, and Félix Vidal. "Critical current versus normal-state resistivity in granular $YBa_2CuO_{7-\delta}$". Appl. Phys. Lett. **63** (1993) 1684 – 1686.

[5.9] M. Mukaida and S. Miyazawa. "Preferential axis control of $YBa_2Cu_3O_x$, thin film by quasilattice-match engineering". J. Appl. Phys. **75** (1993) 1209 – 1212.

[5.10] R. Feenstra, T. B. Lindemer, J. D. Bundai and M. D. Galloway. "Effect of oxygen pressure on the synthesis of $YBa_2Cu_30_{7-x}$ thin films by post-deposition annealing". J. Appl. Phys. **69** (1991) 6569 – 6585.

[5.11] V. G. Hadjiev, C. Thomsen, A. Erb, G. Müller-Vogt, M. R. Koblischka and M. Cardona. "Effect of oxygen disorder on superconductivity-induced self-energy effects in impurity-free $YBa_2Cu_3O_{7-\delta}$". Solid State Comm. **80** (1991) 643 – 647.

[5.12] J. Yoo, K.J. Leonard, D.F. Lee, H.S. Hsu, L. Heatherly, F.A. List, N.A. Rutter, A. Goyal, M. Paranthaman, and D.M. Kroeger. "Effects of conversion parameters on the transport properties of YBCO films in the $BaF_2$ ex situ process". J. Mater. Res. **19** (2004) 1281 – 1289.

[5.13] S. Sathyamurthy and K. Salama. "Processing of $YBa_2Cu_3O_x$ films by solution techniques using metal organic decomposition". J. Supercond. **11** (1998) 545 – 553.

[5.14] M. Suenaga. "BaF2 processes for $YBa_2Cu_3O_7$ conductors: promises and challenges". Physica C **378-391** (2002) 1045 – 10.

[5.15] A. C. Westerheim, Alfredo C. Anderson, D. E. Oates, S. N. Basu, D. Bhatt and M. J. Cima. "Relation between electrical properties and microstructure of $YBa_2Cu_3O_{7-x}$ thin films deposited by single-target off-axis sputtering". J. Appl. Phys. **75** (1994) 393 – 403.

## *Chapter 6*

[6.1] K Venkataraman, D F Lee, K Leonard, LHeatherly, S Cook, MParanthaman, M Mika and V A Maroni. "Reel-to-reel x-ray diffraction and Raman microscopy analysis of differentially heat-treated Y–$BaF_2$–Cu precursor films on metre-length RABiTS". Supercond. Sci. Technol. **17** (2004) 739 – 749.

[6.2] L. Wu, V. Solovyov, H. Wiesmann, Y. Zhu and M. Suenaga. "Mechanisms for hetero-epitaxial nucleation of $YBa_2Cu_3O_{6.1}$ at a buried precursor/$SrTiO_3$ interface in the postdeposition reaction process". Appl. Phys. Lett. **80** (2002) 419 – 421.

[6.3] Jaume Gazquez. Master degree Thesis. UAB-ICMAB-CSIC (2005).

[6.4] R. Liu, C. Thomsen, M. Cardona and H. Mattausch. "Presence of $Cu_2O$ in $MBa_2Cu_3O_6$ (M= Sm, Ho), semiconducting modification of high temperature superconductors". Solid State Comm. **65** (1988) 67 – 70.

[6.5] B. Pivac, K. Furic, D. Desnica, A. Borghesi and A. Sassella. “Raman line profile in polycrystalline silicon”. J. Appl. Phys. **86** (1999) 4383 – 4386.

[6.6] J. F. Xu, W. Ji, Z. X. Shen, W. S. Li, S. H. Tang, X. R. Ye, D. Z. Jia, X. Q. Xin. “Raman spectra of CuO nanocrystals”. J. Raman Spectrosc. **30** (1999) 413 – 415.

[6.7] M. Norton and C. Carter. “Observations on the growth of $YBa_2Cu_3O_{7-\delta}$ thin films by transmission electron microscopy” *in* Interfaces in High-$T_c$ Superconducting Systems. Chapter 1 pag.1. S. Shindé and D. Rudman editors. Springer Verlag. 1994.

[6.8] V. Solovyov, H. Wiesmann, L. Wu, Y. Zhu and M. Suenaga. “Kinetics of $YBa_2Cu_3O_7$ film growth by postdeposition processing”. Appl. Phys. Lett. **76** (2000) 1911 – 1913.

[6.9] V. F. Solovyov, H. Wiesmann, L. Wu, M. Suenaga, K. Venkatareman and V. Maroni. “A new technique for the growth of epitaxial YBCO using spray pyrolysis”. Physica C **415** (2004) 125 – 132.

[6.10] J. Shibata, T. Honjo, H. Fuji, T. Araki, I. Hirabayashi, T. Hirayama, T. Izumi, Y. Shiohara, T. Yamamoto and Y. Ikuhara. “Crystallization mechanism of $Nd_{1+x}Ba_{2-x}Cu_3O_{7-y}$ and $YBa_2Cu_3O_{7-y}$ films deposited by metalorganic deposition method using trifluoroacetates”. J. Mater. Res. **17** (2002) 1266 – 1275.

[6.11] J. I. Langford and J. C. Wilson. “Scherrer after sixty years: a survey and some new results in the determination of crystallite size”. J. Appl. Cryst. **11** (1978) 102 – 113.

[6.12] . B. Qadri, E. F. Skelton, D. Hsu, A. D. Dinsmore, J. Yang, H. F. Gray, and B. R. Ratna. “Size-induced transition-temperature reduction in nanoparticles of ZnS”. Phys. Rev. **60** (1999) 9191 – 9193.

[6.13] P. C. McIntyre, C. M. Cima and A. Roshko. “Epitaxial nucleation and growth of chemically derived $YBa_2Cu_3O_7$ thin films on (001) $SrTiO_3$”. J. Appl. Phys. **77** (1995) 5263 – 5272.

[6.14] L. Wu, Y. Zhu, V.F. Solovyov, H.J. Wiesmann, A.R. Moodenbaugh, R.L. Sabatini, and M. Suenaga. “Nucleation and growth of $YBa_2Cu_3O_x$ on $SrTiO_3$ and $CeO_2$ by a $BaF_2$ postdeposition reaction process”. J. Mater Res. **16** (2001) 2870 – 2884.